Alma Mater Studiorum · University of Bologna

School of Science
Department of Physics and Astronomy
Master Degree in Physics

Competition between boson condensation and molecule formation in 2D Bose-Fermi mixtures with a pairing interaction

Supervisor:
Prof. Pierbiagio Pieri

Submitted by:
Fabrizio Pavan

Academic Year 2020/2021

Abstract

The study of ultra-cold atomic gases is one of the most active field in contemporary physics. The main motivation for the interest in this field consists in the possibility to use ultracold gases to simulate in a controlled way quantum many-body systems of relevance to other fields of physics, or to create novel quantum systems with unusual physical properties. An example of the latter are Bose-Fermi mixtures with a tunable pairing interaction between bosons and fermions. In this work, we study with many-body diagrammatic methods the properties of this kind of mixture in two spatial dimensions, extending previous work for three dimensional Bose-Fermi mixtures. At zero temperature, we focus specifically on the competition between boson condensation and the pairing of bosons and fermions into molecules. By a numerical solution of the main equations resulting by our many-body diagrammatic formalism, we calculate and present results for several thermodynamic quantities of interest. Differences and similarities between the two-dimensional and three-dimensional cases are pointed out. Finally, our new results are applied to discuss a recent proposal for creating a p-wave superfluid in Bose-Fermi mixtures with the fermionic molecules which form for sufficiently strong Bose-Fermi attraction.

Contents

Introduction

When a gas of particles is cooled to extremely low temperatures, quantum effects become dominant and the different behaviours between fermionic and bosonic particles become evident.

A gas of identical bosons (particles with integer spin) undergoes Bose-Einstein condensation, a phase transition to a state of matter which was predicted in 1925 but experimentally observed only in 1995. A Bose-Einstein condensate (BEC) also exhibits superfluidity, the property of a fluid to flow without any friction. On the contrary, identical non-interacting fermions (particles with half-integer spin) have to occupy different quantum mechanical single-particle states, not allowing for a Bose-Einstein condensate. However, in the presence of an attractive interaction, fermions can also pair up into composite bosons and undergo in this way a condensation. This is the phenomenon at the heart of superconductivity. All these physical phenomena find an excellent testing platform in ultracold gases. In fact, thanks to the recent development of experimental techniques, such as laser cooling, it has been possible to cool down to near absolute zero atomic and molecular gases and explore in this way the quantum regime where these interesting phenomena occur. In addition, ultracold gases allow one to test theories and to address fundamental issues of quantum mechanics as well as to reproduce physical systems relevant to other areas in physics, with a exibility and a degree of tunability of parameters unimaginable in the original system of interest. Furthermore ultracold gases offer the possibility to construct novel many-body systems, which are not commonly found in nature . For these reasons, ultracold gases provide a fundamental platform for the quantum

simulation of complex many-body Hamiltonians with more flexibility than normally available in conventional condensed matter systems (see for example [1] and [2]).

Recently, Bose-Fermi mixtures have drawn increasing attention. The case of of Bose-Fermi mixtures with a tunable attraction between bosons and fermions is particularly interesting. In the so-called strong-coupling regime, pair correlations become so intense that bosons and fermions will pair and form composite fermions. The formation of bound molecules enters in competition with the tendency of bosons to condense. For sufficiently intense attractions and for a mixture with a number of bosons that does not exceed the number of fermions, condensation can be completely suppressed (even at zero temperature), since all bosons will participate to the molecular phase. The final result is a Fermi-Fermi mixture, composed of molecules and the unpaired fermions.

This evolution has been studied in 3D, in the works [3], [4] (at finite temperature) and [5] (at zero temperature). In all these papers, 3D Bose-Fermi mixtures were studied with a many-body T-matrix diagrammatic approach, based on the inclusion of the so-called *ladder diagrams*. This selection of diagrams is able to describe correctly both the weak-coupling limit and the opposite limit of strong BF-attraction, with the formation of composite fermions. In particular the depletion of the condensate fraction evaluated in [5] with the T-matrix formalism fully agrees with the results obtained in a very recent experimental work [6]. This represents a strong support for the use of the many-body T-matrix approach. At the same time, progress with experimental techniques has made possible experiments with ultracold gas in dimensions lower than 3D. The 1D and 2D regimes open the possibility to explore a different kind of physics, with different behaviours with respect to 3D. One of the main features is that the tendency of matter to order at temperatures near $T = 0$ is hampered in lower dimensions. This is due to the presence of more intense fluctuations with respect to the 3D systems. Also for this reason, in the last decade, there has been an increasing attention on experiments involving 2D ultracold gases (as for example 2D ultracold systems of ^{6}Li atoms). In addition, 2D systems, may represent

an interesting platform to simulate non-trivial topological phases of matter and to understand the origin of high-T_c superconductivity, which represent one of the main unsolved problems in condensed matter physics ([7], [8] and [9]).

Two-dimensional Bose-Fermi mixtures are still marginally explored, even from a theoretical point of view. Recently a paper by Bazak and Petrov [10] has considered the scattering properties of 2D BF mixtures. In particular their work considers a mixture with a BF attraction and a BB repulsion. The main result of [10] is quite promising: with realistic values of Bose-Bose repulsion, it is possible to create a mixture of a BF molecules without any more complicated bound states (for example trimer states BFF, BBF; tetramer states and so on). The BF molecules are identical fermions, for which the s-wave interaction is suppressed by the Pauli principle. In addition, a strong p-wave attraction between the BF molecules can be obtained in this regime. One can thus think to use this system as a controllable setup to quantum simulate the $p_x + ip_y$ superfluid, and explore its peculiar properties. In particular, $p_x + ip_y$ superfluids are interesting for the quantum simulation of Majorana fermions.

For these reasons, it appears both timely and important to study attractive Bose-Fermi mixtures in 2D with the same T-matrix approach that has been validated by recent experiments in 3D. The extension of such an approach to the 2D regime, and the numerical solutions of the resulting equations that determine the main thermodynamic quantities of the 2D BF mixture constitute the main object of the present thesis. We mention, in this respect, that some preliminary results in two-dimensions were obtained, within the same formalism, also in [11]. The results obtained in the present work agree with those of [11] when comparison is possible, and, at the same time provide a much more complete analysis with respect to that presented in [11].

The thesis is organized as follows. In Chapter 1, we introduce the quantum theory of scattering, which is relevant to describe interactions in ultracold gases. Firstly, we analyze the 3D case, which is commonly treated also in textbooks. Then, we will discuss the scattering theory in two di-

mensions, which is instead marginally addressed in textbooks. In particular we compare the 2D and 3D regimes, underlying the differences. We then analyze the so-called *quasi-2D* regime, that represents the experimental way to explore 2D physics with ultracold gases. Finally we will give an example of the use of ultracold gases as effective quantum simulators of 2D systems.

Chapter 2 is entirely devoted to a general description of Bose-Fermi mixtures with a pairing interaction between bosons and fermions. We summarize previous theoretical works in 3D, underlining the main results of [3], [4] and [5]. Then we give a brief description of the recent experiment of Ref. [6]. The Chapter is concluded by reporting the main results of the work [10] for a Bose-Fermi mixture in 2D.

Chapter 3 presents the T-matrix formalism and the fundamental equations to describe the properties of a 2D Bose-Fermi mixture at zero temperature. The resulting equations need to be solved numerically: Chapter 4 then describes the general structure of the algorithm and of the numerical program which we have written to this end. In particular, we explain how to deal with divergent integrals (which need a convergent factor) in the numerical program, and the main tricks used to accelerate their convergence.

Chapter 5 finally presents the main results of our work. We first analyze the weak-coupling regime, and compare the solutions of our numerical simulations with the perturbative calculations provided by [12] and [13]. We then show the results for the chemical potentials, the condensate fraction and the momentum distributions, in the full BF-coupling range. By combining our calculations of the condensate fraction with the estimate of the p-wave interaction between BF molecules of Ref. [10], we present predictions for the p-wave superfluid gap, and determine the optimal coupling regime to achieve experimentally a p-wave superfluid in 2D Bose-Fermi mixtures.

Chapter 1

Ultracold gases and scattering theory

In this Chapter, we will introduce the quantum theory of scattering, which is relevant to describe interactions in ultracold gases. The 3D case is commonly treated also in textbooks, while the scattering theory in two dimensions is only marginally addressed in textbooks. We will discuss both the 2D and 3D regimes, underlying the differences. We will then analyze the so-called quasi-2D regime, which represents the experimental way to explore 2D physics with ultracold gases. The Chapter is concluded with some examples of use of ultracold gases as effective quantum simulators of 2D systems.

1.1 General considerations on ultracold gases

An important feature of cold atomic vapours is that particle separations, which are typically of order 10^2 nm, are usually an order of magnitude larger than the length scales associated with the atom–atom interaction. Consequently, two-body scattering processes dominate, in general, over processes involving simultaneously more than two particles. Moreover, since the atoms have low velocities, many properties of these systems may be calculated in terms of a single parameter, the scattering length. In a scattering process, the internal states of the particles in the initial or final states

are described by a set of quantum numbers, such as those for the spin, the atomic species, and their state of excitation. We shall refer to a possible choice of these quantum numbers as a channel. Because of the existence of several hyperfine states for a single atom, the scattering of cold alkali atoms is a multi-channel problem. Besides inelastic processes that lead to losses of atoms from the trapping potential, coupling between channels also gives rise to Feshbach resonances, in which a low-energy bound state in one channel strongly modifies scattering in another channel. Feshbach resonances make it possible to tune both the magnitude and the sign of the effective atom–atom interaction, and they have become a powerful tool for investigating cold atoms. For all but the very lightest atoms, it is impossible from theory alone to make reliable calculations of the scattering properties of cold atoms because the atom–atom interaction potentials cannot be calculated with sufficient accuracy. In addition, many properties relevant for cold-atom studies are not directly accessible to experiment. Consequently, in deriving information about two-body scattering it is usually necessary to extract information about the interaction from one class of measurements, and then to use theory to predict properties of interest. Following the development of laser cooling, understanding of low-energy atomic collisions has increased enormously. In particular the use of photoassociation spectroscopy and the study of Feshbach resonances have made it possible to deduce detailed information on scattering lengths.

In the next Section we will introduce the basic notions of 3D scattering theory, following [14].

1.2 Scattering wave function and scattering amplitude in 3D

From basic Quantum Mechanics we know that the wave-function for two particles can be expressed as product between a part that describes the motion of the center of mass like a free particle of mass $M = m_1 + m_2$ and a part that describes the relative motion with reduced mass $m_r =$

$m_1 m_2/(m_1+m_2)$:

$$\left[-\frac{\hbar^2\nabla^2}{2m_r}+V(\mathbf{r})\right]\psi(\mathbf{r})=\left[\hat{H}_0+V(\mathbf{r})\right]\psi(\mathbf{r})=E\psi(\mathbf{r}) \tag{1.1}$$

Let us assume a short-range potential, so there exist a characteristic length r^* above which the potential can be neglected ($V(\mathbf{r})\approx 0$ for every $|\mathbf{r}|>r^*$). So for $r>r^*$ the equation (1.1) becomes the free Schroedinger equation, whose general solution is given by a superposition of plane waves. Our intent is to write down a solution given by the sum between a plane wave with momentum $\mathbf{p}$ and a scattering state with momentum $\mathbf{p}'$. Since we are interested in elastic processes, we can fix $E=\epsilon_{\mathbf{p}}=\hbar^2p^2/2m_r$. From the above considerations, we have that the time-independent Schroedinger equation in a basis-independent notation becomes:

$$\left[\epsilon_{\mathbf{p}}-\hat{H}_0\right]|\psi_{\mathbf{p}}\rangle=\hat{V}\,|\psi_{\mathbf{p}}\rangle \tag{1.2}$$

The solution of the homogeneous equation ($\hat{V}=0$) is given simply by $|\mathbf{p}\rangle$, which can be added to any solution of equation (1.2). The particular solution of equation (1.2), which incorporates the appropriate boundary conditions relevant for the scattering problem is thus given by:

$$|\psi_{\mathbf{p}}^{(+)}\rangle=|\mathbf{p}\rangle+\frac{1}{\epsilon_{\mathbf{p}}-\hat{H}_0+i\epsilon}\hat{V}\,|\psi_{\mathbf{p}}^{(+)}\rangle \tag{1.3}$$

where $\epsilon\to 0^+$ to deal with the singularity in the denominator. The reason for choosing $i\epsilon$ and not $-i\epsilon$ will become clear shortly below. This equation is know in the literature as the *Lippmann-Schwinger equation*. In order to find the scattering wavefunction $\psi_{\mathbf{p}}^{(+)}$, we multiply both sides of equation (1.3) with $|\mathbf{r}\rangle$. In this way we obtain:

$$\langle\mathbf{r}|\psi_{\mathbf{p}}^{(+)}\rangle=\langle\mathbf{r}|\mathbf{p}\rangle+\int d\mathbf{r}'\,\langle\mathbf{r}|\,\frac{1}{\epsilon_{\mathbf{p}}-\hat{H}_0+i\epsilon}\,|\mathbf{r}'\rangle\,\langle\mathbf{r}'|\,\hat{V}\,|\psi_{\mathbf{p}}^{(+)}\rangle \tag{1.4}$$

where the first term term on the right-hand side corresponds to the incoming plane wave:

$$\langle\mathbf{r}|\mathbf{p}\rangle=\frac{e^{i\mathbf{p}\cdot\mathbf{r}}/\hbar}{(2\pi\hbar)^{3/2}} \tag{1.5}$$

while the calculation of the second term is more laborious, and gives:

$$\begin{aligned}\int d\mathbf{r}' \langle \mathbf{r}| \frac{1}{\epsilon_{\mathbf{p}} - \hat{H}_0 + i\epsilon} |\mathbf{r}'\rangle \langle \mathbf{r}'| \hat{V} |\psi_{\mathbf{p}}^{(+)}\rangle = \\ = \int d\mathbf{r}' \int \frac{d\mathbf{p}}{(2\pi\hbar)^3} \frac{e^{i\mathbf{p}'\cdot(\mathbf{r}-\mathbf{r}')/\hbar}}{\epsilon_{\mathbf{p}} - \epsilon_{\mathbf{p}'} + i\epsilon} \langle \mathbf{r}'| \hat{V} |\psi_{\mathbf{p}}^{(+)}\rangle = \\ = -\frac{m_r}{\hbar} \int d\mathbf{r}' \frac{e^{ip|\mathbf{r}-\mathbf{r}'|/\hbar}}{2\pi|\mathbf{r}-\mathbf{r}'|} \langle \mathbf{r}'| \hat{V} |\psi_{\mathbf{p}}^{(+)}\rangle\end{aligned} \tag{1.6}$$

Since we assumed *a priori* that the potential $V(\mathbf{r})$ is short ranged, we are interested on the behaviour of the scattering wavefunction at distances that are large with respect to this range. Therefore we can write the interatomic distance for $r \gg r'$ as:

$$|\mathbf{r}-\mathbf{r}'| = \sqrt{r^2 - 2\mathbf{r}\cdot\mathbf{r}' + r'^2} = r\sqrt{1 - 2\frac{\mathbf{r}\cdot\mathbf{r}'}{r^2} + \frac{r'^2}{r^2}} \approx r - \frac{\mathbf{r}}{r}\cdot\mathbf{r}' \tag{1.7}$$

so thanks to the condition (1.7), we get a much simpler equation than (1.6):

$$\begin{aligned}\int d\mathbf{r}' \langle \mathbf{r}| \frac{1}{\epsilon_{\mathbf{p}} - \hat{H}_0 + i\epsilon} |\mathbf{r}'\rangle \langle \mathbf{r}'| \hat{V} |\psi_{\mathbf{p}}^{(+)}\rangle \approx \\ -\frac{m_r}{\hbar^2} \frac{e^{ipr/\hbar}}{2\pi r} \int d\mathbf{r}' e^{-ip\frac{\mathbf{r}}{r}\cdot\mathbf{r}'/\hbar} \langle \mathbf{r}'| \hat{V} |\psi_{\mathbf{p}}^{(+)}\rangle\end{aligned} \tag{1.8}$$

then, we define the vector $\mathbf{p}' = p\mathbf{r}/r$, which has the same length as the vector $\mathbf{p}$, but points in the direction $\mathbf{r}/r$. In this context we can define a fundamental quantity called *scattering amplitude*:

$$f(\mathbf{p}', \mathbf{p}) = -\frac{1}{2\pi}(2\pi\hbar)^3 \frac{m_r}{\hbar^2} \langle \mathbf{p}'| \hat{V} |\psi_{\mathbf{p}}^{(+)}\rangle \tag{1.9}$$

We have obtained the important result that, at distances much larger than the range of the interaction, the total wavefunction can be written as the sum of an incoming plane wave and an outgoing spherical wave:

$$\psi_{\mathbf{p}}^{(+)}(\mathbf{r}) = \frac{1}{(2\pi\hbar)^{3/2}} \left[e^{i\mathbf{p}\cdot\mathbf{r}/\hbar} + f(\mathbf{p}', \mathbf{p}) \frac{e^{ipr/\hbar}}{r} \right] \tag{1.10}$$

Now we understand the presence of $i\epsilon$ factor in the (1.3). As said above, the second term of the wavefunction $\psi_{\mathbf{p}}^{(+)}$ in (1.10) is an outgoing spherical wave. A small negative imaginary factor $-i\epsilon$ would have led to an incoming spherical wave. i.e. a description of the time-reversed scattering process.

1.3 Two body transition-matrix

In the previous section we have recovered the Lippmann-Schwinger equation, where it was used to determine the general form of the scattering wavefunction, which was seen to consist of an incoming plane wave and an outgoing spherical wave at large separations between the colliding particles. Now, instead to treat the problem with the scattering states $|\psi_{\mathbf{p}}^{(+)}\rangle$, we analyze the problem in a more convenient way. We define an operator $\hat{T}^{2B}$ called *Two body transition-matrix*, defined by the following relation:

$$\hat{V}\,|\psi_{\mathbf{p}}^{(+)}\rangle = \hat{T}^{2B}\,|\mathbf{p}\rangle \tag{1.11}$$

The matrix elements of the two body T-matrix are directly related to the scattering amplitudes $f(\mathbf{p}', \mathbf{p})$ of equation (1.9). Indeed we get:

$$f(\mathbf{p}', \mathbf{p}) = -\frac{m_r(2\pi\hbar)^3}{2\pi\hbar^2}\,\langle \mathbf{p}'|\,\hat{V}\,|\psi_{\mathbf{p}}^{(+)}\rangle = -\frac{m_r(2\pi\hbar)^3}{2\pi\hbar^2}\,\langle \mathbf{p}'|\,\hat{T}^{2B}\,|\mathbf{p}\rangle \tag{1.12}$$

It is convenient to rescale momenta with the relation $\mathbf{k} = \mathbf{p}/\hbar$ and to use the normalization condition $\langle \mathbf{r}|\mathbf{k}\rangle = e^{i\mathbf{k}\cdot\mathbf{r}}$:

$$f(\mathbf{k}', \mathbf{k}) = -\frac{m_r}{2\pi\hbar^2}\,\langle \mathbf{k}'|\,\hat{T}^{2B}\,|\mathbf{k}\rangle = -\frac{m_r}{2\pi\hbar^2} t(\mathbf{k}', \mathbf{k}) \tag{1.13}$$

Consequently, the Lippmann-Schwinger equation (1.3) assumes the form:

$$\hat{T}^{2B}\,|\mathbf{k}\rangle = \hat{V}\,|\mathbf{k}\rangle + \hat{V}\frac{1}{E - \hat{H}_0 + i\epsilon}\hat{T}^{2B}\,|\mathbf{k}\rangle \tag{1.14}$$

which has to be satisfied for any state $|\mathbf{k}\rangle$. This leads us to another equivalent way to define the T-matrix. It can been written as the solution of the *off-shell Lippmann-Schwinger* equation for any (complex) energy z:

$$\hat{T}^{2B}(z) = \hat{V} + \hat{V}\frac{1}{z - \hat{H}_0 + i\epsilon}\hat{T}^{2B}(z) \tag{1.15}$$

By writing $\hat{H} = \hat{H}_0 + \hat{V}$, with some manipulations, one obtains the alternative equation for the two-body T-matrix:

$$\hat{T}^{2B}(z) = \hat{V} + \hat{V}\frac{1}{z - \hat{H} + i\epsilon}\hat{V} \tag{1.16}$$

The equation (1.16) can be expanded in power of $\hat{V}$:

$$\hat{T}^{2B}(z) = \hat{V} \sum_{n=0}^{\infty} \left[\frac{1}{z - \hat{H}_0 + i\epsilon} \hat{V} \right]^n \tag{1.17}$$

which is known as the Born series of the T-matrix. The operator $(z - \hat{H}_0)^{-1}$ has the physical meaning of the non-interacting propagator of the colliding atoms at a (complex) energy z. A common approximation for the T-matrix is to take only the terms $n = 0$ and $n = 1$ into in account (Born approximation). From equation (1.17) we see that the T matrix physically describes the outcome of a collision process, in which the particles interact quantum mechanically an arbitrary number of times. In this way the T-matrix is given by the resulting sum over all elementary interaction processes that take place during a collision. Now let us consider again equation (1.16). Let it be $\{|\psi_\alpha\rangle\}$ a complete set of eigenstates for $\hat{H} = \hat{H}_0 + \hat{V}$. Inserting this set, we find:

$$\hat{T}^{2B}(z) = \hat{V} + \sum_{\alpha} \hat{V} \frac{|\psi_\alpha\rangle \langle\psi_\alpha|}{z - \epsilon_\alpha} \hat{V} \tag{1.18}$$

where the summation over α is discrete for possible bound sates of the interaction potential with energies $\epsilon_\alpha < 0$, while the summation becomes an integration for the continuum of scattering stets with energy $\epsilon_\alpha > 0$. Explicitly, we have:

$$\hat{T}^{2B}(z) = \hat{V} + \sum_{\nu} \hat{V} \frac{|\psi_\nu\rangle \langle\psi_\nu|}{z - \epsilon_\nu} \hat{V} + \int \frac{d\mathbf{k}}{(2\pi)^3} \hat{V} \frac{|\psi_{\mathbf{k}}^{(+)}\rangle \langle\psi_{\mathbf{k}}^{(+)}|}{z - \epsilon_{\mathbf{k}}} \hat{V} \tag{1.19}$$

which shows that the two-body T-matrix has poles in the complex plane that corresponding to the bound state of the interaction potential, while it has also a branch cut on the positive real axis due to the continuum of the scattering states.

1.4 Partial-wave expansion

In Section 1.2, by treating the two-body problem, we have shown the general expression for the scattering wave function at large-distances (equation

(1.10)).

$$\psi_{\mathbf{k}}^{(+)}(\mathbf{r}) = e^{i\mathbf{k}\cdot\mathbf{r}} + f(\mathbf{k}', \mathbf{k})\frac{e^{ikr}}{r} \tag{1.20}$$

To further evaluate the scattering wave function in (1.10), we consider the usual case of a spherical potential $V(\mathbf{r}) = V(r)$, which depends only on the distance between atoms. As a consequence, the elastic scattering amplitude is determined by the magnitude k of the incoming momentum $\mathbf{k}$ and a single angle θ with the outgoing momentum $\mathbf{k}'$, i.e $f(\mathbf{k}', \mathbf{k}) = f(k, \theta)$.

Thus we can expand its scattering amplitude $f(k, \theta)$ with the method of partial waves:

$$f(k, \theta) = \sum_{l=0}^{\infty}(2l + 1)f_l(k)P_l(cos\theta) \tag{1.21}$$

where $P_l(x)$ are the Legendre polynomials. To see the meaning of the partial-wave amplitudes $f_l(k)$, we can take advantage of the following identity:

$$e^{i\mathbf{k}\cdot\mathbf{r}} = \sum_{l}(2l + 1)i^l j_l(kr)P_l(cos\theta) \tag{1.22}$$

where , for $r \to \infty$, we can use the asymptotic behaviour of the spherical Bessel wave function $j_l(kr)$:

$$e^{i\mathbf{k}\cdot\mathbf{r}} \approx \sum_{l}(2l + 1)P_l(cos\theta)\left(\frac{e^{ikr} - e^{-i(kr-l\pi)}}{2ikr}\right). \tag{1.23}$$

In other words, we have written the plane-wave part $e^{i\mathbf{kr}}$ of the scattering wave-function (1.20) as sum (or better speaking as a superposition) of incoming and outgoing spherical waves. So by comparing equations (1.20),(1.21), and (1.23), we have just shown that the presence of an interaction potential changes the coefficient of the outgoing spherical waves according to:

$$\frac{e^{ikr}}{r} \to (1 + 2ikf_l(k))\frac{e^{ikr}}{r}. \tag{1.24}$$

Moreover, due to the conservation of probability flux, the square-modulus of the term $(1 + 2ikf_l(k))$ has to be equal to one. This implies that:

$$1 + 2ikf_l(k) = e^{2i\delta_l(k)}, \tag{1.25}$$

defining in this way the phase shift $\delta_l(k)$. So, summarizing, at large distances, the change in the wave-function, due to the scattering process, is simply reflected by a shift in the phase of every outgoing partial wave. The key point is that ultracold gases can be cooled to the point where only one partial wave is dominant and all the others can be neglected. This is because, one can show that $f_l(k) \sim k^{2l}$ for small k. Typical momenta of the atoms scale with the thermal de Broglie wavelength λ_T, if they are bosons, or the least between λ_T and the Fermi momentum k_F, if they are fermions. Momenta will thus be very small for dilute ultracold gases, and only the partial wave with zero angular momentum ($l = 0$) will contribute.

It is useful now to introduce the *s-wave scattering length*:

$$a = -\lim_{k \to 0} \frac{\delta_0(k)}{k} \tag{1.26}$$

By using equation (1.25), we can estimate the scattering amplitude $f(\mathbf{k}, \mathbf{k}')$ in the limit $kR^* \ll 1$:

$$f(\mathbf{k}, \mathbf{k}') \approx f_0(k) = \frac{1}{k \cot \delta_0(k) - ik} \tag{1.27}$$

where we note that this expression is independent of the angle θ. We can expand in Taylor series the term:

$$k \cot \delta_0(k) = -\frac{1}{a} + \frac{1}{2} r_{\text{eff}} k^2 + ... \tag{1.28}$$

where the coefficient r_{eff} is the so-called effective range. Using equations (1.13) and (1.28), we can obtain the expression of the on-shell T-matrix for the ultracold gases:

$$\langle \mathbf{k}' | \hat{T}^{2B} | \mathbf{k} \rangle = T^{2B}(k) = -\frac{2\pi\hbar^2}{m_r} \frac{1}{k \cot \delta_0(k) - ik} \approx \frac{2\pi\hbar^2}{m_r} \frac{a}{1 - a r_{\text{eff}} k^2 + iak} \tag{1.29}$$

In terms of the small energy E we have the following expression:

$$T^{2B}(E + i\epsilon) \approx \frac{2\pi a \hbar^2}{m_r} \frac{1}{1 + ia\sqrt{2m_r E/\hbar^2} - a r_{\text{eff}} m_r E/\hbar^2} \tag{1.30}$$

and by analytic continuation, we get its off-shell expression:

$$T^{2B}(z) \approx \frac{2\pi a \hbar^2}{m} \frac{1}{1 - a\sqrt{-2m_r z/\hbar^2} - a r_{\text{eff}} m_r z/\hbar^2} \tag{1.31}$$

For $|\mathbf{k}| = |\mathbf{k}'| = k, k \to 0$, we can neglect the second term in the equation (1.28). In this way we have the following expression for the T-matrix:

$$T^{2B}(z) \approx \frac{2\pi a\hbar^2}{m_r} \frac{1}{1 - a\sqrt{-2m_r z/\hbar^2}} \tag{1.32}$$

and in particular the equation (1.32) has a pole at the negative energy:

$$E = -\epsilon_0 = -\frac{\hbar^2}{2m_r a^2} \tag{1.33}$$

Recalling equation (1.32), we have that this pole indicates the presence of a two-body bound state with a small binding energy ϵ_0. One can demonstrate that this relation turns out to be general, such that it does not depend on the specific details of the interaction potentials.

It is interesting to consider the model of the contact potential. By defining $T(\mathbf{k}', \mathbf{k}; z) = \langle \mathbf{k}' | \, T(z) \, | \mathbf{k} \rangle$, the expression (1.16) assumes the form:

$$T(\mathbf{k}', \mathbf{k}; z) = V(\mathbf{k}' - \mathbf{k}) + \int \frac{d^3k''}{(2\pi)^3} \frac{V(\mathbf{k}' - \mathbf{k}'')}{z - \epsilon_{\mathbf{k}''}} T(\mathbf{k}'', \mathbf{k}; z) \tag{1.34}$$

where $\epsilon_{\mathbf{k}} = \hbar^2 k^2/(2m_r)$. For a separable potential $V(\mathbf{k}' - \mathbf{k}) = v_0 w_k w'_k$, where $w_k = \Theta(k_0 - k)$:

$$T(\mathbf{k}', \mathbf{k}; z) = v_0 w_k w_{k'} + v_0 w_{k'} \int \frac{d^3k''}{(2\pi)^3} \frac{w_{k''}^2}{z - \epsilon_{\mathbf{k}''}} T(\mathbf{k}'', \mathbf{k}; z) \tag{1.35}$$

which, by setting $T(\mathbf{k}', \mathbf{k}; z) = w_k w_{k'} T(z)$, we have the solution:

$$T(z) = \left[\frac{1}{v_0} - \int \frac{d^3k''}{(2\pi)^3} \frac{w_{k''}^2}{x - \epsilon_{\mathbf{k}''}} \right]^{-1} \tag{1.36}$$

by setting $T(z)^{-1} = 0$, we get the following form for the contact potential:

$$\frac{1}{v_0} = \frac{m_r}{2\pi\hbar^2 a} - \int \frac{d^3k''}{(2\pi)^3} \frac{w_k^2}{\epsilon_{\mathbf{k}}} \tag{1.37}$$

this expression (that diverges for $k_0 \to \infty$) is typically used to cure the UV behaviors.

1.5 Feshbach Resonances

The main reason of the great impact of ultracold atomic and molecular quantum gases in modern physics lies, from an experimental point of view, in their extraordinary degree of control. This allows physicists to investigate the behaviour of quantum matter under very different conditions. Their interest goes beyond atomic and molecular physics, reaching far into other fields, like condensed matter, few- and many-body physics (Ref. [15] presents a detailed analysis of Feshbach resonances).

The key technique that make ultracold gases so manageable experimentally is the control of the Feshbach resonances. The Feshbach mechanism for cold alkali atoms can be easily modelled in terms of a *multi-channel scattering processes* (see Ref. [16]). Indeed, the internal atomic structure is given by the usual electronic energy levels which are split because of the hyperfine coupling and thus it is basically determined by the properties of the valence electrons and in particular their spin. As a consequence, the interaction between two atoms induces transitions between the hyperfine energy levels and thus changes the spin of such electrons. It is therefore evident that such a mechanism is conveniently described by a multi-channel Hamiltonian. In this context for a given value of the spin, one speaks of an *open channel*, when for that value of the spin a scattering process is allowed. The channel is called *closed*, if no scattering is possible and the system is described by a bound state.

The physical origin and the elementary properties of a Feshbach resonance can be understood from a simple picture. We consider two molecular potential curves $V_{bg}(R)$ and $V_c(R)$, as illustrated in Figure 1.1. For large internuclear distances R, the background potential $V_{bg}(R)$ asymptotically connects to two free atoms in the ultracold gas. For a collision process, with very small energy E, this potential represents the energetically open channel. The other potential, $V_c(R)$, representing the closed channel, is important as it can support bound molecular states near the threshold of the open channel. In this physical context, a *Feshbach resonance* occurs when the bound molecular state in the closed channel energetically approaches the

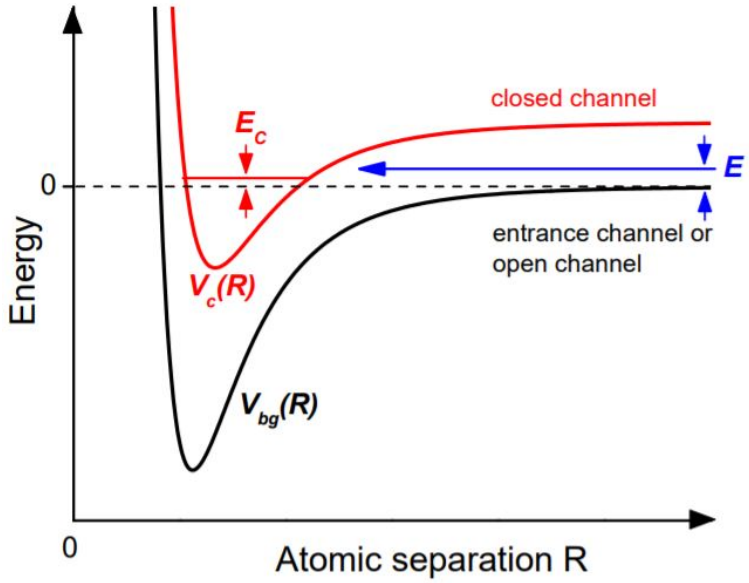

Figure 1.1: *Basic two-channel model for a Feshbach resonance. The phenomenon occurs when two atoms colliding at energy E resonantly couple to a molecular bound state with energy E_c supported by the closed channel potential. In the ultracold domain, collisions take place near zero-energy, $E \to 0$. Resonant coupling is then conveniently realized by magnetically tuning E_c near 0, if the magnetic moments of the closed and open channel differ.* Figure reproduced from Ref. [15].

scattering state in the open channel. Then even weak couplings can lead to strong mixing between the two channels. The energy differences can be controlled via a magnetic field when the corresponding magnetic moments are different. This leads to a *magnetically tuned Feshbach resonance*. The magnetic tuning method is the common way to achieve resonant coupling. Alternatively, resonant coupling can be achieved by optical methods, leading to *optical Feshbach resonances*. In general a magnetically tuned Feshbach resonance can be described by a simple expression for the s-wave scattering length a as a function of the magnetic field B:

$$a(B) = a_{bg}\left(1 - \frac{\Delta}{B - B_0}\right) \tag{1.38}$$

The background scattering length a_{bg}, which is the scattering length associated with $V_{bg}(R)$, represents the off-resonant value. It is directly related to the energy of the last-bound vibrational level of $V_{bg}(R)$. The parameter B_0 denotes the resonance position, where the scattering length diverges $(a \to \pm\infty)$, and the parameter Δ is the resonance width. Note that both a_{bg} and Δ can be positive or negative.

1.6 Notions on the scattering problem in 2D

Now we want generalize the scattering problem to the two-dimensional space. The first problem is represented by the scattering length. When we pass from 3D to 2D, the integral in equation (1.34) diverges logarithmically for $z = 0 + i\epsilon$. Consequently it would imply that the scattering length vanishes for every potential in $2D$. However, a typical length associated with the scattering at low energy can still be defined by looking at how the phase shift (or the T-matrix) vanishes at low-energy. We will show that under very general assumptions on the behaviour of the potential $V(r)$, we have a characteristic phase shift δ_0 that behaves as:

$$\delta_0(k) \approx \frac{\pi}{2\log(ka)} \quad (k \to 0). \tag{1.39}$$

We will follow mostly the treatment of Ref. [17]. The interesting reader can also take a look at Refs. [18], [19].

1.6.1 Scattering wave-function and scattering amplitude in the 2D regime

We now wish to derive the expressions for the scattering wave-function $\psi^{(+)}(\mathbf{r})$ and scattering amplitude $f(\mathbf{k}, \mathbf{k}')$ in the 2D case. The wave function for a two-body system, in its center of mass reference frame, is the solution of the Schrodinger equation:

$$(\nabla^2 + k^2)\psi(\mathbf{r}) = v(\mathbf{r})\psi(\mathbf{r}) \tag{1.40}$$

where $v(\mathbf{r}) = 2m_r V(\mathbf{r})/\hbar^2$, with m_r the reduced mass and $\mathbf{r} = (x, y)$. The equation (1.40) may be solved through the Green's function. As usual, we write down the general solution as the sum of a particular and of a solution of the associated homogeneous equation:

$$(\nabla^2 + k^2)\psi_{homo}(\mathbf{r}) = 0 \tag{1.41}$$

The homogeneous solution is a plane wave:

$$\psi_{homo}(\mathbf{r}) = Ae^{i\mathbf{k}\cdot\mathbf{r}} \tag{1.42}$$

For large distances, the scattering center must assume the form of an outgoing spherical wave, and so we need to keep the solution (1.42) with the plus sign. The particular solution is expressed in terms of the non-interacting Green's function:

$$\psi_{part}(\mathbf{r}) = \int d\mathbf{r}' G^0(\mathbf{r}, \mathbf{r}')v(\mathbf{r}')\psi(\mathbf{r}'), \tag{1.43}$$

which satisfies the differential equation

$$(\nabla^2 + k^2)G^0(\mathbf{r}, \mathbf{r}') = \delta^{(2)}(\mathbf{r} - \mathbf{r}') \tag{1.44}$$

In particular we can take the Fourier transform of (1.44) and get:

$$(k^2 - p^2)G^0(\mathbf{p}) = 1 \implies G(\mathbf{p}) = \frac{1}{k^2 - p^2} \tag{1.45}$$

By applying the Fourier transform to $G(\mathbf{p})$, one has:

$$G^0(\mathbf{r} - \mathbf{r}') = \int \frac{d^2p}{(2\pi)^2} \frac{e^{i\mathbf{p}\cdot(\mathbf{r}-\mathbf{r}')}}{k^2 - p^2} \tag{1.46}$$

The Green's function has two poles on the real axis, for $p = \pm k$. We thus add in the denominator of (1.46) a small positive imaginary shift $+i\eta$, in order to shift the the poles just off the real axis. In this way we obtain the relevant Green's function $G^{(+)}(\mathbf{r} - \mathbf{r}')$ for the scattering problem, corresponding to an outgoing wave. One has (look for example Ref. [17]):

$$G^{(+)}(\mathbf{r} - \mathbf{r}') = \int \frac{d^2p}{(2\pi)^2} \frac{e^{i\mathbf{p}\cdot(\mathbf{r}-\mathbf{r}')}}{k^2 - p^2 + i\eta} = -\frac{i}{4} H_0^1(k|\mathbf{r} - \mathbf{r}'|) \tag{1.47}$$

where $H_0^1(x)$ is the *Hankel* function of the first type.

It is fundamental in our treatment to consider the asymptotic behaviour of $G_k(|\mathbf{r} - \mathbf{r}'|)$ for large distances (low energies),:

$$G^{(+)}(|\mathbf{r} - \mathbf{r}'|) \approx -\frac{i}{4} \sqrt{\frac{2}{\pi k|\mathbf{r} - \mathbf{r}'|}} e^{i(k|\mathbf{r}-\mathbf{r}'| - \frac{\pi}{4})} \qquad |\mathbf{r} - \mathbf{r}'| \to \infty \tag{1.48}$$

So we have the following expression for the scattering wave-function $\psi_{\mathbf{k}}^{(+)}(\mathbf{r})$:

$$\psi_{\mathbf{k}}^{(+)}(\mathbf{r}) = e^{i\mathbf{k}\cdot\mathbf{r}} + \int d^2r' \int \frac{d^2p}{(2\pi)^2} \frac{e^{i\mathbf{p}\cdot(\mathbf{r}-\mathbf{r}')}}{k^2 - p^2 + i\eta} v(\mathbf{r}') \psi_{\mathbf{k}}^{(+)}(\mathbf{r}') \tag{1.49}$$

$$= e^{i\mathbf{k}\cdot\mathbf{r}} - \frac{i}{4} \int d^2r' H_0^1(k|\mathbf{r} - \mathbf{r}'|) v(\mathbf{r}') \psi_{\mathbf{k}}^{(+)}(\mathbf{r}') \tag{1.50}$$

By using the asymptotic expression (1.48), one has the following form for $\psi_{\mathbf{k}}^{(+)}(\mathbf{r})$ for large spatial distances:

$$\psi_{\mathbf{k}}^{(+)}(\mathbf{r}) \approx e^{ikz} - \frac{i}{4} \int d^2r' \left(\frac{2}{\pi k|\mathbf{r} - \mathbf{r}'|} \right)^{1/2} e^{i(k|\mathbf{r}-\mathbf{r}'| - \pi/4)} v(\mathbf{r}') \psi_{\mathbf{k}}^{(+)}(\mathbf{r}') \tag{1.51}$$

Similar to the 3D case we consider $\mathbf{k}'$ as the vector of modulus k parallel to $\mathbf{r}$. The equation (1.51) assumes the form:

$$\psi_{\mathbf{k}}^{(+)}(\mathbf{r}) \approx e^{i\mathbf{k}\cdot\mathbf{r}} - \frac{i}{\sqrt{r}} e^{-i\frac{\pi}{4}} e^{ikr} \frac{1}{2\sqrt{2\pi k}} \int d^2r' e^{-i\mathbf{k}'\cdot\mathbf{r}'} v(\mathbf{r}') \psi_{\mathbf{k}}^{(+)}(\mathbf{r}') \tag{1.52}$$

We can now generalize the scattering amplitude $f(\mathbf{k}', \mathbf{k})$ in 2D through the expression:

$$f(\mathbf{k}', \mathbf{k}) = f(k, \theta) = -\frac{1}{2\sqrt{2\pi k}} \int d^2r' e^{-i\mathbf{k}'\mathbf{r}'} v(\mathbf{r}') \psi_{\mathbf{k}}^{(+)}(\mathbf{r}') \tag{1.53}$$

such that one obtains an equation for the scattering wave-function $\psi_{\mathbf{k}}^{(+)}(\mathbf{r})$ very similar to (1.20):

$$\psi_{\mathbf{k}}^{(+)}(\mathbf{r}) = e^{i\mathbf{k}\cdot\mathbf{r}} + f(\mathbf{k}', \mathbf{k})\frac{e^{i(kr+\pi/4)}}{\sqrt{r}}, \quad r \to \infty \tag{1.54}$$

In the next subsection we will use (1.54) to study the 2D phase-shift problem. Once we will get the expressions for the phase δ_λ at $k \to 0$, we will able to define the scattering length in 2D.

1.6.2 Definition of scattering length in 2D

In the previous subsection we have derived an integral equation for the scattering wave-function. It is useful to consider now the corresponding differential equation. We thus start from the 2D Schroedinger equation:

$$-\frac{\hbar^2}{2m}\left(\frac{\partial^2\psi(\mathbf{r})}{\partial x^2} + \frac{\partial^2\psi(\mathbf{r})}{\partial y^2}\right) + V(\mathbf{r})\psi(\mathbf{r}) = E\psi(\mathbf{r}) \tag{1.55}$$

We assume that the potential is radially symmetric $V(\mathbf{r}) = V(r)$ and thus work with polar coordinates r, θ. In 3D, ψ was expressed in terms of spherical harmonics. In 2D, we simply expand the wave-function as a simple Fourier series:

$$\psi(\mathbf{r}) = \psi(r, \theta) = \sum_{\lambda=-\infty}^{\infty} C_\lambda R_\lambda(r) e^{i\lambda\theta}, \tag{1.56}$$

where λ in an integer number. By inserting equation (1.56) into equation (1.55), we get the following form for the Schrodinger equation:

$$-\frac{\hbar^2}{2m}\left(\frac{d^2}{dr^2} + \frac{1}{r}\frac{d}{dr} - \frac{\lambda^2}{r^2}\right)R_\lambda(r) + V(r)R_\lambda(r) = ER_\lambda(r) \tag{1.57}$$

We can rewrite the equation (1.57) in term of the reduced units ($v(r) = (2m/\hbar^2)V(r)$, $k^2 = (2m/\hbar^2)E$), and obtain:

$$\frac{d^2R_\lambda(r)}{dr^2} + \frac{1}{r}\frac{dR_\lambda(r)}{dr} + \left(k^2 - v(r) - \frac{\lambda^2}{r^2}\right)R_\lambda(r) = 0 \tag{1.58}$$

If one now makes the transformation:

$$R_\lambda(r) = \frac{\chi_\lambda(r)}{\sqrt{r}} \tag{1.59}$$

one gets an interesting form of the Schroedinger equation for the radial function $\chi_\lambda(r)$:

$$\frac{d^2\chi_\lambda(r)}{dr^2} + \left(k^2 - v(r) - \frac{(\lambda - \frac{1}{2})(\lambda + \frac{1}{2})}{r^2}\right)\chi_\lambda(r) = 0 \tag{1.60}$$

Here one can notice that the centrifugal term is exactly as in three dimension under the substitution $(\lambda - \frac{1}{2}) \to l$. If the potential is of circular symmetry, $\psi(\mathbf{r})$ can be expressed as:

$$\psi(r,\theta) = \sum_{\lambda=-\infty}^{\infty} i^\lambda R_\lambda(r) e^{i\lambda\theta} \tag{1.61}$$

where each $R_\lambda(r)$ satisfies the equation (1.58). When r is very large, $V(r)$ (and so $v(r)$) becomes negligible, and the Schrodinger equation (1.58) assumes the form of the standard Bessel equation:

$$x^2\frac{d^2R_\lambda(x)}{dx^2} + x\frac{dR(x)}{dx} + \left(x^2 - \lambda^2\right)R_\lambda(x) = 0 \tag{1.62}$$

where we have set $x = kr$. Thus, the general solution of (1.62) can be expressed in terms of the Bessel $J_\lambda(kr)$ and Neumann $N_\lambda(kr)$ functions:

$$R_\lambda(kr) = C_1 J_\lambda(kr) + C_2 N_\lambda(kr) \tag{1.63}$$

For reasons that will become clear later, we write the general solution $R_\lambda(kr)$ in the form:

$$R_\lambda(kr) = A_\lambda(\cos\delta_\lambda J_\lambda(kr) - \sin\delta_\lambda N_\lambda(kr)) \tag{1.64}$$

where A_λ and δ_λ are some constants to be determined.

In the limit $r \to \infty$, we can consider the following expansions for the Bessel and Neumann functions (see for example Ref. [17]):

$$J_\lambda(kr) \approx \sqrt{\frac{2}{\pi kr}}\cos\left(kr - \frac{1}{2}\pi\lambda - \frac{1}{4}\pi\right) \tag{1.65}$$

$$N_\lambda(kr) \approx \sqrt{\frac{2}{\pi kr}}\sin\left(kr - \frac{1}{2}\pi\lambda - \frac{1}{4}\pi\right) \tag{1.66}$$

By inserting equations (1.65) and (1.66) into equation (1.64), we get the asymptotic behaviour

$$\begin{aligned} R_\lambda(kr) \approx A_\lambda \sqrt{\frac{2}{\pi kr}} \Bigg[\cos\delta_\lambda \cos\left(kr - \frac{1}{2}\pi\lambda - \frac{1}{4}\pi\right) - \sin\delta_\lambda \sin\left(kr - \frac{1}{2}\pi\lambda - \frac{1}{4}\pi\right)\Bigg] \\ = A_\lambda \sqrt{\frac{2}{\pi kr}} \cos\left(kr - \frac{1}{2}\pi\lambda - \frac{1}{4}\pi + \delta_\lambda\right) \end{aligned} \tag{1.67}$$

Now it is clear the choice done for the form of the equation (1.64). In this way we have obtained a compact form of the asymptotic expression for $R_\lambda(kr)$. With a similar procedure, we can expand also the plane wave term $e^{i\mathbf{k}\cdot\mathbf{x}}$ as:

$$e^{i\mathbf{k}\cdot\mathbf{x}} = e^{ikr\cos\theta} = \sum_\lambda i^\lambda J_\lambda(kr) e^{i\lambda\theta} \approx \sqrt{\frac{2}{\pi kr}} \sum_\lambda i^\lambda \cos\left(kr - \frac{1}{2}\pi\lambda - \frac{1}{4}\pi\right) e^{i\lambda\theta} \tag{1.68}$$

The equations (1.67) and (1.68) in the (1.54) give us the following identity:

$$\begin{aligned} & f(k,\theta)\frac{1}{\sqrt{r}} e^{i\frac{\pi}{4}} e^{ikr} = \\ & \sum_\lambda i^\lambda e^{i\lambda\theta} \sqrt{\frac{2}{\pi kr}} \Bigg[A_\lambda \cos\left(kr - \frac{1}{2}\pi\lambda - \frac{1}{4}\pi + \delta_\lambda\right) - \cos\left(kr - \frac{1}{2}\pi\lambda - \frac{1}{4}\pi\right)\Bigg] \end{aligned} \tag{1.69}$$

Let us rewrite the term in the square brackets of equation (1.69). By setting $\alpha(\lambda) = -\frac{1}{2}\pi\lambda - \frac{1}{4}\pi$, we have:

$$\begin{aligned} & A_\lambda \cos(kr + \alpha + \delta_\lambda) - \cos(kr + \alpha) = \\ & \frac{1}{2} e^{i\alpha}\left(A_\lambda e^{i\delta_\lambda} - 1\right) e^{ikr} + \frac{1}{2} e^{-i\alpha}\left(A_\lambda e^{-i\delta_\lambda} - 1\right) e^{-ikr} \end{aligned} \tag{1.70}$$

where we have used the identity $\cos x = (e^{ix} + e^{-ix})/2$ in the (1.70) to write it as sum of two terms, respectively proportional to e^{ikr} and e^{-ikr}. By looking at l.h.s of (1.69), we notice that there is only a term proportional to e^{ikr}. As a consequence, the second term on the r.h.s of equation (1.70) must vanish. In this way we get the following constraint:

$$A_\lambda = e^{i\delta_\lambda} \tag{1.71}$$

Taking into account (1.71), the equation (1.70) assumes the following form:

$$\begin{aligned} A_\lambda \cos(kr + \alpha + \delta_\lambda) - \cos(kr + \alpha) &= \frac{1}{2} e^{i\alpha} \left(e^{2i\delta_\lambda} - 1 \right) e^{ikr} \\ &= i e^{i(\delta_\lambda + \alpha)} \sin\delta_\lambda e^{ikr} = (i^{-\lambda} e^{i\frac{\pi}{4}} e^{i\delta_\lambda} \sin\delta_\lambda) e^{ikr} \end{aligned} \tag{1.72}$$

where we have written the term $ie^{i\alpha} = i^{-\lambda} e^{i\frac{\pi}{4}}$. Finally, by inserting (1.72) in equation (1.69), we get the partial wave-expansion for the scattering amplitude (analogous to the equation (1.21) in 3D) :

$$f(\mathbf{k}', \mathbf{k}) = f(k, \theta) = \sqrt{\frac{2}{\pi k}} \sum_{\lambda=-\infty}^{+\infty} e^{i\delta_\lambda} \sin\delta_\lambda e^{i\lambda\theta} \tag{1.73}$$

Now we want to evaluate the explicit expression for the phase shifts δ_λ and study their variation with energy at low k. One assumes that from $r > r_0$, where r_0 is some distance, $v(r)$ is negligible, so the solution of (1.58) is given by (1.64). On the other hand, for $r < r_0$ there is one and only one solution of (1.58) which behaves regularly at $r = 0$, as long $v(r)$ does not have too singular behaviour. Let us denote by $R_{i\lambda}(r)$ this regular solution. The equation for the phase shift δ_λ is obtained simply from the requirement of regularity of the internal and external solutions at $r = r_0$. So we have to impose the equality between the two logarithmic derivatives:

$$\frac{R'_{i\lambda}(r_0)}{R_{i\lambda}(r_0)} = k \frac{\cos\delta_\lambda J'_\lambda(kr_0) - \sin\delta_\lambda N'_\lambda(kr_0)}{\cos\delta_\lambda J_\lambda(kr_0) - \sin\delta_\lambda N_\lambda(kr_0)} \tag{1.74}$$

where the symbol $'$ indicates the derivative respect to the radial coordinate r. In particular we obtain the following expression for the phase shift δ_λ:

$$\tan\delta_\lambda(k) = \frac{kR_{i\lambda}(r_0)J'_\lambda(kr_0) - R'_{i\lambda}(r_0)N_\lambda(kr_0)}{kR_{i\lambda}(r_0)N'_\lambda(kr_0) - R'_{i\lambda}(r_0)N_\lambda(kr_0)} \tag{1.75}$$

Let us study the last expression in the small energy limit. For $ka \ll 1$ one may replace the Bessel and Neumann functions, as well their derivatives, by the first term of their expansion:

$$\begin{aligned} J_\lambda(x) &= \frac{1}{\lambda!} \left(\frac{x}{2} \right)^\lambda + ... \\ N_\lambda(x) &= -\frac{(\lambda - 1)!}{\pi} \left(\frac{2}{\lambda} \right)^\lambda + ... \end{aligned} \tag{1.76}$$

For $\lambda \neq 0$, meanwhile for the $\lambda = 0$ case we have:

$$\begin{aligned} J_0(x) = 1 \qquad & J_0'(x) = -\frac{1}{2}x \\ N_0(x) = \frac{2}{\pi}\log\left(\frac{C_1 x}{2}\right) & \end{aligned} \tag{1.77}$$

where $C_1 = e^{\gamma}$, with $\gamma \simeq 0,57721$ indicates the Euler-Mascheroni constant. For the case $\lambda \neq 0$, the equation (1.76) in (1.75) gives us the following relations for $\delta_\lambda(k)$:

$$\tan\delta_\lambda(k) = -\frac{\pi}{\lambda!(\lambda-1)!}\frac{\lambda R_{i\lambda}(r_0) - r_0 R'_{i\lambda}(r_0)}{\lambda R_{i\lambda}(r_0) + r_0 R'_{i\lambda}(r_0)}\left(\frac{kr_0}{2}\right)^{2\lambda} \tag{1.78}$$

and one sees that for small k, the phase shift $\delta_\lambda(k) \propto k^{2\lambda}$ for $\lambda \neq 0$. This is analogue to the standard result for the three-dimensional case where $\delta_l(k) \propto k^{2l+1}$, provided the previous substitution $l = \lambda - \frac{1}{2}$.

However, for our purposes, it is fundamental to recover the behaviour of $\delta_0(k)$. By using equations (1.77) into (1.75), we get:

$$\begin{aligned} \tan\delta_0(k) &= \frac{\pi}{2}\frac{R'_{i0}(r_0)}{R'_{i0}(r_0)\log(C_1 kr_0/2) - R_{i0}(r_0)/r_0} \\ &= \frac{\pi}{2}\left\{\log\left[kr_0\frac{C_1}{2}\exp\left(-\frac{R_{i0}(r_0)}{r_0 R'_{i0}(r_0)}\right)\right]\right\}^{-1} \end{aligned} \tag{1.79}$$

By setting:

$$a = \frac{C_1}{2}r_0\exp\left(-\frac{R_{i0}(r_0)}{r_0 R'_{i0}(r_0)}\right) \tag{1.80}$$

and by using the Taylor expansion $\tan(x) \simeq x$ in the l.h.s. of equation (1.79), we get the behaviour of $\delta_0(k)$ at low k.

$$\delta_0(k) \approx \frac{\pi}{2\log(ka)} \qquad k \to 0 \tag{1.81}$$

As said above, the equation (1.81) is quite general (the only reasonable assumption that we have done is that the potential is independent from the polar angle θ, i.e. $V(\mathbf{r}) = V(r)$) and can be used to define the scattering length in 2D, given by the positive constant $a > 0$.

We have generalized the phase-shift formalism for a two-dimensional scattering process. At low energies we have shown that $\delta_\lambda(k) \propto k^{2\lambda}$ for $\lambda \neq$

0. On the contrary (1.81) tells us that $\delta_0(k)$ vanishes only logarithmically. So, also in 2D, we get the result that the s-wave scattering (described by $\delta_0(k)$) dominates at low energies.

Although for the δ_λ the behaviour is similar to the 3D case, the form of δ_0 at low k represents a significant feature of the 2D regime. To better understand the consequences of this fact, let us consider the scattering amplitude $f(\mathbf{k}', \mathbf{k}) = f(k, \theta)$ for $k \to 0$. Thanks to the equation (1.73), we can write:

$$f(\mathbf{k}, \mathbf{k}') \simeq \sqrt{\frac{2}{\pi k}} e^{i\delta_0} \sin\delta_0 \simeq \sqrt{\frac{2}{\pi k}} \frac{\pi}{2\log(ka) - i\pi} + o\left(\frac{1}{\sqrt{k}\log^2(ka)}\right) \qquad k \to 0 \tag{1.82}$$

where in the last equation we have used:

$$\begin{aligned} e^{i\delta_0} \sin\delta_0 = \frac{e^{2i\delta_0} - 1}{2i} &\simeq [\delta_0 + i\delta_0^2 + o(\delta_0^3)] \\ &\simeq \delta_0(1 + i\delta_0) \simeq \delta_0 \frac{1}{1 - i\delta_0} = \frac{\pi}{2\log(ka) - i\pi} \end{aligned} \tag{1.83}$$

Equation (1.82) shows that the scattering amplitude $f(\mathbf{k}', \mathbf{k})$ goes to zero at low collision energy; this is manifestly different from the 3D behaviour, where the scattering amplitude equals minus the scattering length (equation (1.27)). The low-energy behaviour has important consequences in both few- and many-body physics of the 2D gas with the short-range interactions.

Equations (1.81) and (1.82) suggest that the term $\log(ka)$ can be used to define a dimensionless scale free interaction parameter for the 2D case. For fermionic systems it is natural to characterize the system by the Fermi momentum k_F. Thus, $\log(k_F a_{2D})$ is used in many two-dimensional experiments in order to characterize the interaction (as an example one can look at the Refs. [7], [8] and [9]).

1.6.3 T-matrix in 2D and contact potential

In the previous section we have found the expressions for the scattering wave function $\psi_{\mathbf{k}}^{(+)}(\mathbf{r})$ and for the scattering amplitude $f(\mathbf{k}', \mathbf{k})$:

$$\psi_{\mathbf{k}}^{(+)}(\mathbf{r}) = e^{i\mathbf{k}\cdot\mathbf{r}} + f(\mathbf{k}', \mathbf{k})\frac{e^{i(kr+\pi/4)}}{\sqrt{r}}, \quad r \to \infty \tag{1.84}$$

$$f(\mathbf{k}', \mathbf{k}) = -\frac{1}{2\sqrt{2\pi k}} \int d^2r' e^{-i\mathbf{k}'\cdot\mathbf{r}'} v(\mathbf{r}')\psi_{\mathbf{k}}^{(+)}(\mathbf{r}') \tag{1.85}$$

where we recall that $\mathbf{k}'$ is the outgoing momentum and $\mathbf{k}$ is the incoming one.

It is convenient to discuss the scattering in the momentum space also for a 2D regime. For this purpose, we apply the Fourier transform both to the potential and to the scattering wave function:

$$\psi_{\mathbf{k}}(\mathbf{p}) = \int d^2r e^{-i\mathbf{p}\cdot\mathbf{r}} \psi_{\mathbf{k}}^{(+)}(\mathbf{r}) \tag{1.86}$$

$$v(\mathbf{p}) = \int d^2r e^{-i\mathbf{p}\cdot\mathbf{r}} v(\mathbf{r}) \tag{1.87}$$

By inserting equation (1.86) into (1.49) one gets:

$$\psi_{\mathbf{k}}(\mathbf{p}) = (2\pi)^2\delta^{(2)}(\mathbf{p}-\mathbf{k}) - \frac{1}{p^2 - k^2 - i\eta} \int \frac{d^2q}{(2\pi)^2} v(\mathbf{q})\psi_{\mathbf{k}}(\mathbf{p}-\mathbf{q}) \tag{1.88}$$

and the scattering amplitude $f(\mathbf{k}', \mathbf{k})$ assume the form:

$$f(\mathbf{k}', \mathbf{k}) = -\frac{1}{2\sqrt{2\pi k}} \int \frac{d^2q}{(2\pi)^2} v(\mathbf{q})\psi_{\mathbf{k}}(\mathbf{k}'-\mathbf{q}) \tag{1.89}$$

For convenience, we introduce the modified scattering amplitude $\tilde{f}(\mathbf{k}', \mathbf{k}) = -2\sqrt{2\pi k} f(\mathbf{k}', \mathbf{k})$:

$$\tilde{f}(\mathbf{k}', \mathbf{k}) = \int \frac{d^2q}{(2\pi)^2} v(\mathbf{q})\psi_{\mathbf{k}}(\mathbf{k}'-\mathbf{q}) = \int d^2r' e^{-i\mathbf{k}'\cdot\mathbf{r}'} v(\mathbf{r}')\psi_{\mathbf{k}}^{(+)}(\mathbf{r}') \tag{1.90}$$

By inserting eq. (1.88) into (1.90), one gets:

$$\tilde{f}(\mathbf{k}', \mathbf{k}) = v(\mathbf{k}'-\mathbf{k}) + \int \frac{d^2q}{(2\pi)^2} \frac{v(\mathbf{k}'-\mathbf{q})}{k^2 - q^2 + i\eta} \tilde{f}(\mathbf{q}, \mathbf{k}) \tag{1.91}$$

Now let us consider the Lippmann-Schwinger equation for the two-body T-matrix, generalized to the two-dimensional space

$$\begin{aligned} \hat{T}(z) = \hat{V} + \hat{V}\frac{1}{z - \hat{H}_0}\hat{T}(z) \implies \\ T(\mathbf{k}', \mathbf{k}, z) = V(\mathbf{k}'-\mathbf{k}) + \int \frac{d^2q}{(2\pi)^2} \frac{V(\mathbf{k}'-\mathbf{q})}{z - \epsilon_{\mathbf{q}}} T(\mathbf{q}, \mathbf{k}, z) \end{aligned} \tag{1.92}$$

where $T(\mathbf{q},\mathbf{k},z) = \langle \mathbf{k}'| T(z) |\mathbf{k}\rangle$ and $\epsilon_{\mathbf{q}} = \hbar^2 q^2/2m_r$. In particular it is useful to consider the on-shell form of the T-matrix $t(\mathbf{k}',\mathbf{k}) \equiv T(\mathbf{k}',\mathbf{k},z=\epsilon_{\mathbf{k}}+i\eta)$:

$$t(\mathbf{k}',\mathbf{k}) = V(\mathbf{k}'-\mathbf{k}) + \int \frac{d^2q}{(2\pi)^2} \frac{V(\mathbf{k}'-\mathbf{q})}{\epsilon_{\mathbf{k}}+i\eta-\epsilon_{\mathbf{q}}} t(\mathbf{q},\mathbf{k}) \tag{1.93}$$

A direct comparison between equations (1.91) and (1.93), gives us the relation between the on-shell T-matrix and the scattering amplitude in 2D:

$$\tilde{f}(\mathbf{k}',\mathbf{k}) = -2\sqrt{2\pi k} f(\mathbf{k}',\mathbf{k}) = \frac{2m_r}{\hbar^2} t(\mathbf{k}',\mathbf{k}) \tag{1.94}$$

which in turn yields So by inserting the equation (1.82) in the (1.94)

$$t(\mathbf{k}',\mathbf{k}) = -\frac{\hbar^2}{m_r}\sqrt{2\pi k} f(\mathbf{k}',\mathbf{k}) \approx \frac{2\pi\hbar^2}{m_r} \frac{1}{-2\log(ka)+i\pi} + o(\frac{1}{\log^2(ka)}) \quad (k\to 0) \tag{1.95}$$

The above equation is general; it is valid for both attractive and repulsive potentials and it allows one to define the scattering length directly in terms of the asymptotic behaviour of $t(\mathbf{k}',\mathbf{k})$ for small k. Note that in Eq. (1.95), the knowledge that the corrections to the leading order behaviour are of order strictly higher than $\frac{1}{\log^2(ka)}$ is crucial to fix the value of the scattering length.

The idea is now to exploit Eq. (1.95) to deal with the limiting case of a contact potential. As in 3D, a contact potential can be defined as the limit of a short-range attractive potential, when its range $r_0 \to 0$ and the strength of the attraction is changed simultaneously in order to keep the scattering length fixed at some constant value a. Since in 2D every attractive potential is sufficient to produce a bound state, the scattering length of a contact potential can, in turn, be related to the binding energy of the unique bound state supported by the contact potential. In order to see it, it is convenient to consider the contact potential as the appropriate limit of a separable potential. Let us consider the expression for the T-matrix $T(\mathbf{k}',\mathbf{k};z) = \langle \mathbf{k}'| T(z) |\mathbf{k}\rangle$:

$$T(\mathbf{k}',\mathbf{k};z) = V(\mathbf{k}'-\mathbf{k}) + \int \frac{d^2k''}{(2\pi)^2} \frac{V(\mathbf{k}'-\mathbf{k}'')}{z-\epsilon_{\mathbf{k}''}} T(\mathbf{k}'',\mathbf{k};z) \tag{1.96}$$

For a separable potential of the form $V(\mathbf{k}' - \mathbf{k}) = v_0 w_k w_{k'}$ where $w_k = \theta(k_0 - k)$, it becomes:

$$T(\mathbf{k}', \mathbf{k}; z) = v_0 w_k w_{k'} + v_0 w_{k'} \int \frac{d^2k''}{(2\pi)^2} \frac{w_{k''}^2}{z - \epsilon_{\mathbf{k}''}} T(\mathbf{k}'', \mathbf{k}; z), \tag{1.97}$$

which, by setting $T(\mathbf{k}', \mathbf{k}; z) = w_k w_k' T(z)$ leads to:

$$T(z)\left(1 - v_0 \int \frac{d^2k''}{(2\pi)^2} \frac{w_{k''}^2}{z - \epsilon_{\mathbf{k}''}}\right) = v_0 \tag{1.98}$$

and we find the solution $T(z)$:

$$T(z) = \left(\frac{1}{v_0} - \int \frac{d^2k''}{(2\pi)^2} \frac{w_{k''}^2}{z - \epsilon_{\mathbf{k}''}}\right)^{-1} \tag{1.99}$$

One can check that for every value of $v_0 < 0$ there is one and only one solution of the equation $T(z)^{-1} = 0$, with z real and negative. It is known that the poles of the T-matrix along the negative real axis correspond to the energies of bound states. Let then $z = -\epsilon_0$, with $\epsilon_0 > 0$ be such a single pole. One thus has the equation:

$$\frac{1}{v_0} = -\int \frac{d^2k}{(2\pi)^2} \frac{w_k^2}{\epsilon_0 + \epsilon_{\mathbf{k}}} \tag{1.100}$$

So we have just found a way to express the bare potential v_0 in terms of the binding energy ϵ_0 for a given value of the cutoff k_0. By letting then $k_0 \to \infty$, we have obtained the T-matrix for a contact potential in 2D:

$$T(z) = -\left[\int \frac{d^2k}{(2\pi)^2} \frac{z + \epsilon_0}{(z - \epsilon_{\mathbf{k}})(\epsilon_0 + \epsilon_{\mathbf{k}})}\right]^{-1} \tag{1.101}$$

By performing the integration in the above equation, we obtain:

$$T(z) = -\frac{2\pi\hbar^2}{m_r} \frac{1}{\log\left(\frac{-z}{\epsilon_0}\right)} \tag{1.102}$$

We can now evaluate the on-shell t-matrix $t(\mathbf{k}, \mathbf{k}') = T(z = \hbar^2 k^2/(2m_r) + i\epsilon)$ from the expression of $T(z)$ that we have just recovered:

$$\begin{aligned} t(\mathbf{k}, \mathbf{k}') &= -\frac{2\pi\hbar^2/m_r}{\log[-\hbar^2 k^2/(2m_r\epsilon_0) - i\epsilon]} \\ &= -\frac{2\pi\hbar^2/m_r}{\log[\hbar^2 k^2/(2m_r\epsilon_0)] - i\pi} \end{aligned} \tag{1.103}$$

By comparing equation (1.103) with the behaviour of the on-shell t-matrix at low energy given by (1.95), we find the important result:

$$\epsilon_0 = \frac{\hbar^2}{2m_r a^2} \tag{1.104}$$

i.e. the relation between the binding energy ϵ_0 and the scattering length defined by (1.39) is the same as in the 3D case.

1.7 Experimental tools to achieve a quasi-2d gas with cold atoms

The experimental realization of a 2D ultracold gas is based on a strongly anisotropic trap with one tightly confined direction, for example z, and two other directions, x and y, where the system is much less confined. The z-degree of freedom can be neglected if the energy gap Δ_z between the ground state and the first excited state of the z motion is much larger than all relevant energy scales, such as thermal energies, interaction energies etc. . Since the confinement along z is usually generated by a harmonic potential, with a frequency ω_z, the gap is given by $\Delta_z = \hbar\omega_z$.

Then when the z degree of freedom is thermodynamically frozen, the atoms perform zero point motion in the harmonic oscillator ground state in the vertical direction, and the extent of their wavefunction equals the harmonic oscillator length $l_z = \sqrt{\hbar/m\omega_z}$. However, the typical length scale r_0 of the van der Waals interaction potential is much smaller than l_z and therefore the microscopic scattering processes has to be described in three dimensions, by a 3D contact potential on the scale of the problem.

As a result, the interactions are *quasi*-2D rather than 2D because at distances $\ll l_z$ the wavefunction of colliding atoms is determined by 3D scattering length a_{3D}.

Scattering process, however, are altered by the 2D confinement and it becomes possible to describe the scattering physics in terms of a quasi-2D scattering length a_{2D}^q as a function of the usual three-dimensional scattering length a_{3D}. The scattering problem in the confined geometry was treated in

Ref. [20]. Here, we are only interested in reporting the main results, without going into too much detail about this complicated problem.

In [20] it is shown that the general expression (1.54) for the wavefunction of the scattering state remains valid, and can be used for both pure 2D and quasi-2D collisions. The only difference between these two regimes is given by the expressions for the scattering amplitudes. In Section 1.6.2, we have recovered that for a "pure" 2D geometry, the scattering amplitude f_{2D} is given by (1.82):

$$f_{2D}(k, a_{2D}) = -\frac{1}{\sqrt{8\pi k}} \frac{4\pi}{-2\log(k a_{2D}) + i\pi} \tag{1.105}$$

The scattering amplitude for a quasi-2D gas confined to the harmonic oscillator ground state along the z-direction is [20]:

$$f_{2D}^{(q)}(k, a_{3D}, l_z) = -\frac{1}{\sqrt{8\pi k}} \frac{4\pi}{\sqrt{2\pi} l_z / a_{3D} + w(k^2 l_z^2/2)} \tag{1.106}$$

where the function $w(\xi)$ is defined by the following limit:

$$w(\xi) = \lim_{J\to\infty} \left[\sqrt{\frac{4J}{\pi}} \log\left(\frac{J}{e^2}\right) - \sum_{j=0}^{J} \frac{(2j-1)!!}{(2j)!!} \log(j - \xi - i0) \right] \tag{1.107}$$

The equation (1.105) is obtained in the limit $k \to 0$. So we have to consider the same low-energy limit also for the equation (1.106) or, equivalently for $k^2 l_z^2 \ll 1$ (which is equivalent to consider relative energies $\epsilon < \hbar\omega_z$, which precisely defines the so-called quasi-2D regime). The behaviour of the function $w(\xi)$, for $\xi \ll 1$ is the following:

$$w(\xi) = -\log(2\pi\xi/A) + i\pi \tag{1.108}$$

where $A = 0.905$. Inserting equation (1.108) in equation (1.106), we get the following expression:

$$f_{2D}^{(q)}(k, a_{3D}, l_z) = -\frac{1}{\sqrt{8\pi k}} \frac{4\pi}{\sqrt{2\pi} l_z / a_{3D} - \log(\pi k^2 l_z^2 / A) + i\pi} \tag{1.109}$$

Equations (1.105) and (1.109), valid in the limit $k \to 0$, have now similar expressions. This allows one to write the two-dimensional scattering length

a_{2D} in terms of the harmonic oscillator length l_z and the three-dimensional scattering length a_{3D}. This parametrization of the quasi-2D scattering in terms of a_{2D} is fundamental to relate quasi-2D ultracold-atom experiments to theoretical models formulated for purely 2D systems. By comparing equations (1.105) and (1.109), we get the following expression for a_{2D}:

$$a_{2D} = l_z \sqrt{\frac{\pi}{A}} \exp\left(-\sqrt{\frac{\pi}{2}} \frac{l_z}{a_{3D}}\right). \tag{1.110}$$

The scattering in the quasi-2D geometry can thus be descibed in terms of a purely 2D model when the relevant momentum scale k of the colliding atoms is such that $k^2 l_z^2 \ll 1$.

Equation (1.110) is particularly interesting: it shows that the effective 2D scattering length a_{2D} may be controlled by changing either a_{3D} or l_z. This fact opens up the possibility of varying the 2D scattering length a_{2D} in two different ways: by controlling a_{3D} through for example a Feshbach resonance or alternatively by varying ω_z (but keeping $\hbar\omega_z$ much larger than any energy scale, in order to remain in a quasi-2D regime).

1.8 Example of quantum simulations with ultracold gases in 2D: the BKT transition in bosonic and fermionic gases

As an example how dimensionality plays a main role in the properties of a quantum phase transition, let us consider the two-dimensional Bose gas.

It is common knowledge that is impossible to reach Bose-Einstein condensation in a uniform 2D system. In particular the answer is negative, both for the ideal and the interacting gas. Indeed in the reduced dimensionality, the long-range order does not appear at any finite temperature due to thermal fluctuations of the order parameter.

This fact can be understood by studying the behaviour of the first-order correlation function $g_1(\mathbf{r}) = \langle \hat{\Psi}^\dagger(\mathbf{r}) \hat{\Psi}(0) \rangle$, where $\hat{\Psi}(\mathbf{r})$ is the annihilation operator for a bosonic particle at position $\mathbf{r}$. As shown in Ref. [21], the function $g_1(\mathbf{r})$ always tend to zero for $r \to \infty$ and it is true for any temperature.

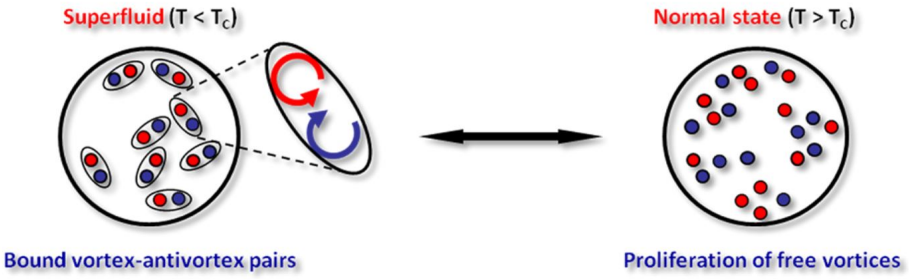

Figure 1.2: *The microscopic BKT mechanism at the origin of the 2D superfluid transition. Below the BKT critical temperature (left figure), vortices of opposite circulation are bound into dipole pairs. As the transition point is approached, the density of the pairs grows and the average pair size diverges. Just above the transition temperature (right figure), a plasma of free vortices forms and suppresses superfluidity.*

However, one can also show that the destruction of the long-range order is only marginal in 2D, in the sense that at low temperatures, $g_1(\mathbf{r})$ decays only *algebraically* with distance (meanwhile at high T it follows an exponential shape). So, in this way an interacting Bose gas at low T exhibits the so-called "quasi-long-range order" and in particular show a superfluid state.

This fact led to an unusual phase transition which (in an *infinite* Bose system) results in superfluidity without condensation, that is described by the Berezinskii-Kosterlitz-Thouless (BKT theory in brief). It represents a phase transition, described by the two-dimensional (2D) XY model in statistical mechanics, from bound vortex-antivortex pairs at low temperature to unpaired vortices and anti-vortices at some critical temperature, indicated in literature with T_{BKT}. In other words, the superfluid phase is destroyed via proliferation of vortices, where in the 2D XY-model, vortices represent stable configurations. In Figure 1.2 is represented schematically the BKT-process.

It provides a specific phenomena for two dimensional system and can experimentally observed in trapped two dimensional gas.

The BKT mechanism is very different from the usual finite-temperature phase transition. It does not involve any spontaneous symmetry breaking

and emergence of a spatially uniform order parameter.

Instead, the low temperature phase is associated with a quasi-long-range order, with the correlations of the order parameter (for example the macroscopic wave function of a Bose fluid). The BKT transitions, for these reasons, becomes the first known phase transition with nontrivial topology. The References [21] and [22] describes in a more accurate way the BKT process.

In particular in [21] is stressed that the BKT process takes place of condensation only for infinite Bose gas. In practice for real systems the distinction between BKT and (conventional) BEC transitions can be quite subtle, because no experimental systems are infinite in size. As addressed in Ref. [21], the BKT superfluid the phase of the wavefunction is not uniform in space, but the phase correlations decay extremely slowly and in practice span the whole experimental system. Ironically, this means that BKT superfludity inevitably also leads to a finite condensate fraction, and the emergence of a BEC can in fact be used as a signature of the BKT transition. The key distinction however is that in contrast to the "conventional" BEC, which is a purely statistical phenomenon and does not rely on interactions, this BKT-induced condensation is fundamentally interaction driven (the Ref. [21] provides a more detailed analysis of the competion between BEC and BKT). However BKT-theory and general topological phase transitions do not represent the only aims to quantum simulate 2D physics through ultracold gases.

In a parallel way, the search of theoretical explanation of high-T_c superconductivity in cuprate materials is one of the main open questions in modern condensed matter physics. Although scientists can explain the process behind more conventional lower-temperature superconductivity, they are still trying to work out how the phenomenon can take place at high temperatures in what are essentially 2D materials (cuprates being made up of layers of copper oxide). Such low-dimensional materials are prone to fluctuations that prevent the long-range coherence thought to be essential for superconductivity.

This has led to an increasing focus on 2D Fermi gases, because they can serve as model systems to try and help clear up this mystery, having strong

and tuneable correlations between their constituent fermions that can mimic interactions in superconductors. In particular these 2D fermionic systems (in general composed by ^{6}Li atoms) shows a Fermi-to-Bose crossover, i.e. at enough strong interaction fermions pair into 2D Bose dimers (analogue to the formation of the Cooper pairs in conventional superconductivity). This process can be seen as the generalization of the BCS-BEC crossover (already treated in 3D) in a 2D regime (see [23] for a general review).

Even in 3D, the crossover region is difficult to describe theoretically and in 2D the presence of quantum fluctuations complicates the problem (in particular the BKT process comes into play). So, a full consistent theory of 2D Fermi-to-Bose crossover must be able to describe the physical behaviour including also the fluctuations due to the intrinsic disorder of 2D regime. Once this goal is achieved, 2D Fermi gas could be a promising platform to quantum simulate high-T_c superconductivity.

As said above in the past decade, several experiments involving ^{6}Li atoms are been performed in quasi-2D regime, in order to understand how strongly correlated 2D systems can give rise to unconventional superconductivity with high critical temperatures. Let us discuss some results of experimental works.

A signature of Cooper-pair condensation has been observed in [7]. An equally populated mixture of ^{6}Li atoms in two spin states has been studied near the 3D Feshbach resonance, with a population $N = 4 - 5$ x 10^4 atoms per spin state. The kinematics is restricted by confining in a disc-shaped trap with the anisotropy ratio $\omega_z/\omega_r \simeq 310$ and an axial oscillator length $l_z = \sqrt{\hbar/m\omega_z} \simeq 551\ nm$.

In the lower panel (A) of Figure 1.3 are shown the measurements of the 2D density distribution $n(\mathbf{r})$ in the trap, meanwhile in the panel (B) is shown the evolution in the radial potential, after that the z-confinement is turned off. All the measurements are performed at the lowest attainable temperatures.

The in-trap images show the reduction of the gas as the interaction between the ^{6}Li atoms is increased. Anyway the most interesting result is in the lower panel (B) of Figure 1.3: it shows the obtained pair momentum

distributions for the coldest attainable temperature at different interaction strengths. One observes a dramatic enhancement at low momenta which manifests itself in a sharp central peak. The evolution in the panel (B) can be interpreted as Bose condensation of atomic pairs. However it is possible that the experiments proves signatures of superfluidity. In such expansion, nearly all momentum is released along the tightly confined direction, with almost no momentum released radially. Superfluid expansion, therefore, may also produce sharp peaks similar to those of the panel (B) of Figure 1.3. Therefore, the experiment [7] may be observing onset of superfluidity or quasicondensation rather than condensation.

The same group also points out that the temperature, at which the peak appear, coincides with the temperature of the BKT transition, measured in the Ref. [8]. The paper [8] reports also the measurement of the first-order correlation $g_1(\mathbf{r})$ in the Fermi-to-Bose crossover, as function of the temperature. The experimental setup and techniques are essentially the same of [7]. The first order correlation function $g_1(\mathbf{r})$ is derived from the measured momentum distribution $n(\mathbf{k})$:

$$g_1(\mathbf{r}) = \int d^2k n(\mathbf{k}) e^{i\mathbf{k}\cdot\mathbf{r}} \tag{1.111}$$

The result of such measurement of the correlation function is shown in the upper panel of Figure 1.3, at $\log(k_F a_{2D}) \simeq -0.5$ and $\log(k_F a_{2D}) \simeq 0.5$ respectively (the crossover-region is in the range $-1 \leq \log(k_F a_{2D}) \leq 1$). The only parameter which is varied in the experiment is the dimensionless temperature $t = T/T^0_{BEC}$, where $T^0_{BEC} = \sqrt{6N}\frac{\hbar\omega_r}{\pi k_B}$ is the condensation temperature of an ideal 2D Bose gas (in the harmonic potential).

One can appreciate that at lower temperatures the decay of $g_1(\mathbf{r})$ is algebraic, i.e. $g_1 \propto r^{-\eta(T)}$ with a temperature-dependent exponent $\eta(T)$, while at high T the correlation function decays exponentially. The transition from exponential to power low decay signals the onset of superfluidity.

The results obtained in [7] and [8] (pair condensations and algebraically decaying correlations at low temperatures) support the presence of a superfluid behaviour of ^{6}Li atoms, although a direct observation of superfluid flow has not yet been made. At this purpose, we finally mention a very

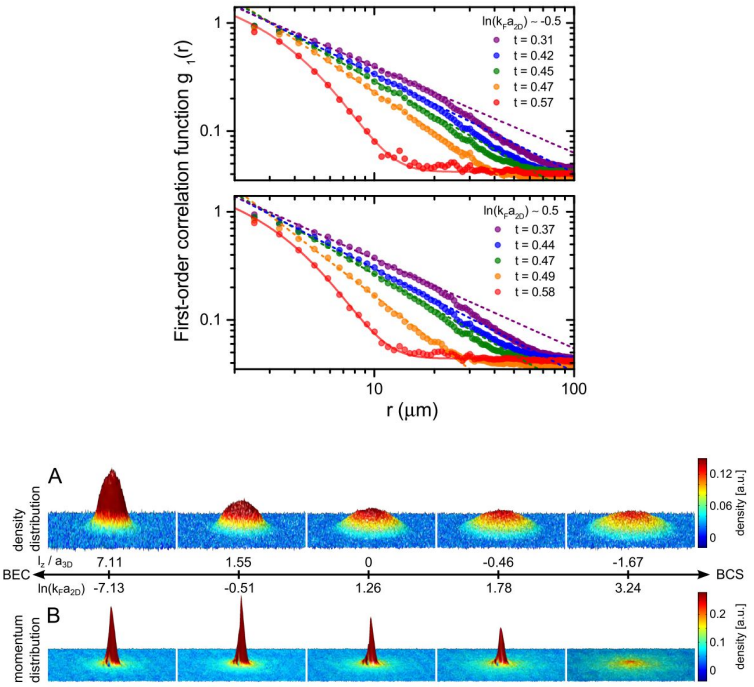

Figure 1.3: Upper Figure: *First-order correlation functions* $g_1(r)$ *for different temperatures at* $\log(k_F a_{2D}) \simeq -0.5$ *and* $\log(k_F a_{2D}) \simeq 0.5$. *The temperature scale used here is* $t = T/T^0_{BEC}$. *At high temperatures correlations decay exponentially as expected for a gas in the normal phase. At low temperatures. algebraic correlations* ($g_1(r) \propto r^{-\eta(T)}$) *with a temperature-dependent scaling exponent* $\eta(T)$. Figure reproduced from [8]. Lower Figure: *(A) In situ density distribution obtained from absorption along the z-axis. (B) Pair momentum distribution obtained from the* $\tau/4$ *(for more details look at Ref. [7]) with a pair projection ramp to* $l_z/a_{3D} = 7.11$, *corresponding to a magnetic field of B= 692 G. The strong enhancement at low momenta in the momentum distribution function for* $\log(k_F a_{2D}) < 3.24$ *is a clear signature of pair condensation.* Figure reproduced from [7]

.

recent experimental work that may prove in a more direct way the presence of superfluidity in a 2D Fermi gas. In Ref. [9], superfluidity is demonstrated (always through a mixture of a 2D ^{6}Li atoms) by moving a periodic potential through the system and observing no dissipation below a critical velocity v_c. The critical velocity is measured as function of the interaction parameter $\log(k_F a_{2D})$, finding a maximum in the crossover regime between fermionic and bosonic regime. The three papers [7], [8] and [9] underline the growing attention of the physics on ultracold atoms on 2D quantum systems. The 2D Fermi gases potentially may be represent an ideal platform to get a full consistent comprehension of the influence of the BKT mechanism and the origin of high-T_c superconductivity in the 2D regime.

Chapter 2

Previous studies of Bose-Fermi mixtures with BF pairing interaction

Bose-Fermi mixtures with a tunable boson-fermion attraction have been object of active theoretical and experimental investigation over the last few years. The main behaviour of this quantum system is represented by the formation of molecules between bosons and fermions. As a consequence, the condensation of bosons is completely suppressed (even at $T = 0$), for mixtures where the boson density n_B is lower that the fermion density n_F. In this chapter we will see how this physical picture emerges within a many-body diagrammatic formalism based on the sum of the so-called "ladder diagrams". We start our discussion by presenting some theoretical works at finite temperature.

2.1 Bose-Fermi mixtures in 3D at finite temperature

The first theoretical studies of ultracold Bose-Fermi mixtures focused on non-resonant system, where boson-fermion pairing is irrelevant. These systems have been studied through mean-field like treatments, in particular

their tendency towards collapse or phase separation.

Ref. [3] represents our starting point to discuss resonant Bose-Fermi mixture. Such work considers a homogeneous mixture composed by single-component fermions and bosons. The attraction between bosons and fermions is assumed to be tuned by a broad Fano-Feshbach resonance, as in most of experiments with ultracold gases, and thus be accurately described by an attractive point-contact potential. The ultraviolet divergences associated with the use of a contact potential are eliminated by expressing the bare interaction v_0 in terms of the boson-fermion scattering length a_{BF} through the divergent expression $1/v_0 = m_r/(2\pi a) - \int d\mathbf{k}/(2\pi)^3 2m_r/\mathbf{k}^2$, which compensates analogous divergences arising in perturbation theory. No interactions between bosons is taken into account (even though it becomes relevant in the treatment of stability of the system), while a Fermi-Fermi s-wave scattering length is excluded by Pauli principle. In this physical context, the system is described by a *minimal* Hamiltonian (see equation (1) in the reference [3] and similar to equation (3.1) in Chapter 3 , with integrations performed over 3D momenta). The parameter in these theoretical approach that regulates the pairing attraction between bosons and fermions is the s-wave scattering length a_{BF}. In addition, one can consider another natural length scale of this system, the Fermi momentum $k_F = (6\pi^2 n_F)^{1/3}$ or alternatively a fictitious Fermi momentum $k_F = (3\pi^2 n)^{1/3}$, where $n = n_B + n_F$. It is useful in this framework to define the dimensionless coupling parameter $g = (k_F a_{BF})^{-1}$, to describe the strength of the interaction.

The expected behavior of the system is trivial in the opposite regimes of the boson-fermion couplings. In the weak-coupling limit, where the scattering length a_{BF} is small and negative (such that $((k_F a_{BF})^{-1} \ll 1)$), the two components behave essentially as ideal Bose and Fermi gases. More interestingly, in the strong coupling limit, with a_{BF} small and positive (such that $(k_F a_{BF})^{-1} \gg 1$), bosons and fermions will form bound states of molecular composite fermions, with a binding energy of $\epsilon_0 = 1/(2m_r a_{BF}^2)$. This effect results particularly strong in mixtures prepareted with $n_F > n_B$. In fact, by increasing the interaction, the number of bosons bounded in the molecular states with fermions increases, until all bosons will pair with fermions into

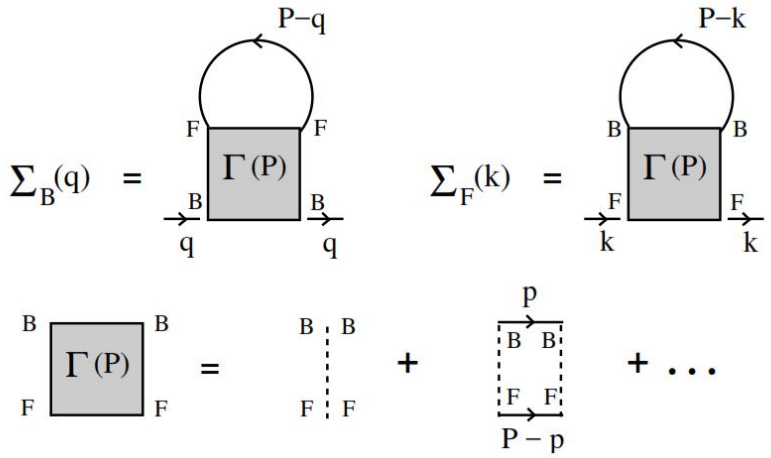

Figure 2.1: *T-matrix diagrams for the fermionic and bosonic self-energies in the normal phase. Full lines represent bare bosonic and fermionic Green's function. Broken lines represent the bare boson-fermion interaction* v_0. Figure reproduced from [3].

molecules. This Bose-Fermi pairing affects also the boson condensate. For sufficiently strong couplings, even at $T = 0$, the condensate fraction can be suppressed completely.

In this context the ladder-diagrams approach proves very effective to describe the evolution between these two regimes. The physical quantity that collects all these diagrams is called *T-matrix*. By knowing the T-matrix one can in principle evaluate the self energies, to build up the dressed Green's function to get the observables. In the T-matrix formalism for Bose-Fermi mixtures these observables are the bosonic and fermionic momentum distribution functions and densities. In the Ref. [3] are considered the following diagrams, reported in Figure 2.1.

The choice of the self-energy diagrams is motivated by recovering the two correct physical behaviours in the two above limits, in completely analogy with previous work on the BCS-BEC crossover (see Ref. [24]). This is because in the weak-coupling limit the T-matrix self-energy yields the leading order correction to the non-interacting system in powers of the small pa-

rameter na_{BF}^3. At the same time, in the strong-coupling limit, the T-matrix becomes proportional to the bare Green's function of the molecule of the composite fermion (see for example Eq.(7) in [3]). As a consequence, by increasing the interaction to reach the molecular limit, the chemical potential μ_B becomes more and more negative and tends to minus the binding energy ϵ_0, as expected when all bosons pair with fermions. On the contrary the fermionic potential μ_F remains almost constant.

In general, for intermediate couplings, the problem needs to be solved numerically. In the work [3], particularly interesting is the study of how the critical temperature T_c for condensation varies as function of the coupling strength. The critical temperature is very close to the non-interacting value in the weak-coupling regime. By increasing the interaction, the critical temperature becomes lower and lower. At a certain critical values g_c, T_c vanishes, corresponding to a quantum phase transition, which separates a phase with a condensate and a phase with molecular correlations sufficiently strong to deplete completely the condensate density. The authors find that the critical coupling depends weakly on the value of the density imbalance n_B/n_F. Figure 2.2 reports the behaviour of μ_F, μ_B and of the critical temperature T_c discussed above.

Subsequent theoretical works on Bose-Fermi mixtures in 3D have further explored the very peculiar properties of this quantum system. The next step taken in [4] was the study of mass-imbalanced Bose-Fermi mixtures. The general behaviour of the critical temperature as function of the coupling is similar to what found in the equal-mass case. The critical temperature T_c decreases and vanishes at a certain coupling g_c. Above this value, the BEC is completely suppressed in favor to the formation of molecules. In particular the weak dependence of g_c with respect to density imbalance is also confirmes. A minor difference is the global behaviour of T_c: contrary to the mass-balanced case, a weak maximum in the critical temperature is found at intermediate coupling, with a value of the maximum slightly above the non-interacting value T_0. This feature is more pronounced for intermediate values of the density imbalance.

Regarding the behaviour of the two chemical potentials μ_B and μ_F at the

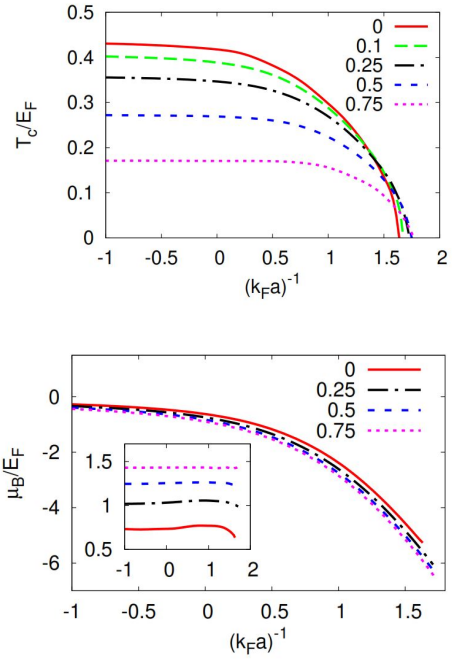

Figure 2.2: *Upper panel: the temperature T_c as function of $(k_F a_{BF})^{-1}$ Lower panel: the chemical potentials μ_B and μ_F (inset) as function of $(k_F a_{BF})^{-1}$.* Figures reproduced from Ref. [3].

critical temperature T_c, they present a trend similar to the mass-balanced case. The bosonic chemical potential decreases rapidly with increasing attraction, and changes from $\mu_B \approx 2\pi n_F a_{BF}/m_r$ for weak couplings to $\mu_B \approx -\epsilon_0$ for strong couplings, with a small dependence on n_B/n_F. The fermionic chemical potential changes little and remains almost constant. This is because the decrease of the chemical potential μ_F due to the attractive interaction within bosons is partially compensated by the decreasing of the temperature when moving along the critical line (which increases μ_F) and by the Pauli repulsion between unpaired fermions and Bose-Fermi molecules.

So in general for any mass ratio, the behaviour of the critical temperature as a function of the boson-fermion dimensionless coupling evidences the presence of a quantum phase transition at zero temperature. This transition is between a superfluid associated with the presence of a boson condensate and a normal phase where the condensate is completely depleted.

We now pass to discuss a very interesting behaviour of the bosonic momentum distribution function $n_B(\mathbf{k})$, which occurs for values of the imbalance sufficiently large. One can see in Fig. 2.3 that the bosonic momentum distribution function vanishes identically at low momenta. This empty region extends from $\mathbf{q} = 0$ until a certain value, that depends only by the density imbalance.

The physical reason for this peculiar behaviour can be understood as follows. For a large imbalance so (that is, for $n_F \gg n_B$) most fermions remain unpaired and fill a Fermi sphere of radius $k_{UF} \simeq [(n_F - n_B)/6\pi^2]^{1/3}$. At couplings $g > g_c$ the bosons are instead bound into molecules, which fill a Fermi sphere with a radius $P_{CF} \simeq (n_B/6\pi^2)^{1/3}$. Now, the region in momentum space $|\mathbf{k}| < k_{UF}$ is already occupied by the unpaired fermions. As a consequence only fermions with $\mathbf{k} > k_{UF}$ are bounded in molecules. Since the momentum of the molecules is given by the sum $\mathbf{P} = \mathbf{q} + \mathbf{k}$, the two previous conditions $|\mathbf{P}| < P_{CF}$ and $|\mathbf{k}| > k_{UF}$ imply that only bosons with $|\mathbf{q}| > q_0 = k_{UF} - P_{CF}$ belongs to the pairs, leaving empty the region $|\mathbf{q}| < q_0$. It has been verified that the values of q_0 obtained numerically are compatible with the equation $q_0 = k_{UF} - P_{CF}$. This very peculiar

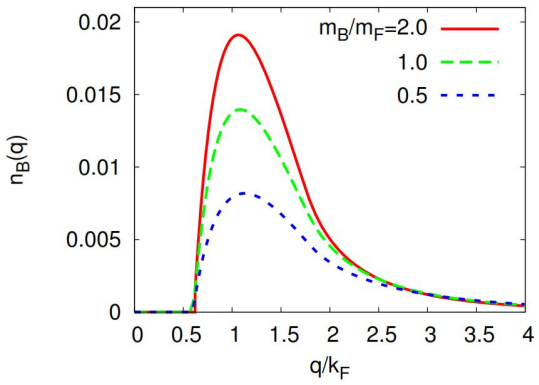

Figure 2.3: *bosonic distribution functions at the critical coupling g_c, for the density imbalance $(n_B - n_F)/(n_B + n_F) = 0.75$.* Figure reproduced from Ref. [3]

.

phenomena which occurs for Bose-Fermi mixtures was called *indirect Pauli exclusion effect* (introduced in Ref. [4]).

Ref. [25] provides a more precise study of this effect from an analytical point of view. In the same work the indirect Pauli exclusion effect was confirmed also by quantum Monte-Carlo simulations. A more detailed comparison between the two methods is shown in the reference [26], for mixtures with different values of $x = n_B/n_F$. This comparison shows how the T-Matrix formalism represents an efficient approach to describe the pair correlation appearing in the Bose-Fermi mixture.

2.2 Generalization of the T-matrix self-energy to the condensed phase at $T = 0$

In general the works that we have discussed so far represent a detailed description of the molecular limit of the Bose-Fermi mixture. The method of the T-matrix formalism is able to describe the mixture for temperatures $T > T_c$, where T_c is the condensed temperature. In particular it predicts the total depletion of the condensate, because T_c vanishes at a certain critical value g_c.

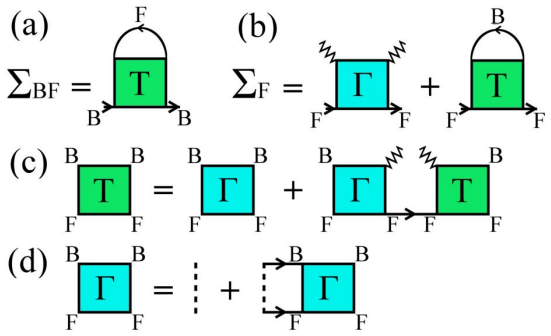

Figure 2.4: *Feynman diagrams extended to include the condense phase: Full lines indicate the B and F propagators, while wavy-lines indicate condensed lines.* Figure reproduced from Ref. [5].

Subsequent works [25],[26] studied Bose-Fermi mixtures in the molecular limit exactly at $T = 0$, confirming that a sufficiently strong BF attraction suppresses completely the boson condensate (a result which could only be extrapolated in the previous works formulated at finite temperature).

Ref. [5] finally extended the T-matrix approach to the condensed phase.

This approach introduces a new T-matrix (indicated with T) which corresponds to an infinite series of the ladder series of diagrams (Γ) (see Fig. 2.4). In this way, the theory takes into account all possible ladder diagrams where the boson line are either condensed or normal.

The diagrams for the two self-energies Σ_B and Σ_F are similar to those of the reference [3]. The main difference is that the usual term is now build up with the T-matrix T. In addition, the bosonic normal self-energy includes also the term $8\pi a_{BB} n_0/m_B$, given by the Bogoliubov theory at $T = 0$ for a dilute interacting Bose gas (see [27] for major details).

The fermionic self-energy is due only to the coupling with bosons. In this case, the T-matrix can be closed in the diagram either with a boson propagator or with two condensate insertions. The second choice, however, produces in general *improper* self-energy diagrams, except for the first diagram of T (i.e., the diagram for which $T = \Gamma$). So, in order to avoid double-counting in the Dyson's equation, it is necessary to replace the T-matrix T with Γ, when

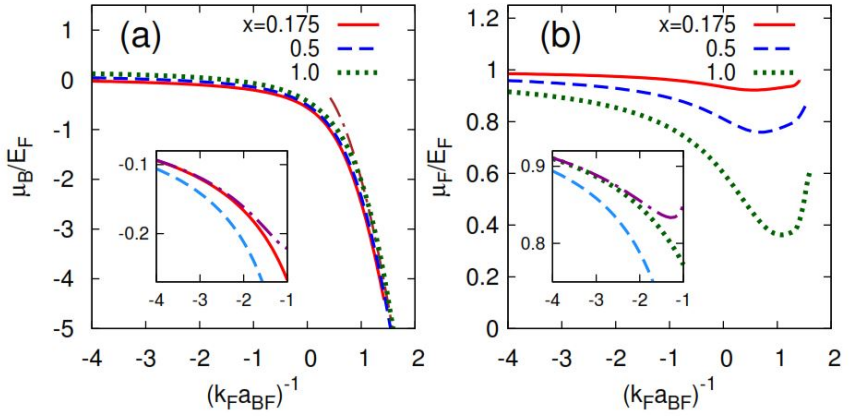

Figure 2.5: *(a) Bosonic chemical potential μ_B vs $(k_F a_{BF})^{-1}$ for $m_B = m_F$, $\eta = 3x10^{-3}$ and different values of $x = n_B/n_F$. Dashed-dotted line: $-\epsilon_0$ (b) Fermionic chemical potential μ_F for same parameters. Insets: comparison at $a_{BB} = 0$ with first (dashed) and second order (dashed-dotted) perturbative results in weak coupling for (a) μ_B at $x = 0.175$ (b) μ_F at $x = 1$..* Figures reproduced from the reference [5].

T is closed by two condensate insertions. This explains the first diagram in the Figure 2.4 in the panel(b).

Similarly to [3], the self-energies build up the dressed Green's function, which is used in tirn to evaluate the two momentum distributions and the two densities for Bosons and Fermions. Besides the two equations for the densities, there is now an additional one, that is the Hugenholtz-Pines relation $\mu_B = \Sigma_{11}(0) - \Sigma_{12}(0)$. In this way this improved T-Matrix approach is able to describe also the weak coupling regime, and above all the intermediate regime $|k_F a_{BF}| \geq 1$ where perturbation theory fails.

Figure 2.5 reports the two chemical potential μ_B and μ_F (normalized to the Fermi energy $E_F = k_F^2/2m_F$) as a function of $g = (k_F a_{BF})^{-1}$. The data are obtained by solving the T-matrix equations for $m_B = m_F$, $\eta = 3x10^{-3}$ and three different values of $x = n_B/n_F$. The chemical potential μ_B tends to the mean field value $4\pi a_{BB} n_0/m_B$ in the weak-coupling limit $(k_F a_{BF})^{-1} \ll -1$, while it approaches minus the value of the binding energy, $-\epsilon_0$, in the molecular limit in completely analogy with the previous works [3]. More-

over, by taking a look on the inset, one can see that μ_B approaches also the second order perturbative expression $\mu_B = 2\pi a_{BF} n_F / m_r (1 + 3 k_F a_{BF}/(2\pi))$ (dashed-dotted line). The fermionic chemical potential μ_F, as the attraction is increased, first decreases, following the second order perturbative expression $\mu_F = E_F + 2\pi a_{BF} n_B / m_r (1 + 2 k_F a_{BF}/\pi)$ in the weak coupling limit (as shown in the inset) and then increases when the critical coupling g_c is approached. In complete analogy with [4], this behaviour for moderate couplings suggests a repulsion between unpaired fermions and the BF molecules, similar to that occurring in the molecular limit. But the central finding of this generalized T-matrix approach is given by the results for the population of the condensate n_0. Figure 2.6 reports n_0/n_B vs. $(k_F a_{BF})^{-1}$ for different x and constant $\eta = n_B a_{BB}^3$. The main result is that the curves evaluated for different concentrations n_B/n_F overlap each other, showing a sort of universal behaviour. Deviations occur only for values $n_0/n_B \leq 0.2$ very close to g_c (where, in addition, the condensed phase could be replaced by a phase-separated state according to the phase diagram of Ref. [28]).

This occurs not only for the balanced-mass case, but also for mass ratios $m_B/m_F \neq 1$. Specifically, the insets of Figure 2.6 report examples for $m_B/m_F = 5$ and $m_B/m_F = 23/40$ (this latter value corresponds to the mass ratio of a ^{23}Na-^{40}K mixture, that represents the mixture considered in the experiment of Ref. [6]).

Quantum Monte-Carlo simulations reported in the same work [5] confirm this universal behaviour for $x \leq 0.5$, with results very close to those obtained by the T-matrix approach. Finally, the results for the whole momentum distribution $n_B(k)$ obtained by the two different methods were compared in [5]. The corresponding results are reported in Figure 2.7 and confirm, once again, the validity of the T-matrix formalism. This very good agreement will motivate us to extend the same formalism to the study Bose-Fermi mixtures in 2D.

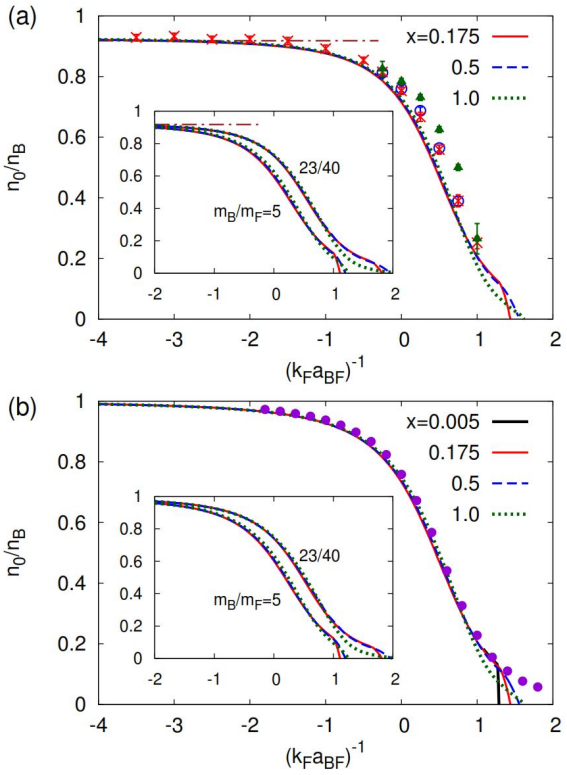

Figure 2.6: *(a) Bosonic chemical potential μ_B vs $(k_F a_{BF})^{-1}$ for $m_B = m_F$, $\eta = 3x10^{-3}$ and different values of $x = n_B/n_F$. Dashed-dotted line: $-\epsilon_0$ (b) Fermionic chemical potential μ_F for same parameters. Insets: comparison at $a_{BB} = 0$ with first (dashed) and second order (dashed-dotted) perturbative results in weak coupling for (a) μ_B at $x = 0.175$ (b) μ_F at $x = 1$.* . Figure reproduced from Ref. [5]

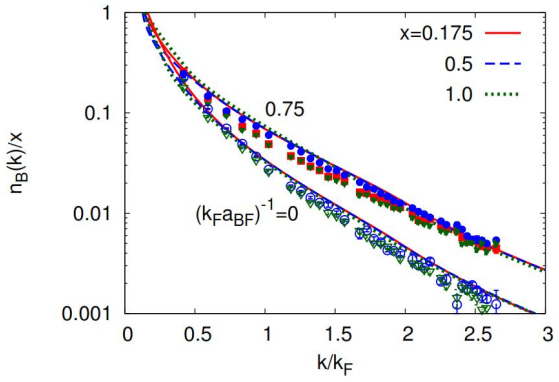

Figure 2.7: *Bosonic momentum distribution function divided by x vs. k for $m_B = m_F$, $\eta = 3x10^{-3}$,$(k_F a_{BF})^{-1} = 0, 0.75$ and different values of x. Curves: TMA results. Symbols: QMC data $x = 0.175$ (crosses),0.5 (circles), 1 (triangles).* Figure reproduced from Ref. [5].

2.3 Recent experimental results for a BF-mixture in 3D

In the previous sections we have discussed how the T-matrix formalism is able to capture rather well the quantum phase transition between the condensed phase and the normal phase with molecules. In spite of the intrinsic approximation of selecting just a class of Feynman diagrams, the T-matrix approach compared extremely well with Quantum Monte Carlo *ab initio* simulations.

We will now discuss very recent experimental results [6] that further confirm the validity of the T-matrix diagrammatic approach.

A double-degenerate Bose-Fermi mixture of ^{23}Na and ^{40}K, has been studied in [6] by using a novel density-decompression technique, which mitigates atomic loss[1].

The experiment starts with 2.3×10^5 ^{40}K atoms at a temperature $T = 80$ nK ($\simeq 0.2\, T_F$, where T_F is the Fermi temperature) and a BEC of 0.8×10^5

[1]The regime of equal density is hard to control experimentally: the excess density of the Bose-Einstein condensate causes fast interspecies loss.

^{23}Na atoms with a condensate fraction of 60% at a magnetic field of 81 G.

A single magnetic field ramp with a speed of 3.5 G/ms is terminated at the final value of magnetic field around 78.3 G, close to a Feshbach resonance, tuning in this way different values of the interaction strength $g = (k_F a_{BF})^{-1}$. It is found that the depletion of the BEC is independent of the ramp speed for sufficiently slow ramps (see the Supplemental Material of [6]). The magnetic field is then quenched at the value 72.3 G.

This process is used to measure the intensity of pairing BF-correlations, forcing the formation of molecules already before the phase transition. The higher the number of molecules generated, the more intense the pairing-correlations before the quench. After this procedure the system results composed of free Na atoms and bound NaK molecules, which are then imaged in time of flight after Stern-Gerlach separation. The results are shown in Figure 2.8 in the panels (a) and (b).

Thus, the signatures of the phase transition a from a polaronic condensate to a molecular Fermi gas are described quantitatively by defining the normalized order parameter $\phi = N_{BEC}/(N_m + N_{BEC})$, where N_{BEC} is the number of condensed Na atoms and N_m is the number of the molecules. Clearly ϕ has the role of order parameter and describes the condensate fraction, which can be depleted due to the quantum excitation of bosons to finite-momentum states. The majority of these finite-momentum states are due to the formation of pairing correlations, which are measured, as said above, by the projection into molecules [2].

The measurements of ϕ were thus directly compared with the predictions of the condensate fraction obtained with the T-matrix approach of Ref. [5]. Figure 2.9 shows the measured order parameter ϕ as a function of $g = (k_F a_{BF})^{-1}$ for $n_B/n_F = 0.9$ and 1.3. One can appreciate from the Figure 2.8 that ϕ slowly decreases by increasing the coupling until $(k_F a_{BF})^{-1} < 0$. On the contrary, once the scattering length becomes positive, the order parameter decreases rapidly and vanishes in the regime beyond $(k_F a_{BF})^{-1} = 1.43$ where the residual condensate fraction is compa-

[2] In Ref. [6] the definition of ϕ does not take into account the number of thermal Na atoms, whose number remains mostly unchanged across the full interaction range

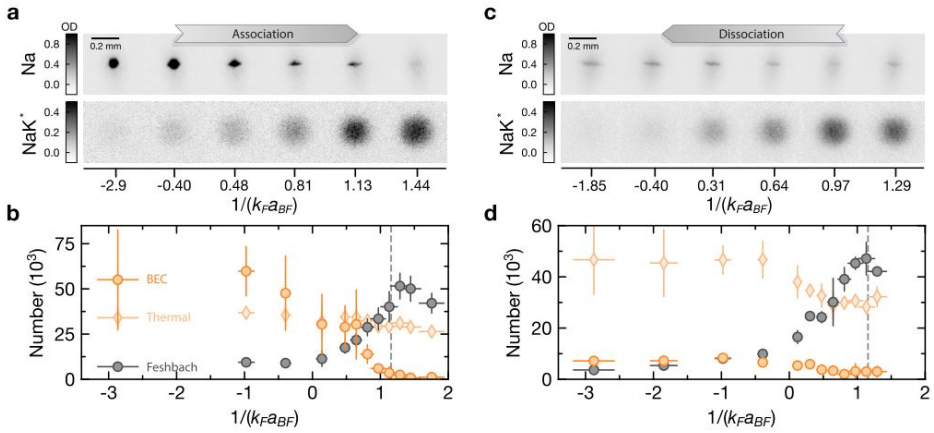

Figure 2.8: *(a) Absorption images of Na atoms (Na) and induced molecules (NaK*) after 18 ms time of fight during the association ramp from the BEC to the molecular phase. (b) Production of induced molecules. Number of condensed Na atoms (dark orange points), thermal Na atoms (bright orange diamonds) and induced molecules (gray points) is shown as function of* $(k_F a_{BF})^{-1}$ *for* $n_B/n_F = 1.3$*. The grey line indicates the BEC-to-molecule transition at* $(k_F a_{BF})^{-1} = 1.16$ *in the Fermi polaron problem (C) Absorption images during the dissociation ramp with 18 ms time of flight. (d) Dissociation of the induced molecules (reversal of the phase transition). Condensed Na atoms(dark orange points), thermal Na atoms (bright orange diamonds) and induced molecules (gray points) are shown as a function of* $(k_F a_{BF})^{-1}$ *for* $n_B/n_F = 1.3$*).* Figure reproduced from [6].

rable to the uncertainty of the measurement. One can see in figure 2.9 that, throughout the full interaction regime, there is indeed a very good agreement between the experimental measurements and the predicted condensate fraction of Ref. [5], corresponding to the black line.

It is important to stress that both data sets (for $n_B/n_F = 0.9$ and $n_B/n_F = 1.3$) overlap within error bars, confirming the universality of the condensate depletion with respect to the values of n_B/n_F that was first predicted in [5].

In order to estimate the transition point independently from the order parameter, the number of projected molecules was also used as an indicator for BF-pairing correlations. When the parameter $g = (k_F a_{BF})^{-1}$ increases, as is shown in Figure 2.8, the number of projected molecules increases until a saturation value is reached. It is the signal that all bosons are bounded into molecules. The resulting transition point is estimated to be $(k_F a_{BF})^{-1} = 1.29(13)$, which is consistent with the transition point obtained by the vanishing of the order parameter. The data collected show a conversion rate around 80% of the Na atoms in the BEC into molecules.

The reversal of the phase transition was also studied. Once the ramp has reached the value of $(k_F a_{BF})^{-1} = 1.3$, the magnetic field is decreased to dissociate the molecules. Then the dissociation ramp is again followed by a magnetic-field-quench at 72.3 G for the detection. As can be seen from the time-of-flight images in Figure 2.8, the number of projected molecules decreases, and at the same time a finite BEC fraction is recovered. Quantitatively, the number of the Na atoms in the BEC can be increased from $3(2) \times 10^3$ to $8(1) \times 10^3$.

In the dissociation processes an increase of thermal Na atoms is registered, which is attributed to the non-adiabatic effects generated by the magnetic field ramps near the transition point. As a consequence, the reversal phase transition cannot be characterized by the same order parameter ϕ, due to the change of the number of thermal Na atoms.

However, the partial restoration of the BEC is a signal of the dissociation of the molecules due to the decreasing of the coupling, in line with the expected phase transition. So these measurements provide an experimental

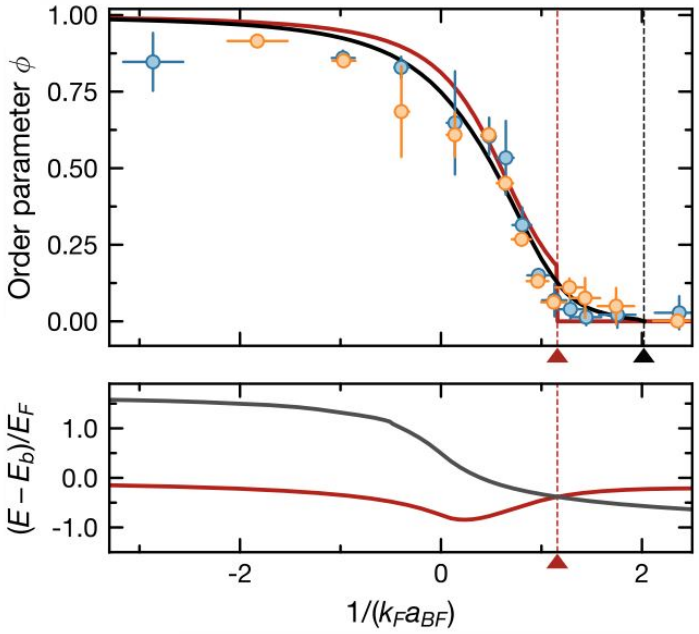

Figure 2.9: Upper Figure: *Order parameter ϕ measured in [6] as function of the coupling parameter $(k_F a_{BF})^{-1}$ for the boson-fermion ratio $n_B/n_F = 0.9$ (orange points) and $n_B/n_F = 1.3$ (blue points). The black solid line shows the order parameter from the $T = 0$ theory in* Ref. [5] *predicting the QPT to occur at $(k_F a_{BF})_c^{-1} = 2.02$ (black triangle) with $n_B/n_F = 1$.* Lower Figure: *Energy spectrum of the zero-momentum Fermi polaron (red line) and the zero-momentum molecule (gray line) for a single bosonic impurity obtained from the fRG. The energies cross at the polaron-to-molecule transition (red-dashed line). For values $a_{BF} > 0$, the binding energy $E_b = \hbar^2/2m_r a_{BF}^2$ is subtracted where m_r is the reduced mass.* Figures reproduced from Ref. [6].

support for the previous theoretical works for BF mixtures, in particular with that carried out in Ref. [5]. In particular, the competition between condensation and pairing-correlations that leads to the formation of the BF molecules is evident from both the measured order parameter in Figure 2.9 and the induced-molecular process in Fig. 2.8.

Although the experiment has been realized at the finite temperature $T = 0.2\ T_F$, it shows signatures of a quantum phase transition from the condensate to the molecular phase that may occur strictly at $T = 0$, as shown in the previous works [3], [4], [5].

2.3.1 Comparison between T-matrix and fRG calculations in the polaronic limit

The T-matrix approach of [5], in the polaronic limit ($n_B/n_F \to 0$, i.e. a single impurity immersed in a Fermi sea), predicts the polaron-to-molecule transition to occur at $(k_F a_{BF})^{-1} = 1.60$. For finite bosonic densities, this value increases, and in general the phase transition occur for values $(k_F a_{BF})^{-1} > 1.60$. Specifically for the case of balanced densities and mass-ratio $m_B/m_F = 23/40$ (corresponding to the Na-K mixture considered in [6]), it predicts a $g_c = (k_F a_{BF})^{-1} = 2.02$. The T-matrix approach, however, only takes into account single particle-hole excitations of the Fermi sea and underestimates the modification of the binding energy of molecules inside the many-body environment. Indeed, by applying the T-matrix approach to the Fermi-polaron problem and $m_B = m_F$, one finds the polaron-to-molecule transition to occur at $(k_F a_{BF})^{-1} = 1.27$. More accurate techniques for the polaron problem, such as the functional renormalization group (fRG) and the Quantum Monte Carlo (QMC) predict, in the same case, the value $(k_F a_{BF})^{-1} = 0.90$. For this reason, in order to obtain a more precise value of the critical g_c for the heteronuclear case of the mixture ^{23}Na-^{40}K in the polaronic limit, a fRG scheme was used in [6]). With this procedure, it is possible to obtain the polaron and molecule energies, that are shown in the lower panel of Figure 2.9. The two graphs cross each other at $(k_F a_{BF})^{-1} = 1.16$. However, as can be seen from Figure 2.9, the polaron and molecule energies cross at rather shallow angle (see upper panel of Figure 2.9), implying

that the critical value in the polaronic limit can be affected by a sizable uncertainty. According to [6], the value of $(k_F a_{BF})^{-1} = 1.16$ obtained in the polaronic impurity limit represents a lower bound on the true value of the critical coupling of the quantum phase transition at $g_c = (k_F a_{BF})_c^{-1}$. Consistently with the universality of the condensate fraction predicted in [5], and its connection with the polaron quasiparticle weight, which was also first understood in [5], one sees in Figure 2.9(a) that the polaron quasi-particle weight (red curve) obtained with the fRG approach in the impurity limit, describes already rather well the condensate fraction (except for the discontinuity of the polaron-to-molecule transition). The main reason for the different predictions for the polaron-molecule transition between the fRG and T-matrix approaches in the single-impurity limit is the overestimation of the repulsion between the molecule and the surrounding fermions in the Fermi sea. On the contrary, the quasiparticle weight is less affected, and the two methods (fRG and T-matrix) give a similar result in the single impurity case. This is important, because it supports the expectation that the T-matrix formalism should give accurate predictions for the condensate fraction also at finite bosonic densities.

2.4 2D Bose-Fermi mixtures and p-wave superfluidity

One of the most fascinating and difficult challenges of modern condensed matter physics is the full understanding of topological quantum systems.

Among these topological quantum systems, the $p_x + ip_y$ superfluid represents a particularly interesting system, realized in ^{3}He and possibly in superconducting Sr_2RuO_4. The increasing interest in topological quantum behaviour (and also in high-T_c superconductivity) has led physicists to looking for more robust and controllable setups. The main reason lies in the possibility of having a full experimental control of the interesting topological properties of this paradigmatic phase, such as Majorana modes or non-Abelian vortices.

As usual ultracold gases represent the ideal environment to perform this

search, in particular for their success in the verification of the BEC-BCS crossover in two-component Fermi gases.

The expected similar crossover between spinless fermions with a p-wave attraction is expected to be fundamentally different and more interesting from an experimental point of view. Theoretically speaking, it has been shown that by increasing the attraction a transition from the weakly coupled topological $p_x + ip_y$ phase to the topologically trivial strongly-coupled phase of dimers may arise (see Ref. [29] for review).

The main experimental problem is represented by the recombination in three-body clusters, or possibly higher-order correlations that can significantly modify the physical behaviour of the system. In particular these systems suffers three-body losses. So, from the experimental point of view, the target is to create p-wave superfluidity with inelastic loss-processes under control.

This problem was studied by Bazak and Petrov in Ref. [10]. The inelastic recombination can be suppressed, if the p-wave attraction extends much beyond the recombination region. In it is in this context that the study of the Bose-Fermi mixture plays a very important role to realize the experimental background to reach p-wave superfluidity. In particular there are several reasons that make the study of the two-dimensional case more interesting than the three-dimensional one. Following Ref. [10], consider a Bose-Fermi mixture with a Bose-Fermi attraction which supports a weakly bound Bose-Fermi (BF) molecular state.

Consider now two identical fermions in the mixture: the exchange of a boson leads to an effective attraction between the fermions, inversely proportional to the bosonic mass m_B. On the other hand, the Fermi-Dirac statics gives rise to an effective centifugal repulsion $\propto l(l+1)/m_F R^2$ in three dimensions and $\propto l^2/m_F R^2$ in two dimensions, with l odd integer and R represents is the distance between the fermionic atoms. As a result of this competition, if one consider the mass ratio m_F/m_B, there exist a critical value $(m_F/m_B)_c$ such that one effect dominates with respect to the other one. In fact, above the value $(m_F/m_B)_c$, the attraction between two fermions due to the exchange of a boson becomes more intense with respect

to the centrifugal barrier and there appears a trimer state with angular momentum l. In 3D, the $l = 1$ trimer appears above $(m_F/m_B)_c = 8.2$, while in 2D one can show that this number decreases $(m_F/m_B)_c = 3.3$. Below this critical value, the system is characterized by an atom-molecule attraction in the p-wave channel.

Consider now two BF molecules. Then, the presence of the second boson approximately doubles the exchange attraction and one expects a p-wave molecule-molecule resonance to appear at roughly half the mass ratio discussed above for two fermions and a boson. The main reason that makes the 2D case more interesting with respect to the 3D case is that the last one is subject to inelastic losses. This problem is studied in detail, again by Petrov, in [30] and is due to the fact that, in the three-dimensional space, the FBB is an Efimovian system.

On the contrary in 2D, the p-wave interaction becomes resonant for $1 \leq m_F/m_B \leq 2$. This is fundamental because it makes it possible to study effects of strong p-wave interactions in accessible isotopic mixtures. A low-energy collision between two BF molecules can lead to the creation of FFB or FBB trimers. As mentioned above, the FFB trimer state is absent for $(m_F/m_B) < 3.3$. The FBB trimer is instead possible, and is also stable because its energy is always below the molecule-molecule threshold $2E_{BF}$. However, a weak BB repulsion (specifically $a_{BB}/a_{FB} > 7.65 \times 10^{-9}$ for $m_F/m_B = 1$ and $a_{BB}/a_{FB} > 3.2 \times 10^{-22}$ for $m_F/m_B = 2$) is sufficient to make this state energetically forbidden.

By considering even clusters of higher orders Bazak and Petrov show in their work [10] that, for a sufficiently strong Boson-Boson repulsion, two- and three-molecule collisions are elastic. This result is fundamental, because it makes it possible in principle, to obtain a stable gas of BF molecules, without any more complicated cluster-states.

Since the BF bound state is a fermionic particle, this means that the s-wave interaction is suppressed by Pauli principle, so the p-wave interaction between molecules is dominant. In addition, the reduced dimensionality provides the possibility to tune independently the the boson-boson and boson-fermion scattering lengths a_{BB} and a_{BF}. In the same experiment

one can think to control one scattering length with a Fano-Feshbach resonance and the other one with a confinement-induced resonance (described in Section 1.7).

An independent tuning of the BB interaction and the BF interactions could be the key point to have a mechanically stable Bose-Fermi mixture for a wide range of BF couplings, that represents an important issue for the experiments.

Chapter 3

T-matrix approach for a Bose-Fermi mixture in 2D

The main scope of the thesis is to extend the T-matrix approach also in the 2D regime. In particular we will consider the same set of Feynman diagrams of Ref. [5] previously developed in 3D. Contrary to the more standard theories at $T = 0$ which work with Green's functions defined on the real frequency axis (see, e.g., Chapters 3-4 and 6 of Ref. [31]), the theory that we will consider is formulated at zero temperature by taking the $T \to 0$ limit in all relevant equations obtained within the finite temperature (Matsubara) formalism (Chapter 7 in [31]), keeping in this way imaginary frequencies. Working also at $T = 0$ with imaginary frequencies is useful to avoid the singularities (or nearly singularities) of the Green's functions calculated along the real frequency axis.

3.1 The system

The system of interest is represented by a mixture of single-component fermions (F) with density n_F and bosons (B) with density n_B. In the presence of a broad Fano-Feshbach resonance, the effective range of the potential r_0 is much smaller than the average interparticle distance and the boson-fermion (BF) scattering length a_{BF}. Under this condition, the system is de-

scribed by a minimal Hamiltonian, where the boson-fermion interaction can be described by an attractive point-contact potential. The grand-canonical Hamiltonian is then:

$$\begin{aligned} H = \sum_{s=B,F} \int d\mathbf{r} \psi_s^\dagger(\mathbf{r}) \Big(-\frac{\nabla^2}{2m_s} - \mu_s \Big) \psi_s(\mathbf{r}) \\ + v_0^{BF} \int d\mathbf{r} \psi_B^\dagger(\mathbf{r}) \psi_F^\dagger(\mathbf{r}) \psi_F(\mathbf{r}) \psi_B(\mathbf{r}) \\ + \frac{1}{2} v_0^{BB} \int d\mathbf{r} \int d\mathbf{r}' \psi_B^\dagger(\mathbf{r}) \psi_B^\dagger(\mathbf{r}') \psi_B(\mathbf{r}') \psi_B(\mathbf{r}) \end{aligned} \tag{3.1}$$

where $\psi_s^\dagger$ creates a particle of mass m_s and chemical potential μ_s, where $s = B, F$ indicates the bosonic and fermionic species respectively. The terms v_0^{BF} and v_0^{BB} are the bare contact strengths. From this moment on we set $\hbar = k_B = 1$ in all equations. The use of a contact interaction introduces ultraviolet divergences in perturbation theory that can be eliminated by expressing the bare coupling strength v_0^{BF} in terms of the boson-fermion binding energy $\epsilon_0 = 1/(2m_r a_{BF}^2)$ through the Eq. (1.100):

$$\frac{1}{v_0^{BF}} = -\int \frac{d^2k}{(2\pi)^2} \frac{1}{\frac{\mathbf{k}^2}{2m_r} + \epsilon_0} \tag{3.2}$$

where $m_r = m_B m_F/(m_B + m_F)$ is the reduced mass of the boson-fermion system and $\mathbf{k}$ is the 2D momentum. The BF interaction is attractive and tunable from weak to strong couplings, while the BB interaction is assumed to be weakly repulsive. As a consequence, the BB interaction will be treated at the level of the Bogoliubov approximation, which is not plagued by the UV divergences arising at higher order in perturbation theory. In analogy to experiments for 2D fermionic systems, we then describe the BF-coupling regimes by defining the dimensionless parameter $g = -\log(k_F a_{BF})$ where $k_F = \sqrt{4\pi n_F}$ is the 2D-Fermi momentum. In terms of g, we have *weak* BF-attraction for $g \lesssim -2$, while *strong* BF-attraction for $g \gtrsim 1$. The molecular limit is obtained in the regime $g \gg 1$, such that $a_{BF} \to 0$.

3.2 T-matrices for the normal and condensed phase in 2D

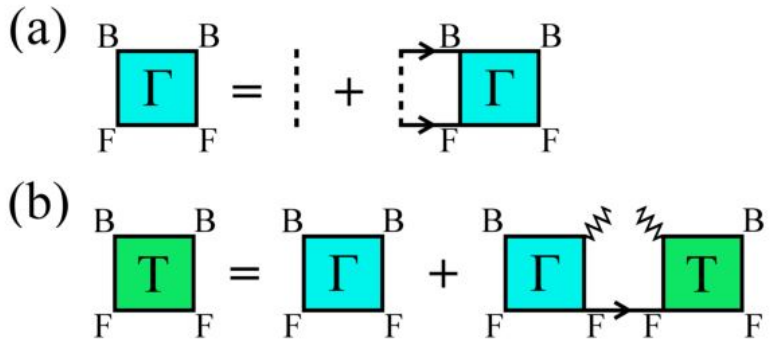

Figure 3.1: *Diagrams of the T-matrix* $\Gamma(\boldsymbol{P},\Omega)$ *in the normal phase (a) and of the T-matrix* $T(\boldsymbol{P},\Omega)$. Figure reproduced from Ref. [5].

In our treatment we work with two different T-matrices. The first one, indicated by $\Gamma(\mathbf{P},\Omega)$ describes the propagation of a fermion-boson pair where all boson lines are out of the condensate. The second one, i.e., $T(\mathbf{P},\Omega)$, describes the propagation of a fermion-boson pair where at least one normal boson line is replaced by condensate insertions. The ladder series of diagrams for $\Gamma(\mathbf{P},\Omega)$, represented in Fig. 3.1a, corresponds to the following algebraic equation:

$$\Gamma(\mathbf{P},\Omega) = v_0^{BF} - v_0^{BF}\Gamma(\mathbf{P},\Omega)\int \frac{d^2q}{(2\pi)^2}\int_{-\infty}^{+\infty}\frac{d\omega}{2\pi}G_F^0(\mathbf{P}-\mathbf{q},\Omega-\omega)G_B^0(\mathbf{q},\omega) \tag{3.3}$$

where $G_B^0(\mathbf{q},\omega)$ and $G_F^0(\mathbf{q},\omega)$ are respectively the bosonic and fermionic bare (or non-interacting) Green's functions:

$$G_B^0(\mathbf{q},\omega) = \frac{1}{\mu_B - \frac{q^2}{2m_B} + i\omega}; \qquad G_F^0(\mathbf{q},\omega) = \frac{1}{\mu_F - \frac{q^2}{2m_F} + i\omega} \tag{3.4}$$

The integral over ω yields:

$$\begin{aligned}&\int_{-\infty}^{+\infty}\frac{d\omega}{2\pi}G_F^0(\mathbf{P}-\mathbf{q},\Omega-\omega)G_B^0(\mathbf{q},\omega) = \\ &= \int_{-\infty}^{+\infty}\frac{d\omega}{2\pi}\frac{1}{i(\Omega-\omega)-\xi^F_{\mathbf{P}-\mathbf{q}}}\frac{1}{i\omega-\xi^B_{\mathbf{q}}} = \frac{1-\Theta(-\xi^F_{\mathbf{P}-\mathbf{q}})}{\xi^F_{\mathbf{P}-\mathbf{q}}+\xi^B_{\mathbf{q}}-i\Omega}\end{aligned} \tag{3.5}$$

where $\xi^s_{\mathbf{k}} = \frac{\mathbf{k}^2}{2m_s} - \mu_s$ $(s = B, F)$, Ω is a frequency, while $\mathbf{p}$ and $\mathbf{P}$ are momenta. The equation (3.5) can be evaluated by a contour integration in the complex plane. One can easily see that the integrand has two poles: one for $\omega = -i\xi^B_{\mathbf{q}}$ and one for $\omega = \Omega + i\xi^F_{\mathbf{P}-\mathbf{q}}$. The first pole is always in the lower complex plane (corresponding to the condition $\xi^B_{\mathbf{q}} > 0$) since the bosonic chemical potential μ_B in our calculations will be always ≤ 0. The second pole can instead be situated in the upper-half or in the lower-half depending on the sign of $\xi^F_{\mathbf{P}-\mathbf{q}}$

By closing the contour in the upper complex plane, only this second pole contributes, provided $\xi^F_{\mathbf{P}-\mathbf{q}} > 0$. We thus get the result $\Theta(\xi^F_{\mathbf{P}-\mathbf{q}})(\xi^F_{\mathbf{P}-\mathbf{q}} + \xi^B_{\mathbf{q}} - i\Omega)^{-1}$ (in the last line of equation (3.5) we have used the identity $\Theta(x) = 1 - \Theta(-x)$).

Equation (3.3) yields then

$$\frac{1}{\Gamma(\mathbf{P}, \Omega)} = \frac{1}{v_0^{BF}} + \int \frac{d^2q}{(2\pi)^2} \frac{1 - \Theta(-\xi^F_{\mathbf{P}-\mathbf{q}})}{\xi^F_{\mathbf{P}-\mathbf{q}} + \xi^B_{\mathbf{q}} - i\Omega}. \tag{3.6}$$

The ultraviolet divergence of the integral Eq. (3.6) is compensated by Eq. (3.2) expressing the bare interaction v_0^{BF} in terms of the binding energy ε_0. In this way one obtains

$$\Gamma(\mathbf{P}, \Omega) = \frac{1}{\Gamma^{SC}(\mathbf{P}, \Omega)^{-1} - I_F(\mathbf{P}, \Omega)} \tag{3.7}$$

where $\Gamma^{SC}(\mathbf{P}, \Omega)$, which corresponds to the strong-coupling limit of $\Gamma(\mathbf{P}, \Omega)$ is given by

$$\begin{aligned} \frac{1}{\Gamma^{SC}(\mathbf{P}, \Omega)} = \frac{1}{v_0^{BF}} + \int \frac{d^2q}{(2\pi)^2} \frac{1}{\xi^F_{\mathbf{P}-\mathbf{q}} + \xi^B_{\mathbf{q}} - i\Omega} = \\ = -\frac{m_r}{2\pi} \log\left(\frac{\frac{P^2}{2M} - 2\mu - i\Omega}{\epsilon_0} \right). \end{aligned} \tag{3.8}$$

Note that Eq. (3.8) can be obtained from Eq. (1.102) by replacing $z = -\frac{P^2}{2M} + 2\mu + i\Omega$.

The contribution $I_F(\mathbf{P}, \Omega)$ is defined by the following integral:

$$I_F(\mathbf{P}, \Omega) = \int \frac{d^2q}{(2\pi)^2} \frac{\Theta(-\xi^F_{\mathbf{P}-\mathbf{q}})}{\xi^F_{\mathbf{P}-\mathbf{p}} + \xi^B_{\mathbf{q}} - i\Omega} \tag{3.9}$$

This integral can be solved exactly with rather laborious calculation, by using the following useful relation for the integration performed over the polar angle θ in 2D:

$$\int_0^{2\pi} \frac{d\theta}{z \pm \cos\theta} = 2\pi \frac{\mathrm{sgn}(\Re e(z))}{\sqrt{z^2-1}} \tag{3.10}$$

Here, we just report the final result for $I_F(\mathbf{P},\Omega)$. First of all we notice that the $\Theta(-\xi^F_{\mathbf{P}-\mathbf{p}})$ in the numerator of the integrand in Eq. (3.9) implies that $I_F(\mathbf{P},\Omega) = 0$ for $\mu_F \leq 0$. For $\mu_F > 0$ we have the following solution:

$$\begin{aligned}
I_F(\mathbf{P},\Omega) =& \frac{1}{4\pi\sqrt{\alpha}}\Bigg[\log\left(\beta + 2\alpha k_{\mu_F}^2 + 2\sqrt{\alpha}\sqrt{\gamma + \beta k_{\mu_F}^2 + \alpha k_{\mu_F}^4}\right) \\
& - \log(\beta + 2\sqrt{\alpha\gamma})\Bigg] \qquad \left(\text{for } \mu \leq \frac{P^2}{4m_B}\right); \\
=& -\frac{1}{4\pi\sqrt{\alpha}}\Bigg[\log\left(\beta + 2\alpha k_+^2 + 2i\sqrt{\alpha}\mathrm{sgn}(\Omega)\sqrt{\frac{P^2}{m_B}k_+^2 + \Omega^2}\right) \\
& - \log\frac{P^2}{m_B^2} - i\pi\mathrm{sgn}(\Omega)\Bigg] \\
& + \frac{1}{4\pi\sqrt{\alpha}}\Bigg[\log\left(\beta + 2\alpha k_{\mu_F}^2 + 2\sqrt{\alpha}\sqrt{\gamma + \beta k_{\mu_f}^2 + \alpha k_{\mu_F}^4}\right) \\
& - \log\left(\beta + 2\alpha k_+^2 + 2i\sqrt{\alpha}\mathrm{sgn}(\Omega)\sqrt{\frac{P^2}{m_B}k_+^2 + \Omega^2}\right)\Bigg] \\
& \left(\text{ for } \mu > \frac{P^2}{4m_B}\right)
\end{aligned} \tag{3.11}$$

where we have defined the momenta $k_{\mu_F} = \sqrt{2m_F\mu_F}$ and $k_+ = \sqrt{2m_r}\sqrt{2\mu - \frac{P^2}{m_B}}$ and the coefficients :

$$\begin{aligned}
\alpha &= \frac{1}{4m_r^2} \\
\beta &= \frac{P^2}{m_B}\left(\frac{1}{2m_r} - \frac{1}{m_B}\right) - \frac{1}{m_r}(2\mu + i\Omega) \\
\gamma &= \left(\frac{P^2}{2m_B} - 2\mu - i\Omega\right)^2.
\end{aligned} \tag{3.12}$$

It is also useful to report the solution of I_F for $P = 0$:

$$I_F(0,\Omega) = \frac{m_r}{2\pi}\log\left(\frac{1}{2}k_{\mu_F}^2 - 2m_r\mu - im_r\Omega\right) - \frac{m_r}{2\pi}\log\left(-2m_r\mu - im_r\Omega\right). \tag{3.13}$$

In particular from this latter equation we can recover the behaviour of $I_F(\mathbf{P},\Omega)$ for $\Omega \to \pm\infty$:

$$\begin{aligned} I_F(\mathbf{P},\Omega) =& \frac{m_r}{2\pi}\log\left[1 + \frac{\frac{1}{2}k_{\mu_F}^2 - 2m_r\mu}{-im_r\Omega}\right] - \frac{m_r}{2\pi}\log\left[1 + \frac{-2m_r\mu}{-im_r\Omega}\right] \\ \simeq& -\frac{m_r}{2\pi}\frac{k_{\mu_F}^2}{2im_r\Omega} = -\frac{k_{\mu_F}^2}{4\pi}\frac{1}{i\Omega} = -\frac{n_{\mu_F}}{i\Omega} \end{aligned} \tag{3.14}$$

where we have used $\log(1+x) \simeq x$ for $x \to 0$. This equation will turn out particularly useful for the numerical program, when we will have to approximate the high-frequency tails of the integrals over Ω.

The algebraic equation for the T-matrix $T(\mathbf{P},\Omega)$ in the condensed phase, corresponding to the diagrams in Fig. 2.4b is:

$$T(\mathbf{P},\Omega) = \Gamma(\mathbf{P},\Omega) + \Gamma(\mathbf{P},\Omega)n_0 G_F^0(\mathbf{P},\Omega)T(\mathbf{P},\Omega), \tag{3.15}$$

with solution:

$$T(\mathbf{P},\Omega) = \frac{1}{\Gamma(\mathbf{P},\Omega)^{-1} - n_0 G_F^0(\mathbf{P},\Omega)} \tag{3.16}$$

where n_0 is the condensate density.

Fermi momenta of the T-matrices $T(\mathbf{P},\Omega)$ and $\Gamma(\mathbf{P},\Omega)$

The T-matrix $T(\mathbf{P},\Omega)$ represents the basic building block to evaluate the self-energies and then the Green's functions in the condensed phase. So it is important to deal with its analytic properties. More precisely, it presents a Fermi jump placed at a certain momentum P_{T_1}.

It is obtained by considering the analytic continuation of $T(\mathbf{P},\Omega)$ to the retarded $T^R(\mathbf{P},\tilde{\Omega})$ via the replacement $i\Omega \to \tilde{\Omega} + i\epsilon$, with ϵ infinitesimally small and positive and $\tilde{\Omega}$ real. The Fermi step momentum is defined by the equation:

$$\Omega(\tilde{P}_{T1}) = 0 \tag{3.17}$$

with $\Omega(\tilde{P})$ obtained by the solution of the equation of

$$\Re e\, T^R(\mathbf{P}, \Omega(P))^{-1} = 0 \tag{3.18}$$

when, simultaneously:

$$\Im m\, T^R(\mathbf{P}, \Omega(P))^{-1} = 0 \tag{3.19}$$

Note that since zero frequency is at the intersection between the imaginary and real axis, the determination of of momentum P_{T_1} does not require to perform the analytic continuation. The momentum P_{T_1} can thus be obtained by solving the equation:

$$\Re e\, T(P_{T_1}, 0)^{-1} = 0, \tag{3.20}$$

since $\Im m\, T^R(\mathbf{P}, 0)^{-1} = 0$ for all $\mathbf{P}$. The momentum P_{T_1}, is fundamental in the numerical program to evaluate accurately the momentum integrals for the two self-energies and the quantity Δ^2_∞ (defined shortly below). This is because the corresponding integrands vanish sharply at P_{T_1}.

For completeness, we define an analogue momenta also for the T-matrix in the normal phase $\Gamma(\mathbf{P}, \Omega)$, as solution of the equation:

$$\Re e\, \Gamma(P_\Gamma, 0)^{-1} = 0. \tag{3.21}$$

The momenta P_Γ has no role of the optimization of the numerical program. However it is found only in the BF mixture for boson concentrations $x = n_B/n_F$ near the unitarity.

Tan's constant and Δ^2_∞

Let us now introduce a very important quantity in the theory as well as in its numerical implementation. This physical quantity is defined by considering the trace of the T-matrix $T(\mathbf{P}, \Omega)$:

$$\Delta^2_\infty = \int \frac{d^2P}{(2\pi)^2} \int \frac{d\Omega}{2\pi} T(\mathbf{P}, \Omega) e^{i\Omega\eta} \quad \eta \to 0^+ \tag{3.22}$$

where we have introduced the factor $e^{i\Omega\eta}$ which makes the integral over the frequencies convergent (since $T(\mathbf{P}, \Omega) \propto 1/\log\Omega$ for large frequencies).

The evaluation of Δ_∞^2 is fundamental to set the asymptotic behaviour of the high-frequency limit of the two self-energies $\Sigma_F(\mathbf{k},\omega)$ and $\Sigma_B(\mathbf{k},\omega)$ and for the limit $k \to \infty$ of the two distribution functions $n_F(\mathbf{k})$ and $n_B(\mathbf{k})$. In particular, Δ_∞^2 is related to the so-called Tan constant C which rules the large momentum behaviour of the momentum distributions of quantum many-body systems interacting via a contact interaction. S. Tan has proven in [32] that in these systems the large momentum behaviour is given by C/k^4, where C is the so-called contact constant C. We will see that in our case $C = 4m_r^2\Delta_\infty^2$ for fermions, while for bosons C gets a contribution also from the Bogoliubov depletion of the condensate due to the boson-boson interaction, such that $C = 4m_r^2[\Delta_\infty^2 + \Sigma_{12}^2]$.

In the strong-coupling (molecular) limit the quantity Δ_∞^2 can be also connected to the density of molecules (composite fermions) n_{CF}. Focusing on the specific case $n_B \leq n_F$, we expect that in the molecular limit the bosonic chemical potential μ_B will tend to the value $-\epsilon_0$. In addition, the condensate density n_0 will tend to zero since essentially all bosons will be paired up into molecules. We can then write:

$$T(\mathbf{P},\Omega)^{-1} \approx \Gamma(\mathbf{P},\Omega)^{-1} \approx \Gamma^{SC}(\mathbf{P},\Omega)^{-1} = -\frac{m_r}{2\pi}\log\left(\frac{\frac{P^2}{2M} - 2\mu - i\Omega}{\epsilon_0}\right) \tag{3.23}$$

In the strong coupling limit the quantity $2\mu =\simeq -\epsilon_0$, with ϵ_0 large, such that the quantity $\mu_{CF} \equiv \epsilon_0 + 2\mu \ll |2\mu|$. We thus have

$$\begin{aligned}\Gamma^{SC}(\mathbf{P},\Omega)^{-1} =& -\frac{m_r}{2\pi}\log\left(1 + \frac{P^2/2M - i\Omega}{2|\mu|}\right) + \frac{m_r}{2\pi}\log\left(1 + \frac{\mu_{CF}}{2|\mu|}\right) \\ \simeq& \frac{m_r}{2\pi}\frac{i\Omega - P^2/2M + \mu_{CF}}{2|\mu|} \simeq \frac{m_r}{2\pi}\frac{i\Omega - P^2/2M + \mu_{CF}}{\epsilon_0}\end{aligned} \tag{3.24}$$

where we have expanded the logarithms by using $\log(1+x) \approx x$ for $x \simeq 0$. So, we have just recovered that in the strong coupling limit the the T-matrix $T(\mathbf{P},\Omega)$ reduces to $\Gamma^{SC}(\mathbf{P},\Omega)$, which in turn becomes proportional to the bare Green's function $G_{CF}(\mathbf{P},\Omega)$ for the molecules

$$\Gamma^{SC}(\mathbf{P},\Omega) \simeq \frac{2\pi}{m_r}\epsilon_0\frac{1}{i\Omega - P^2/2M + \mu_{CF}} = \frac{\pi}{m_r^2 a_{BF}^2}G_{CF}^0(\mathbf{P},\Omega). \tag{3.25}$$

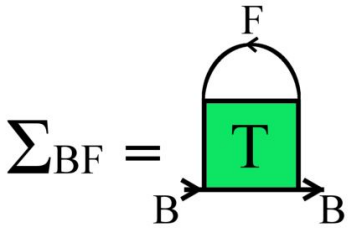

Figure 3.2: *Diagrams for the self-energy Σ_{BF}: full lines correspond to the bare fermionic (F) and to the bare boson (B) Green's functions.* Figure reproduced from Ref. [5].

The quantity $\mu_{CF} \equiv \epsilon_0 + 2\mu$ thus acquires the meaning of the chemical potential of the composite fermions.

When equation (3.25) is plugged into equation (3.22) for Δ^2_∞, one obtains:

$$\begin{aligned} \Delta^2_\infty &= \int \frac{d^2P}{(2\pi)^2} \int \frac{d\Omega}{2\pi} T(\mathbf{P},\Omega) e^{i\Omega\eta} \\ &\simeq \frac{\pi}{m_r^2 a_{BF}^2} \int \frac{d^2P}{(2\pi)^2} \int \frac{d\Omega}{2\pi} G^0_{CF}(\mathbf{P},\Omega) e^{i\Omega\eta} = \frac{\pi}{m_r^2 a_{BF}^2} n_{CF} \end{aligned} \tag{3.26}$$

We see from this equation that, also in the 2D case, the quantity Δ^2_∞ is related to the density of composite fermions n_{CF} in the strong coupling limit. For mixtures with $n_B < n_F$ one can show that n_{CF} tends to n_B in the strong-coupling limit.

3.3 Self-energies

3.3.1 Bosonic self-energy

We write down now the expression for the contribution to the bosonic normal self-energy that describes the coupling of a boson with a fermionic particle. The diagrams that we are going to consider are drawn in Figure 3.2: Full lines correspond to the bare fermionic (F) and to the bare boson (B) Green's functions.

$$\Sigma_{BF}(\mathbf{k},\omega) = \int \frac{d^2P}{(2\pi)^2} \int \frac{d\Omega}{2\pi} T(\mathbf{P},\Omega) G_F^0(\mathbf{P}-\mathbf{k},\Omega-\omega) e^{i\Omega\eta}, \qquad \eta \to 0^+ \tag{3.27}$$

where the Feynman's rules normally should give us an minus sign in front of equation (3.27), due to the presence of the fermionic loop. But this cancels off because we have included for convenience an overall minus sign in the definition of $T(\mathbf{P},\Omega)$ and $\Gamma(\mathbf{P},\Omega)$.

In addition to the term Σ_{BF} that describes the interaction between a boson particle and a fermionic particle we want to take in account also the interactions between bosons with momentum $\mathbf{k} \neq 0$ and the condensate.

A weakly interacting Bose system is described diagrammatically by a different theory respect to the fermionic particles. We remind that in bosonic systems in the presence of a condensate, there are in general three distinct self-energies. The first one (indicated usually with Σ_{11}) has one particle line going in and one coming out, similar to the fermionic case.

The other two self-energies have two particle lines either coming out (Σ_{12}) or going in (Σ_{21}) and this underlines the difference with respect to fermions, due to the macroscopic occupancy of the zero-momentum state. In the literature Σ_{11} is called the "normal" self-energy, while Σ_{12} and Σ_{21} are known as the "anomalous" self-energies (it can be shown that in general $\Sigma_{12} = \Sigma_{21}$. (see for example [27] and [31]). A weakly interacting ($n_B a_{BB}^3 \ll 1$) Bose system at $T = 0$ can be described by the standard Bogoliubov theory in 3D. In this theory one has:

$$\Sigma_{11} = 2\Sigma_{12} = \frac{8\pi a_{BB} n_0}{m_B}. \tag{3.28}$$

In the 2D case one can show, instead, that the normal (Σ_{11}) and anomalous self-energies (Σ_{12}) (see [12] and [33])

$$\Sigma_{11} = 2\Sigma_{12} = -\frac{8\pi n_0}{m_B \log(n_B a_{BB}^2)} \tag{3.29}$$

So in our framework the bosonic normal and anomalous self-energies take

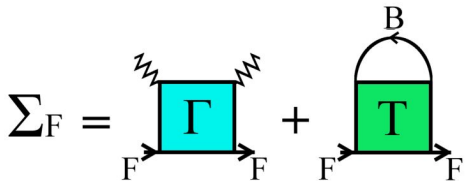

Figure 3.3: *Diagrams for the self-energy Σ_F:Diagrams for the self-energy Σ_{BF}: full lines correspond to the bare fermionic (F) and to the bare boson (B) Green's functions; the wavy lines are the condensate fraction $\sqrt{n_0}$.* Figure reproduced from Ref. [5].

the form:

$$\Sigma_{11}(\mathbf{k},\omega) \equiv \Sigma_B(\mathbf{k},\omega) = -\frac{8\pi n_0}{m_B \log(n_B a_{BB}^2)} + \int \frac{d^2P}{(2\pi)^2} \int \frac{d\Omega}{2\pi} T(\mathbf{P},\Omega) G_F^0(\mathbf{P}-\mathbf{k},\Omega-\omega) e^{i\Omega\eta} \quad \eta \to 0^+ \quad (3.30)$$

$$\Sigma_{12}(\mathbf{k},\omega) = \Sigma_{12} = -\frac{4\pi n_0}{m_B \log(n_B a_{BB}^2)}$$

3.3.2 Fermionic self-energy

The diagrams that we are going to consider for the fermionic self-energy $\Sigma_F(\mathbf{k},\omega)$ in our framework are drawn in Figure 3.3. The T-matrix can be closed in the diagram either with a boson propagator or with two condensate lines. The second choice, however, produces in general improper self-energy diagrams. For this reason the diagram closed with two condensate lines is constructed with just the Γ-matrix. The fermionic self-energy is then given by:

$$\Sigma_F(\mathbf{k},\omega) = n_0 \Gamma(\mathbf{k},\omega) - \int \frac{d^2P}{(2\pi)^2} \int \frac{d\Omega}{2\pi} T(\mathbf{P},\Omega) G_F^0(\mathbf{P}-\mathbf{k},\Omega-\omega) e^{i\Omega\eta} \quad (3.31)$$

where again the integral performed in Ω needs the convergence factor $e^{i\Omega\eta}$, with $\eta \to 0^+$.

3.4 Equations for the fermionic and bosonic densities

In general, from the self-energy, one can construct the corresponding interacting Green's function, from which one can derive several physical quantities. Here, we will be interested in the momentum distributions. The (interacting) fermionic Green's function is obtained from the Dyson's equation:

$$G_F(\mathbf{k},\omega) = \frac{1}{G_F^0(\mathbf{k},\omega)^{-1} - \Sigma_F(\mathbf{k},\omega)}. \tag{3.32}$$

The fermionic momentum distribution function $n_F(\mathbf{k})$ is in turn given by:

$$n_F(\mathbf{k}) = \int_{-\infty}^{+\infty} \frac{d\omega}{2\pi} G_F(\mathbf{k},\omega) e^{i\omega\eta} \quad \eta \to 0^+, \tag{3.33}$$

from which the fermion density n_F is obtained by an integration over momenta:

$$n_F = \int \frac{d^2k}{(2\pi)^2} n_F(\mathbf{k}) \tag{3.34}$$

Due to the presence of the condensate, the expression of the expression of the Dyson's equation is more complicated respect to the fermionic case. For the bosons, the presence of the anomalous self-energy Σ_{12} makes the Dyson's equation to acquire a matrix form. The solution of the Dysons's equation for the normal bosonic Green's function is then given by:

$$G_B(\mathbf{k},\omega) = \frac{i\omega + \xi_{\mathbf{k}}^B + \Sigma_B(-\mathbf{k},-\omega)}{[i\omega + \xi_{\mathbf{k}}^B + \Sigma_B(-\mathbf{k},-\omega)][i\omega - \xi_{\mathbf{k}}^B - \Sigma_B(\mathbf{k},\omega)] + \Sigma_{12}^2} \tag{3.35}$$

The normal bosonic Green's function $G_B(\mathbf{k},\omega)$,when integrated over the frequency ω, yields the momentum distribution of non-condensed bosons ($\mathbf{k} \neq 0$):

$$n_B(\mathbf{k}) = -\int_{-\infty}^{+\infty} \frac{d\omega}{2\pi} G_B(\mathbf{k},\omega) e^{i\omega\eta} \quad \eta \to 0^+. \tag{3.36}$$

By integrating over the two-dimensional momentum $\mathbf{k}$, we then get the density n'_B of bosons out of the condensate:

$$n'_B = \int \frac{d^2k}{(2\pi)^2} n_B(\mathbf{k}). \tag{3.37}$$

The total density of bosons is thus given by the sum between n'_B and the condensate density n_0:

$$n_B = n_0 + \int \frac{d^2k}{(2\pi)^2} n_B(\mathbf{k}) \tag{3.38}$$

The above equations for the boson and fermion densities are complemented by the Hugenholtz-Pines equation which, in the condensed phase, connects the chemical potential to the normal and anomalous self-energies at vanishing momentum and frequency (see Ref. [34]):

$$\mu_B = \Sigma_B(\mathbf{k} = 0, \omega = 0) - \Sigma_{12}(\mathbf{k} = 0, \omega = 0). \tag{3.39}$$

The three equations (3.34),(3.38), and (3.39) allow one to determine the values of μ_F, μ_B, and n_0 for given densities and coupling strengths.

Pole of the fermionic dressed Green's function and Fermi momentum k_{F1}

It is useful to introduce the equation for the pole of the retarded fermionic Green's function $G_F^R(\mathbf{k}, \omega)$, which is obtained by analytic continuation of G to the real frequency axis. The pole is defined by the equation

$$\Re e\, G_F^R(\mathbf{k}, \omega(k))^{-1} = 0 \tag{3.40}$$

when:

$$\Im m\, G_F^R(\mathbf{k}, \omega(k))^{-1} = 0 \tag{3.41}$$

As we did for the Fermi step momentum of T^R, we define k_{F1} the values of k for which the dispersions of such poles cross zero. At the momenta k_{F1}, the fermionic momentum distribution function $n_F(\mathbf{k})$ will have a jump. For this reason finding the momentum k_{F1} is essential to optimize the integration of $n_F(\mathbf{k})$ over momenta to calculate the density. Note that since zero frequency is at the intersection between the imaginary and real axis, the determination of of momentum k_{F1} does not require to perform the analytic continuation. The momentum k_{F1} can thus be obtained by solving the equation:

$$\Re e\, G_F(k_{F1}, 0)^{-1} = 0. \tag{3.42}$$

Chapter 4

Numerical implementation of the theoretical formalism

The main purpose of the program is to solve the three fundamental equations:

$$n_B = n'_B + n_0 = n_0 + \int \frac{d^2k}{(2\pi)^2} n_B(\boldsymbol{k}) \tag{4.1}$$

$$n_F = \int \frac{d^2k}{(2\pi)^2} n_F(\boldsymbol{k}) \tag{4.2}$$

$$\mu_B = \Sigma_B(\boldsymbol{k} = 0, \omega = 0) - \Sigma_{12} \tag{4.3}$$

From equations (4.1),(4.2) *and* (4.3)*, the program finds the values of the chemical potentials μ_B, μ_F and the density population of the condensate n_0, for given boson concentration $x = n_B/n_F$, fermion density n_F, BF-pairing coupling $g = -\log(k_F a_{BF})$, BB repulsion a_{BB} and mass ratio m_B/m_F. We addressed the solution of these three fundamental equations by implementing a numerical code written in Fortran 90 language.*

4.1 General structure of the program

Units

All the equations presented above are inserted in the numerical program in a dimensionless form. To this end, a natural momentum scale is provided

by the Fermi momentum k_F of the non-interacting system, which in 2D is defined by inverting the equation

$$n_F = \int_0^{k_F} \frac{d^2k}{(2\pi)^2} = \frac{k_F^2}{4\pi}, \tag{4.4}$$

yielding $k_F = (4\pi n_F)^{1/2}$. All momenta are then measured in units of of the Fermi momentum k_F, all lengths in units of $(k_F)^{-1}$ and all densities in units of the value $k_F^2/4\pi = n_F$. In this way the convergence for the equations of the densities are reached when $\tilde{n}_F = n_F 4\pi/k_F^2 = 1$ and $\tilde{n}_B = n_B 4\pi/k_F^2 = x$, where $x = n_B/n_F$ is the concentration of bosons with respect to the fermion density. Masses are measured in terms of the fermionic mass m_F, while energies and frequencies are measured in terms of the Fermi energy $E_F = k_F^2/2m_F$. The T-matrices Γ, Γ^{SC}, and T are measured in units of $(m_F)^{-1}$.

How to perform integrations in the program

All integrals are evaluated with the Gauss-Legendre method, with the *Gauleg* subroutine, provided by Ref. [35]. Given an interval of integration, the subroutine takes as input the two extremes and two arrays of the same number N of elements. The subroutine divides the full interval into N sub-intervals, and evaluates the vectors of points and weights, according to the Gaussian quadrature procedure (for more information about this algorithm one can see Chapter 4 of Ref. [36]).

Root-finding subroutine: the SR1 algorithm

The program starts with initial trial values for μ_B, μ_F and n_0. At each step for the values of the chemical potentials and the condensate population, the program evaluates the self-energies, the dressed Green's functions and finally the equations (4.1),(4.2) and (4.3).

To find the solutions of the three fundamental equations we combine the bisection method with a two dimensional SR1 algorithm. The SR1 algorithm represents a generalization of the secant method for a multidimensional problem (see for example [37]).

Specifically, for given values of (μ_F, n_0), Eq. (4.3) is solved for μ_B with the bisection method (using the function *rtbis* from references [36] and [35]). In this way, equations (4.1) and (4.2) become functions of (μ_F and n_0) only, and are solved using the SR1 algorithm. The reason for the different treatment of Eq. (4.3) with respect to the remaining two equations is that Eq. (4.3) is much faster to be evaluated. Computationally, it is thus much more convenient to treat it separately.

When the SR1-subroutine starts, the trial values μ_F and n_0 determine μ_B through equation (4.3). Then iterations start and the program uses μ_B, μ_F and n_0 to evaluate the trial densities n_B and n_F. Such trial densities, after multiplication by the Hessian matrix, update the values of μ_F and n_0. The procedure restarts as above: $(\mu_F, n_0) \rightarrow \mu_B \rightarrow n_B, n_F$. At each step, the differences between the new values of the calculated densities $(n_B^{\rm new}, n_F^{\rm new})$ and the old ones $(n_B^{\rm old}, n_F^{\rm old})$, as well as the differences between the new values of the condensate fraction and fermionic chemical potentials $(n_0^{\rm new}, \mu_F^{\rm new})$ and the old ones $(n_0^{\rm old}, \mu_F^{\rm old})$, are used to determine the updating of the (approximate) Hessian matrix. Whenever the values of μ_F,n_0 and the Hessian matrix are updated, a new iteration of the SR1 method begins.

When the two density equations (4.1) and (4.2) are satisfied within a chosen precision, the cycle terminates.

4.2 How to deal with ill-convergent quantities

Some of the integrals over frequency involved in the calculation are particularly delicate to be evaluated numerically because they converge only because of the convergence factor which appear in their definition. The idea to deal numerically with these integrals is to rewrite them by adding and subtracting a contribution with the same high-frequency behavior. In this way, the difference between the original integral and the new contribution is now absolutely convergent, and can be integrated numerically, while the integral of the added contribution with the convergence factor is calculated analytically (provided of course the added contribution is chosen carefully).

4.2.1 Calculation of Δ^2_∞

By looking at the equation (3.16) , we notice that $T \propto (\log \Omega)^{-1}$ at large Ω, and so the quantity Δ^2_∞ :

$$\Delta^2_\infty = \int \frac{d^2P}{(2\pi)^2} \int \frac{d\Omega}{2\pi} T(\mathbf{P},\Omega) e^{i\Omega\eta} \quad \eta \to 0^+ \tag{4.5}$$

converges only because of the convergence factor $e^{i\Omega\eta}$. It is thus convenient to add and subtract the strong-coupling limit of the Γ-matrix $\Gamma^{SC}(\mathbf{P},\Omega)$ and write

$$\begin{aligned} &\int_{-\infty}^{+\infty} \frac{d\Omega}{2\pi} T(\mathbf{P},\Omega) e^{i\Omega\eta} \\ = &\int_{-\infty}^{+\infty} \frac{d\Omega}{2\pi} (T(\mathbf{P},\Omega) - \Gamma^{SC}(\mathbf{P},\Omega)) + \int_{-\infty}^{+\infty} \frac{d\Omega}{2\pi} \Gamma^{SC}(\mathbf{P},\Omega) e^{i\Omega.\eta} \end{aligned} \tag{4.6}$$

The term $T(\mathbf{P},\Omega) - \Gamma^{SC}(\mathbf{P},\Omega) \propto 1/(\Omega \log^2 \Omega)$ at large frequency: for this reason the convergence factor is no longer necessary and the first integral of (4.6) can now be evaluated numerically. By looking at the definition of $T(\mathbf{P},\Omega)$ and $\Gamma^{SC}(\mathbf{P},\Omega)$ (equations (3.8) and (3.16)), we can take advantage of the fact that $T(\mathbf{P},\Omega)^* = T(\mathbf{P},-\Omega)$, $\Gamma^{SC}(\mathbf{P},\Omega)^* = \Gamma^{SC}(\mathbf{P},-\Omega)$. In this way we can integrate only over positive frequencies and take two times the real part of the integral:

$$\int_{-\infty}^{+\infty} \frac{d\Omega}{2\pi} (T(\mathbf{P},\Omega) - \Gamma^{SC}(\mathbf{P},\Omega)) = 2\Re e \left[\int_0^{+\infty} \frac{d\Omega}{2\pi} (T(\mathbf{P},\Omega) - \Gamma^{SC}(\mathbf{P},\Omega)) \right] \tag{4.7}$$

Finally we divide the range of integration of Ω into two ranges: $[0,\Omega_c]$ and $[\Omega_c,+\infty]$:

$$\begin{aligned} &\int_0^{+\infty} \frac{d\Omega}{2\pi} [T(\mathbf{P},\Omega) - \Gamma^{SC}(\mathbf{P},\Omega)] = \\ &\int_0^{\Omega_c} \frac{d\Omega}{2\pi} [T(\mathbf{P},\Omega) - \Gamma^{SC}(\mathbf{P},\Omega)] + \int_{\Omega_c}^{+\infty} \frac{d\Omega}{2\pi} [T(\mathbf{P},\Omega) - \Gamma^{SC}(\mathbf{P},\Omega)] \end{aligned} \tag{4.8}$$

The first integral on the r.h.s of equation (4.8) can now be integrated numerically.

By choosing the cutoff Ω_c sufficiently large (in our numerical program is fixed at the value $\Omega_c = 10^7$), we can use the asymptotic expressions for

the integrand of the second term on the r.h.s. of equation (4.8). In fact for $\Omega \to \infty$, we can consider $n_0 G_F^0 \approx n_0/(i\Omega)$ and:

$$\Gamma^{SC}(\mathbf{P}, \Omega \to \infty) \approx -\frac{2\pi}{m_r} \frac{1}{\log(\frac{-i\Omega}{\epsilon_0})} \tag{4.9}$$

Moreover, for $\Omega \to \infty$, we can express $I_F(\mathbf{P}, \Omega)$ through the asymptotic expression (3.14). In this way, for large Ω we can write the integrand of the second term in equation (4.8) as:

$$\begin{aligned} &T(\mathbf{P}, \Omega \to \infty) - \Gamma^{SC}(\mathbf{P}, \Omega \to \infty) = \\ &= \frac{1}{\Gamma(\mathbf{P}, \Omega \to \infty)^{-1} - n_0 G_F^0(\mathbf{P}, \Omega \to \infty)} - \Gamma^{SC}(\mathbf{P}, \Omega \to \infty) \\ &\approx \frac{\Gamma^{SC}}{1 + \frac{1}{i\Omega}(n_{\mu_F} - n_0)\Gamma^{SC}} - \Gamma^{SC} \approx \Gamma^{SC}\left(1 - \frac{1}{i\Omega}(n_{\mu_F} - n_0)\Gamma^{SC}\right) - \Gamma^{SC} \end{aligned} \tag{4.10}$$

$$\implies T - \Gamma^{SC} \approx \frac{(n_0 - n_{\mu_F})}{i\Omega}(\Gamma^{SC})^2 \qquad \Omega \to \infty \tag{4.11}$$

Then, the behaviour of the integrand at large Ω is approximated as:

$$T(\mathbf{P}, \Omega) - \Gamma^{SC}(\mathbf{P}, \Omega) \approx \left(\frac{2\pi}{m_r}\right)^2 \frac{n_0 - n_{u_F}}{i\Omega \log^2 \frac{-i\Omega}{\epsilon_0}} \quad \Omega \to \infty \tag{4.12}$$

The integral of the above asymptotic expression from the large cut-off Ω_c to infinity gives:

$$\int_{\Omega_c}^{+\infty} \frac{d\Omega}{2\pi}(T(\mathbf{P}, \Omega) - \Gamma^{SC}(\mathbf{P}, \Omega)) = (n_0 - n_{\mu_F})\left(\frac{2\pi}{m_r}\right)^2 \frac{1}{2\pi} \frac{\frac{\pi}{2} - i \log \frac{\Omega_c}{\epsilon_0}}{(\frac{\pi}{2})^2 + \log^2 \frac{\Omega_c}{\epsilon_0}} \tag{4.13}$$

The second integral in equation (4.6) can instead be solved analytically by a contour integration in the complex plane after the analytic extension $i\Omega \to z$. By looking at the definition (3.8), one can see that $\Gamma^{SC}(\mathbf{P}, z)$ has a pole for $\Re ez = \xi_{\mathbf{P}}^{CF} = \frac{P^2}{2M} - \mu_{CF}$ and a branch cut for $\Re ez > z_c = \frac{P^2}{2M} - 2\mu$, such that

$$\begin{aligned} &\int_{-\infty}^{+\infty} \frac{d\Omega}{2\pi} \Gamma^{SC}(\mathbf{P}, \Omega) e^{i\Omega\eta} \\ &\qquad = \frac{2\pi}{m_r}\left[\epsilon_0 \Theta(-\xi_{\mathbf{P}}^{CF}) + \Theta(-z_c) \int_{z_c}^{0} \frac{dx}{\log^2(\frac{x - z_c}{\epsilon_0}) + \pi^2}\right], \end{aligned} \tag{4.14}$$

where the integral over x can be performed numerically through the *Gauleg* subroutine. In this way we have evaluated all pieces of the full integral (4.6). The subsequent integration over $\mathbf{P}$ of equations (4.7) and (4.14) is performed in polar coordinates. The integration over the angle is trivial and gives a factor 2π (there is no dependence on the angle), while the integration over P is performed numerically with a *Gauleg*-integration in the range $[0, P_{T1}]$, sampled with 10 points.

4.2.2 Calculation of the self-energies

Let us consider first the bosonic self energy:

$$\Sigma_{BF}(\mathbf{k},\omega) = \int \frac{d^2P}{(2\pi)^2} \int \frac{d\Omega}{2\pi} T(\mathbf{P},\Omega) G_F^0(\mathbf{P}-\mathbf{k},\Omega-\omega) e^{i\Omega\eta} \qquad \eta \to 0^+ \quad (4.15)$$

We sum and subtract function with the same asymptotic behaviour that can be analytically integrated in the complex plane. An ideal term is represented by $\Gamma^{SC}(\mathbf{P},\Omega) G_F^{00}(\mathbf{P}-\mathbf{k},\Omega-\omega)$, where G_F^{00} is a bare fermionic Green's function with $\mu_F^0 = 0^-$, in order to avoid introducing additional poles.

$$\begin{aligned}\Sigma_{BF}(\mathbf{k},\omega) = \int \frac{d^2P}{(2\pi)^2} \int_{-\infty}^{+\infty} \frac{d\Omega}{2\pi} [T(\mathbf{P},\Omega) G_F^0(\mathbf{P}-\mathbf{k},\Omega-\omega) \\ -\Gamma^{SC}(\mathbf{P},\Omega) G_F^{00}(\mathbf{P}-\mathbf{k},\Omega-\omega)] \qquad (4.16) \\ + \int \frac{d^2P}{(2\pi)^2} \int_{-\infty}^{+\infty} \frac{d\Omega}{2\pi} \Gamma^{SC}(\mathbf{P},\Omega) G_F^{00}(\mathbf{P}-\mathbf{k},\Omega-\omega) e^{i\Omega\eta}\end{aligned}$$

where now the first integral converges because the large-frequency behaviour of the integrand is $\propto 1/\Omega^2 \log\Omega$. The second integral of equation (4.16) is evaluated again by a contour integration in the complex plane. The function $\Gamma^{SC}(\mathbf{P},z)$ has a pole for $\Re ez = \xi_{\mathbf{P}}^{CF} = \frac{P^2}{2M} - \mu_{CF}$ and a branch cut for $\Re ez > z_c = \frac{P^2}{2M} - 2\mu$, while G_F^{00} has no singularities in the region enclosed by the contour, since $\mu_F^0 < 0$,. We obtain from this integration:

$$\begin{aligned}&\int_{-\infty}^{+\infty} \frac{d\Omega}{2\pi} \Gamma^{SC}(\mathbf{P},\Omega) G_F^{00}(\mathbf{P}-\mathbf{k},\Omega-\omega) e^{i\Omega\eta} = \\ &-\frac{2\pi}{m_r} \left\{ \frac{-\epsilon_0 \Theta(-\xi_{\mathbf{P}}^{CF})}{\xi_{\mathbf{P}}^{CF} - i\omega - \xi_{\mathbf{P}-\mathbf{k}}^{F0}} - \Theta(-z_c) \int_{z_c}^{0} dx \frac{1}{\log\frac{x-z_c}{\epsilon_0} + \pi^2} \frac{1}{x - i\omega - \xi_{\mathbf{P}-\mathbf{k}}^{F0}} \right\} \qquad (4.17)\end{aligned}$$

where we have defined $\xi^{F0}_{\mathbf{k}} = \frac{\mathbf{k}^2}{2m_F} - \mu^0_F$.

When performing the subsequent integral over $\mathbf{P}$ in polar coordinates, we now have terms that depend on the polar angle θ, specifically on $\cos\theta$. The integral over θ can be performed by using the identity (3.10), yielding:

$$\int_0^{2\pi} \frac{d\theta}{2\pi} \int_{-\infty}^{+\infty} \frac{d\Omega}{2\pi} \Gamma^{SC}(\mathbf{P},\Omega) G^{00}_F(\mathbf{P}-\mathbf{k},\Omega-\omega) e^{i\Omega\eta} =$$

$$= \frac{2\pi}{m_r} \Bigg[\frac{\epsilon_0 \Theta(-\xi^{CF}_{\mathbf{P}}) \mathrm{sgn}\Big(\xi^{CF}_{\mathbf{P}} - \frac{P^2+k^2}{2m_F} + \mu^0_F\Big)}{\sqrt{(\xi^{CF}_{\mathbf{P}} - i\omega - \frac{P^2+k^2}{2m_F} + \mu^0_F)^2 - (\frac{Pk}{m_F})^2}}$$

$$+\Theta(-z_c) \int_{z_c}^0 dx \frac{1}{\log^2(\frac{x-z_c}{\epsilon_0}) + \pi^2} \frac{\mathrm{sgn}\Big(x - \frac{P^2+k^2}{2m_F} + \mu^0_F\Big)}{\sqrt{(x - i\omega - \frac{P^2+k^2}{2m_F} + \mu^0_F)^2 - (\frac{Pk}{m_F})^2}} \Bigg], \tag{4.18}$$

where again the integral over x can be solved numerically with no difficulties.

Let us consider now the first integral in (4.16). We divide the integral over Ω in three ranges, i.e. $[-\infty,-\Omega_c]$,$[-\Omega_c,\Omega_c]$ and $[\Omega_c,\infty]$, where Ω_c is a large cutoff fixed at the value $\Omega_c = 50000$ in the numerical program.

We start by considering the interval $[-\Omega_c,\Omega_c]$. We have:

$$\int_0^{2\pi} \frac{d\theta}{2\pi} \int_{-\Omega_c}^{+\Omega_c} \frac{d\Omega}{2\pi} [T(\mathbf{P},\Omega) G^0_F(\mathbf{P}-\mathbf{k},\Omega-\omega) - \Gamma^{SC}(\mathbf{P},\Omega) G^{00}_F(\mathbf{P}-\mathbf{k},\Omega-\omega)] =$$

$$\int_{-\Omega_c}^{\Omega_c} \frac{d\Omega}{2\pi} T(\mathbf{P},\Omega) \frac{\mathrm{sgn}\Big(-\frac{P^2+k^2}{2m_F} + \mu_F\Big)}{\sqrt{(i(\Omega-\omega) - \frac{P^2+k^2}{2m_F} + \mu_F)^2 - (\frac{Pk}{m_F})^2}}$$

$$- \int_{-\Omega_c}^{\Omega_c} \frac{d\Omega}{2\pi} \Gamma^{SC}(\mathbf{P},\Omega) \frac{\mathrm{sgn}\Big(-\frac{P^2+k^2}{2m_F} + \mu^0_F\Big)}{\sqrt{(i(\Omega-\omega) - \frac{P^2+k^2}{2m_F} + \mu^0_F)^2 - (\frac{Pk}{m_F})^2}} \tag{4.19}$$

We now need to evaluate the integrals in the large Ω ranges $[-\infty,-\Omega_c]$ and $[\Omega_c,\infty]$ where we can use a large-Ω expansion of the integrand. In

addition, we note that for large Ω:

$$\left(\int_{-\infty}^{-\Omega_c} + \int_{\Omega_c}^{\infty}\right)\frac{d\Omega}{2\pi}[...] = 2\Re e\int_{\Omega_c}^{\infty}\frac{d\Omega}{2\pi}[...]. \tag{4.20}$$

In order to estimate the asymptotic expression for the integrand of the first term on the r.h.s of equation (4.16), we add and subtract the term $\Gamma^{SC}(\mathbf{P},\Omega)G_F^0(\mathbf{P}-\mathbf{k},\Omega-\omega)$:

$$\begin{aligned} T(\mathbf{P},\Omega)G_F^0(\mathbf{P}-\mathbf{k},\Omega-\omega) - \Gamma^{SC}(\mathbf{P},\Omega)G_F^{00}(\mathbf{P}-\mathbf{k},\Omega-\omega) \\ = (T(\mathbf{P},\Omega)-\Gamma^{SC}(\mathbf{P},\Omega))G_F^0(\mathbf{P}-\mathbf{k},\Omega-\omega) \\ +\Gamma^{SC}(\mathbf{P},\Omega)(G_F^0(\mathbf{P}-\mathbf{k},\Omega-\omega) - G_F^{00}(\mathbf{P}-\mathbf{k},\Omega-\omega)) \\ \approx \left(\frac{2\pi}{m_r}\right)^2 \frac{n_0-n_{u_F}}{i\Omega\log^2\frac{-i\Omega}{\epsilon_0}}\frac{1}{i\Omega} - \frac{2\pi}{m_r}\frac{1}{\log(\frac{-i\Omega}{\epsilon_0})}\frac{\mu_F^0-\mu_F}{(i\Omega)^2} \end{aligned} \tag{4.21}$$

for large Ω.

In addition:

$$G_F^0(\mathbf{P}-\mathbf{k},\Omega-\omega) - G_F^{00}(\mathbf{P}-\mathbf{k},\Omega-\omega) \simeq \frac{\mu_F^0-\mu_F}{(i\Omega)^2} \quad \Omega\to\infty \tag{4.22}$$

We thus have:

$$\begin{aligned} 2\Re e\int_0^{2\pi}\frac{d\theta}{2\pi}\int_{\Omega_c}^{\infty}\frac{d\Omega}{2\pi}(T(\mathbf{P},\Omega)G_F^0(\mathbf{P}-\mathbf{k},\Omega-\omega) - \Gamma^{sc}(\mathbf{P},\Omega)G_F^{00}(\mathbf{P}-\mathbf{k},\Omega-\omega)) \\ = 2\Re e\int_{\Omega_c}^{\infty}\frac{d\Omega}{2\pi}\left[\left(\frac{2\pi}{m_r}\right)^2\frac{n_0-n_{u_F}}{i\Omega\log^2\frac{-i\Omega}{\epsilon_0}}\frac{1}{i\Omega} - \frac{2\pi}{m_r}\frac{1}{\log(\frac{-i\Omega}{\epsilon_0})}\frac{\mu_F^0-\mu_F}{(i\Omega)^2}\right] \end{aligned} \tag{4.23}$$

Finally, after the change of variable $\Omega\to 1/x$, this integral is evaluated numerically in the range $[0,x_c]$ with *Gauleg*, with $x_c = 1/\Omega_c$.

The sum of the r.h.s. of equations (4.18),(4.19) and (4.23) has finally to be integrated over P.

Before discussing the final integral over P let us discuss the calculation of the fermionic self-energy (3.31). The procedure is similar to that for the bosonic self-energy Σ_{BF}. However, the bare bosonic Green's functions G_B^0 which appears in Eq. (3.31) does not contribute with a pole to the

corresponding contour integral, since $\mu_B \leq 0$ within G_B^0 (we recall that when $\mu_B > 0$ it is set $= 0$ in the G_B^0 which appears in the definition of Σ_F.

This makes the calculation easier, because it is sufficient to add and subtract $\Gamma^{SC}(\mathbf{P}, \Omega) G_B^0(\mathbf{P} - \mathbf{k}, \Omega - \omega)$ to the equation (3.31), with no need to introduce an auxiliary function G_B^{00}, as it was necessary for the calculation of Σ_{BF}). To evaluate the fermionic self-energy Σ_F we thus follow the same steps as for Σ_{BF}, with the substitutions $G_F^0 \to G_B^0$, $G_F^{00} \to G_B^0$, $\xi^{F0} \to \xi^B$ in (4.16) and (4.17). In particular the second term of (4.23) is not present.

The final integration over P is performed in a slightly different way for the two self-energies. As for Δ_∞^2, the integrands of both Σ_F and Σ_{BF} vanish for $P > P_{T1}$. For Σ_F, the bare Green's function G_B^0 does not introduce any further step. We thus use in this case a single *Gauleg*-integration in the range $[0, P_{T1}]$ (sampled with 10 points, typically).

The bosonic self-energy $\Sigma_B(\mathbf{k}, \omega)$ for $\mu_F > 0$ has instead two steps at $P = |k_{\mu_F} - k|$ and at $P = k_{\mu_F} + k$, due to the pole of $G_F^0(P - k, \Omega - \omega)$. We then order $|k_{\mu_F} - k|$,$k_{\mu_F} + k$ and P_{T1} and depending on this ordering we split the interval $[0, P_{T1}]$ in two or three further sub-intervals (or not split it at all, when $|k_{\mu_F} - k| > P_{T1}$). The sub-intervals are chosen to have the steps at their boundaries, in such a way that the integrals within each sub-interval can be calculated with *Gauleg*-integrations (with 10 points, typically).

Finally, when ω gets sufficiently large, it can be shown that, similarly to the 3D case [11], the two self-energies can be approximated by the following asymptotic expressions:

$$\Sigma_B(\mathbf{k}, \omega) \approx 2\Sigma_{12} + n_{\mu_F} T(\mathbf{k}, \omega) - \Delta_\infty^2 G_F^0(\mathbf{k}, -\omega) \tag{4.24}$$

$$\Sigma_F(\mathbf{k}, \omega) \approx n_0 \Gamma(\mathbf{k}, \omega) + \Delta_\infty^2 G_B^0(\mathbf{k}, -\omega). \tag{4.25}$$

In our numerical code, the asymptotic expressions (4.24) and (4.25) are used when $\omega / E_F \geq 100$.

4.3 Calculation of the densities

The momentum distribution functions $n_B(\mathbf{k})$ and $n_F(\mathbf{k})$ are obtained by integrating the dressed Green's functions over the frequency ω. Also in this

case the two integrands (which are proportional to $1/\omega$ at large frequencies) converge only thanks to the convergence factor. The numerical procedure to deal with these ill-convergent integrals is simpler than the cases considered previously. For the boson distribution, it is sufficient to add and subtract to the integrand of $n_B(\mathbf{k})$ the bare Bogoliubov Green's function $G_B^{0'}(\mathbf{k},\omega)$, defined by dropping altogether the BF self-energy in the equation (3.35) for the interacting bosonic Green function $G_B(\mathbf{k},\omega)$:

$$G_B^{0'}(\mathbf{k},\omega) = \frac{i\omega + \xi_{\mathbf{k}}^B + \Sigma_{12}}{(i\omega + \xi_{\mathbf{k}}^B + 2\Sigma_{12})(i\omega - \xi_{\mathbf{k}}^B - 2\Sigma_{12}) + \Sigma_{12}^2} \tag{4.26}$$

For the fermionic momentum distribution, instead, we simply add and subtract the bare fermionic Green's function $G_F^0(\mathbf{k},\omega)$ to the corresponding integrand. We thus write:

$$\begin{aligned} n_B(\mathbf{k}) &= -\int_{-\infty}^{+\infty} \frac{d\omega}{2\pi} G_B(\mathbf{k},\omega) e^{i\omega\eta} \\ &= -\int_{-\infty}^{+\infty} \frac{d\omega}{2\pi} [G_B(\mathbf{k},\omega) - G_B^{0'}(\mathbf{k},\omega)] - \int_{-\infty}^{+\infty} \frac{d\omega}{2\pi} G_B^{0'}(\mathbf{k},\omega) e^{i\omega\eta} \end{aligned} \tag{4.27}$$

$$\begin{aligned} n_F(\mathbf{k}) &= \int_{-\infty}^{+\infty} \frac{d\omega}{2\pi} G_F(\mathbf{k},\omega) e^{i\omega\eta} \\ &= \int_{-\infty}^{+\infty} \frac{d\omega}{2\pi} [G_F(\mathbf{k},\omega) - G_F^0(\mathbf{k},\omega)] + \int_{-\infty}^{+\infty} \frac{d\omega}{2\pi} G_F^0(\mathbf{k},\omega) e^{i\omega\eta} \end{aligned} \tag{4.28}$$

where the convergence factors have been dropped in the first terms on the right hand side because they are absolutely convergent.

The second terms on the r.h.s of equations (4.27) and (4.28) are easily evaluated by a contour integration. Due to the presence of the convergence factor $e^{i\omega\eta}, \eta \to 0^+$, the contour of these two integrals have to be closed in the upper complex plane. The function $G_B^{0'}(\mathbf{k},\omega)$ has two poles for $\omega_\pm = \pm i\sqrt{(\xi_{\mathbf{k}}^B)^2 + 3\Sigma_{12}^2 + 4\Sigma_{12}\xi_{\mathbf{k}}^B}$ and so only ω_+ contributes. For the fermionic case, the pole occurs at $\omega = -i\xi_{\mathbf{k}}^F$, and naturally it is in the upper complex

plane iff $\xi^F_{\mathbf{k}} < 0$. We thus obtain:

$$\begin{aligned}
\int_{-\infty}^{+\infty} \frac{d\omega}{2\pi} G^{0'}_B(\mathbf{k},\omega) e^{i\omega\eta} &= \frac{1}{2} \frac{\xi^B_{\mathbf{k}} + 2\Sigma_{12}}{\sqrt{(\xi^B_{\mathbf{k}})^2 + 3\Sigma^2_{12} + 4\Sigma_{12}\xi^B_{\mathbf{k}}}} - \frac{1}{2} \\
\int_{-\infty}^{+\infty} \frac{d\omega}{2\pi} G^{0}_F(\mathbf{k},\omega) e^{i\omega\eta} &= \Theta(-\xi^F_{\mathbf{k}})
\end{aligned} \tag{4.29}$$

The integrations over the frequency for the first terms on the r.h.s. of (4.27) and (4.28) are instead performed numerically. We use the property $G_{B/F}(\mathbf{k},-\omega) = G^*_{B/F}(\mathbf{k},\omega)$to restrict the range of integration to positive frequencies and write

$$\int_{-\infty}^{+\infty} \frac{d\omega}{2\pi} [G_F(\mathbf{k},\omega) - G^0_F(\mathbf{k},\omega)] = 2\Re e \int_0^{+\infty} \frac{d\omega}{2\pi} [G_F(\mathbf{k},\omega) - G^0_F(\mathbf{k},\omega)] \tag{4.30}$$

In practice, in the numerical calculations the integral over ω is evaluated in the range $[0, 50000E_F]$, with a negligible contributions from larger frequencies. This range is divided into five sub-ranges in order to take more points where needed: $[0, 0.002]$,$[0.002, 0.01]$,$[0.01, 0.3]$,$[0.3, 3]$,$[3, 1000]$, sampled with 100, 70, 50, 40 and 1000 points respectively.

We recall that for values of $\omega > 100E_F$ we use the asymptotic expressions (4.24) and (4.25) for the self-energies in the expression for the dressed Green's functions $G_F(\mathbf{k},\omega)$ and $G_B(\mathbf{k},\omega)$. The use of these equations in the large ω range is crucial to decrease the computational time, since in this case the internal integrations over P and Ω are performed analytically.

The final integration over the momentum $\mathbf{k}$ of $n_B(\mathbf{k})$ and $n_F(\mathbf{k})$ gives a factor 2π for the angular part, while the integral over k is separated in two ranges: $[0, k_c]$ and $[k_c, \infty]$. The cutoff k_c is chosen in such a way that in the large-momenta range $[k_c, \infty]$, one can use the asymptotic expressions:

$$n_B(k \gg k_F) = \frac{\Delta^2_\infty}{4\left(\frac{k^2}{4m_r} - \mu\right)^2} + \frac{\Sigma^2_{12}}{4\left(\frac{k^2}{2m_B} - \mu_B\right)^2} \tag{4.31}$$

$$n_F(k \gg k_F) = \frac{\Delta^2_\infty}{4\left(\frac{k^2}{4m_r} - \mu\right)^2}. \tag{4.32}$$

These asymptotic expressions were obtained in [11] for the 3D case, but they hold also in 2D. The corresponding integrals can thus be evaluated analytically. We have verified that the value $k_c = 4k_F$ for the cut-off is adequate for all couplings we have considered.

The numerical integration in the range $[0, k_c]$ requires a different treatment between the fermionic and bosonic cases. For fermions, the interval $[0, k_c]$ is split in the two sub-intervals $[0, k_{F_1}]$ and $[k_{F_1}, k_c]$ to account for the Fermi step at k_{F1}.

For the function $n_B(k)$ the integration is more complicated. The behaviour of the bosonic momentum function changes significantly in the full range of the BF coupling $g = -\log(k_F a_{BF})$, as it will be discussed in the next chapter. As a consequence, the sub-ranges of the interval $[0, k_c]$ are not kept fixed for all couplings, but they are modified in order to have more points around the peaks and main features of $n_B(k)$.

Chapter 5

Results for mixtures with majority of fermions

In this chapter we present the results obtained through a numerical solution of the T-matrix formalism in the case of mixtures with fermion density larger than or equal to the boson density, i.e. $n_F \geq n_B$. We focus on mass-balanced 2D BF mixtures and mostly with zero BB repulsion. All the fundamental quantities such as chemical potentials, condensate fraction and the momenta distribution functions are expressed as a function of the dimensionless BF coupling parameter $g = -\log(k_F a_{BF})$. Chemical potentials and the condensate fraction are compared in the weak-coupling limit to perturbative results found in [12],[13]. Finally, by using our numerical results, we estimate the size of the gap of the p-wave superfluid which should form according to the mechanism proposed in [10].

Relevance of BF mixtures with $n_B \leq n_F$

The results of the present work are restricted to BF mixtures for which the fermion density does not exceed the boson density. Even though our formalism can be applied also to mixtures with a majority of bosons, we have chosen to focus on the case $n_B \leq n_F$ for two reasons.

- We have seen that, very generally, pairing of bosons with fermions into

BF molecules competes with boson condensation. However, only when $n_B \leq n_F$, *all* bosons can pair with fermions to form BF molecules for sufficiently strong attraction. A complete suppression of the condensation fraction at $T = 0$ can thus be achieved only when $n_B \leq n_F$. Only in these mixtures it thus possible to have a quantum phase transition from a phase with a condensate to a Fermi-Fermi mixture phase, composed only by BF molecules and unpaired fermions, in the absence of a condensate.

- Mixtures with a majority of bosons are expected to be more severely affected by three-atom losses, since the dominant recombination process involves two bosons and a fermion, with a loss rate which thus scales with $n_B^2 n_F$. Recombination involving two fermions and a bosons are in fact hindered by the Pauli exclusion principle.

5.1 Condensate fraction

Here, we present the results for the condensate fraction n_0/n_B. We start our discussion by considering the weak coupling regime. In this regime, the condensate fraction should approach the perturbative result

$$\frac{n_0}{n_B} = 1 - \frac{1}{4g^2}\left(\frac{w+1}{w}\right)^2 \log(w+1) + \frac{1}{\log(n_B a_{BB}^2)} \tag{5.1}$$

where $w = m_B/m_F$ (in our case $w = 1$).

Eq. (5.1) represents a combination of the results obtained by Refs. [12] (describing the weak coupling limit for a system of interacting bosons in 2D) and [13] (describing the weak coupling limit of BF attraction in 2D).

Figure 5.1 thus reports our numerical results for the condensate fraction in the weak regime of the BF attraction, for the case of a mass-balanced mixture with a BB repulsion $\eta = -[\log(n_B a_{BB}^2)]^{-1} \approx 5 \times 10^{-3}$.

One can appreciate how the numerical results (red continuous line), for the two different concentrations $x = 0.175$ (panel (a)) and $x = 1.0$ (panel (b)), follow mostly equation (5.1) (dashed line) and tend to approach the

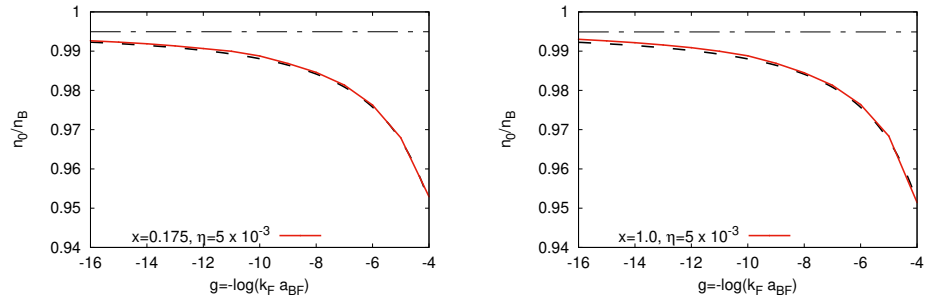

(a) (b)

Figure 5.1: *Condensate fraction in the weak BF coupling regime for two concentrations* $x = 0.175$ *(panel (a)) and* $x = 1.0$ *(panel (b)) and with a BB repulsion* $\eta = -[log(n_B a_{BB}^2)] = 5$ x 10^{-3}. *Dashed line: weak coupling limit of* n_0/n_B *given by equation* (5.1). *Dash-dotted line: asymptotic limit* $1 + [\log(n_B a_{BB}^2)]^{-1}$ *of the condensate fraction for* $g \to -\infty$.

asymptotic limit $1 + [\log(n_B a_{BB}^2)]^{-1}$ (dash-dotted line) for $g \to -\infty$. This limit is determined only by the boson repulsion.

Figure 5.2 reports instead our numerical results for the condensate fraction in the whole BF coupling range (in the case of mass-balanced mixture with zero BB repulsion) for three different concentrations $x = 0.175, 0.5$ and 1.0. Also in this case, all curves for n_0/n_B approach the weak coupling limit given by equation (5.1).

In particular the universal behaviour (described in Section for the 3D case) of the condensate fraction n_0/n_B is found also in the 2D case: the curves corresponding to different values of the concentration $x = n_B/n_F$ overlap each other, except for the ending part of the curves, when n_0/n_B is already quite small.

On the other hand, no critical coupling above which $n_0 = 0$ identically is found in the 2D case. This finding is different with respect to the 3D case. We believe however that this finding is due to a shortcoming of the T-matrix approximation in 2D. Specifically, in the polaronic limit $x \to 0$, the T-matrix is known to overestimate the repulsion between the molelcular state and the surrounding fermions (yielding a molecule-fermion repulsion

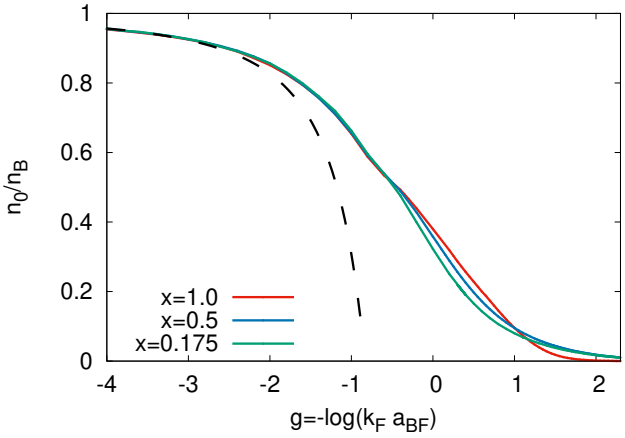

Figure 5.2: *Condensate fraction n_0/n_B as function of the dimensionless BF coupling parameter $g = -\log(k_F a_{BF})$, for three different concentrations $x = n_B/n_F = 0.175, 0.5, 1.0$ (with $m_B = m_F$ and zero BB repulsion). Dashed line: weak coupling limit of n_0/n_B given by equation* (5.1).

which is not vanishing in the molecular regime, see for example [38], [39]).

This suppresses the polaron-molecule transition. The same overestimate of the molecule-fermion repulsion (as well as of the molecule-molecule repulsion) suppresses the transition at finite x. Improving the approximation would require the inclusion of three-body correlations, as discussed in Ref. [40], a task which is however extremely difficult to implement outside the polaronic limit $x \to 0$.

Note however that the condensate fraction becomes negligible for $g = -\log(k_F a_{BF}) \gtrsim 2$ for all concentrations; for larger couplings the system can thus be considered in the molecular phase for all practical purposes.

5.2 Momentum distribution functions

In this Section we present the behaviour of the bosonic and fermionic distribution functions $n_B(k)$ and $n_F(k)$. We show their evolution in the full coupling regime that we have explored in our numerical simulations.

The behaviour of the bosonic momentum distribution function is partic-

ularly rich. The full evolution of the function $n_B(k)$ is shown in the panels from (a) to (e) of Figures 5.3, 5.4 and 5.5.

At weak coupling, $n_B(k)$ starts from a non-zero value at $k = 0$ and shows a peak at low momenta. By increasing the coupling, the height of the peak grows, until the coupling value $g \approx -1.80$ is reached. Starting from this regime of BF pairing, the peak at finite momentum disappears, and the whole function flattens by increasing the coupling parameter (with a redistribution of the occupancy from low momenta to high momenta). Beyond the a coupling $g \approx 0$, one observes a different behaviour of $n_B(k)$ for the concentrations $x = n_B/n_F = 0.175, 0.5$ with respect to the balanced-density case $x = 1$. Indeed, one can appreciate the appearance of a cusp in the curves of $n_B(k)$ corresponding to the two concentrations $x = 0.175, 0.5$. The cusp becomes more pronounced by increasing the coupling, suggesting a bi-modal distribution. We explain this behaviour as the superposition of two different contributions.

We attribute the shape of $n_B(k)$ at low momenta to condensed bosons. The second shape, at larger momenta, is instead attributed to the indirect Pauli exclusion effect, that we discussed previously for 3D BF mixtures. From Section 2.1, we know in particular that this peculiar effect occurs in 3D for Bose-Fermi mixtures with $x = n_B/n_F < 0.5$ in the molecular limit, yielding a range $[0, k_0]$ where $n_B(k)$ is identically zero, while $k_0 = 0$ for $x \geq 0.5$ (even though a peak might still occurs, except for $x = 1$). Consistently with this interpretation, we see that for $x = 1$ the curve for $n_B(k)$ follows a regular evolution with coupling, without showing any cusp.

In 2D, we see that the indirect Pauli exclusion effect is not limited to the molecular limit, but is anticipated to coupling values where the condensate fraction is still sizable, thus filling the region $[0, k_0]$ with the contribution from the condensed bosons. We believe that this finding is a clear indication of the presence of molecules even away from the extreme molecular limit, and of their coexistence with condensed bosons, reflecting the general expectation that in 2D pairing effects should be larger than in 3D.

The panels (f) of Figures 5.3, 5.4 and 5.5, show the evolution with coupling of the fermionic momentum distribution function $n_F(k)$ for the three

concentrations $x = 0.175, 0.5$ and 1.0. The expected behavior for a Fermi liquid, with a step pinned at k_F, holds up to $g \approx 0$ (see also the next Section). As expected, the occupation number for $k < k_{F1}$ is progressively reduced for increasing coupling, signalling that increasing BF-correlations push fermions into states above k_F, as necessary for the formation of BF molecules.

In order to emphasise the behaviour of $n_F(k)$ at large momenta, in the insets of Figures 5.3f, 5.4f and 5.5f, we report the ratio between $n_F(k)$ and the asymptotic result (4.32):

$$\phi(k) = \frac{\Delta_\infty^2}{4\left(\frac{k^2}{4m_r} - \mu\right)^2} \tag{5.2}$$

which holds for $k \gg k_F$. One can notice how the ratio $n_F(k)/\phi(k)$ tends quite rapidly to unity for all coupling and concentrations when k increases. This validates our choice to use the asymptotic expressions (4.31) and (4.32) for $k \geq k_F$ when integrating the momentum distribution functions.

As a final technical remark for this Section, we stress that the cusp feature in the curve of $n_B(k)$ complicates the optimal choice of the numerical grid for the integration of $n_B(k)$ over the momenta k (required to get the bosonic density). The optimal choice was the result of several trials, and needed a patient tuning when varying the interaction or concentration parameters.

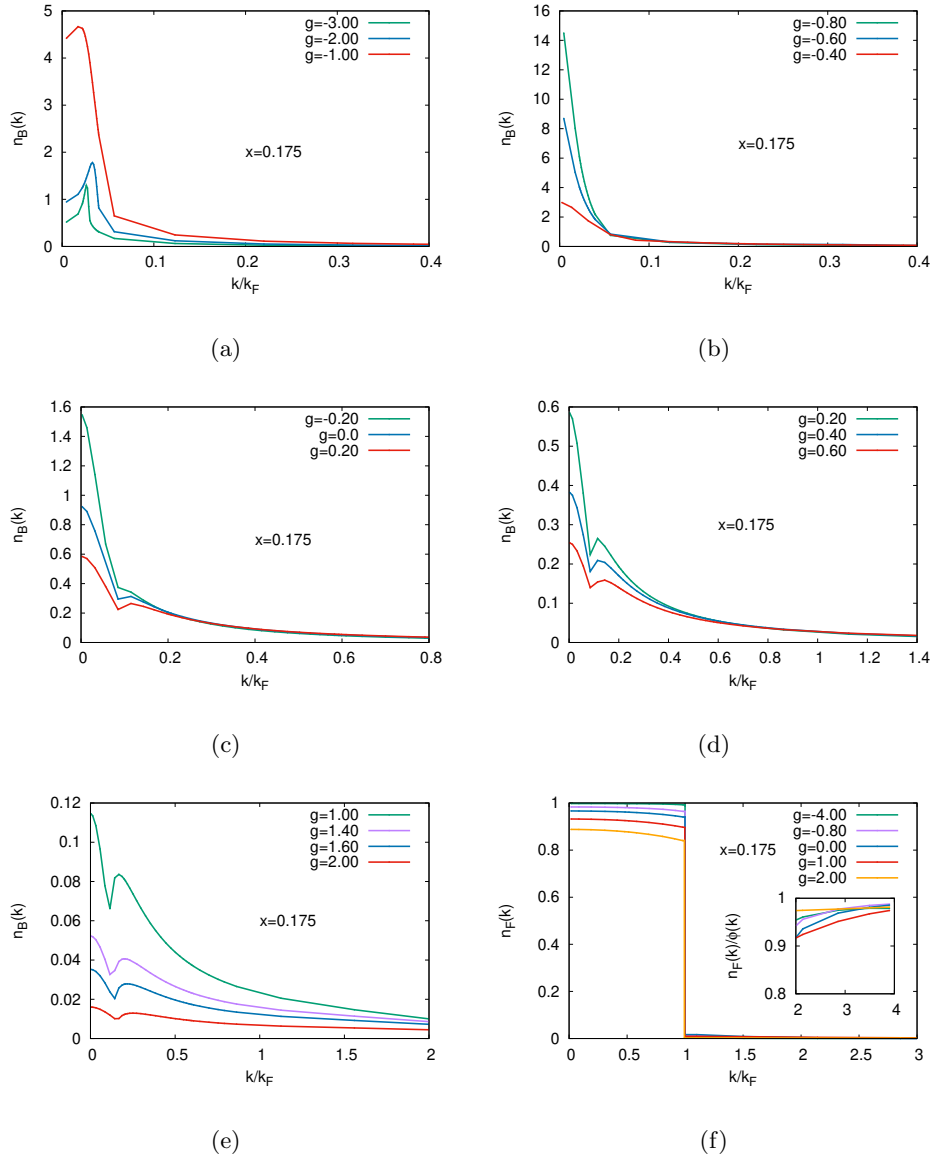

Figure 5.3: *Panels from (a) to (e): Evolution of the bosonic momentum distribution function* $n_B(k)$ *as function of the BF coupling parameter* $g = -\log(k_F a_{BF})$*, for a concentration of* $x = n_B/n_F = 0.175$*. Panel (f) :Evolution of the fermionic momentum distribution function* $n_B(k)$ *as function of the BF coupling parameter* $g = -\log(k_F a_{BF})$*. All figures are for equal fermion and boson masses and zero BB repulsion.*

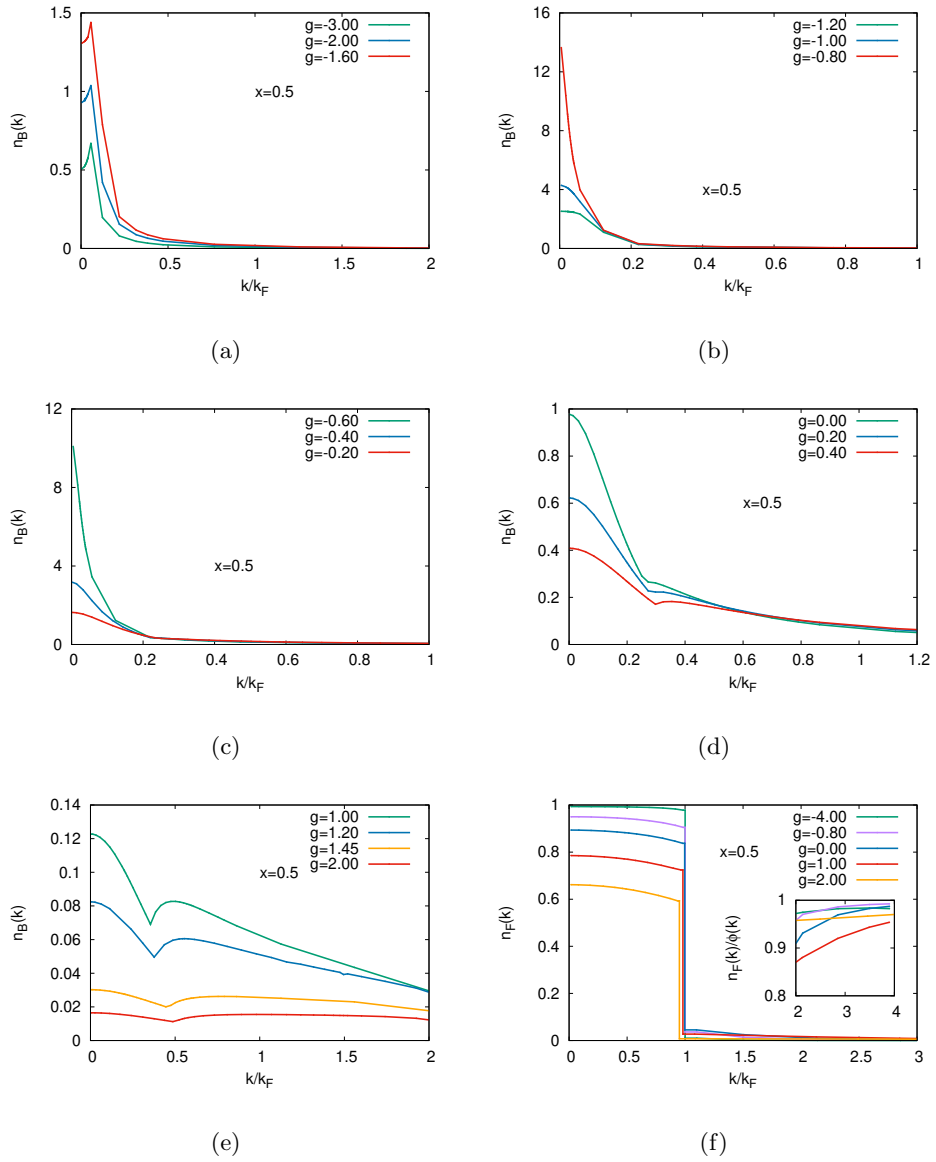

Figure 5.4: Panels from (a) to (e): *Evolution of the bosonic momentum distribution function* $n_B(k)$ *as function of the BF coupling parameter* $g = -\log(k_F a_{BF})$, *for a concentration of* $x = n_B/n_F = 0.5$. Panel (f) :*Evolution of the fermionic momentum distribution function* $n_F(k)$ *as function of the BF coupling parameter* $g = -\log(k_F a_{BF})$, *for a concentration of* $x = n_B/n_F = 0.5$. *All figures are for equal fermion and boson masses and zero BB repulsion.*

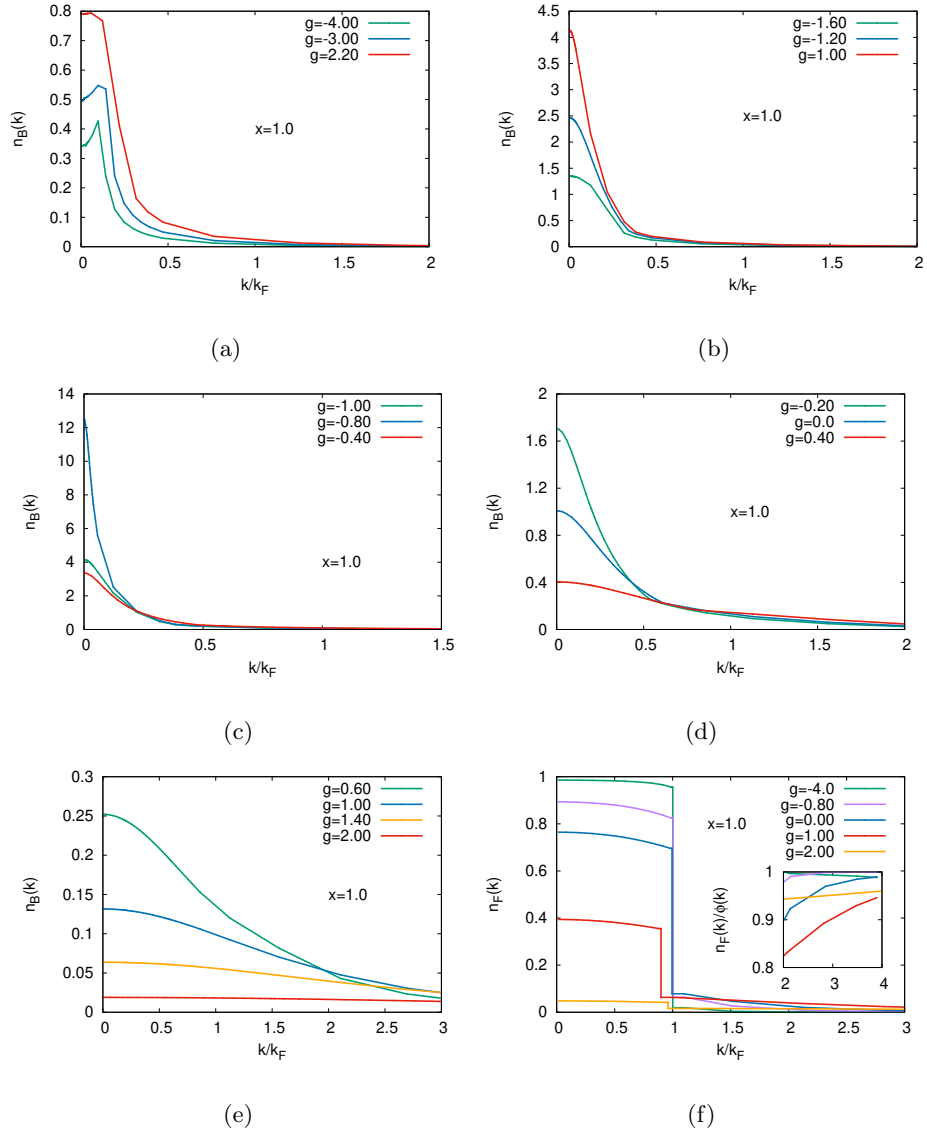

Figure 5.5: *Panels from (a) to (e): Evolution of the bosonic momentum distribution function $n_B(k)$ as function of the BF coupling parameter $g = -\log(k_F a_{BF})$, for the balanced density case $x = n_B/n_F = 1.0$. Panel (f) :Evolution of the fermionic momentum distribution function $n_F(k)$ as function of the BF coupling parameter $g = -\log(k_F a_{BF})$, for the balanced density case $x = n_B/n_F = 1.0$. All figures are for equal fermion and boson masses and zero BB repulsion.*

5.3 Results for the Fermi step momenta of G_F, T, and Γ

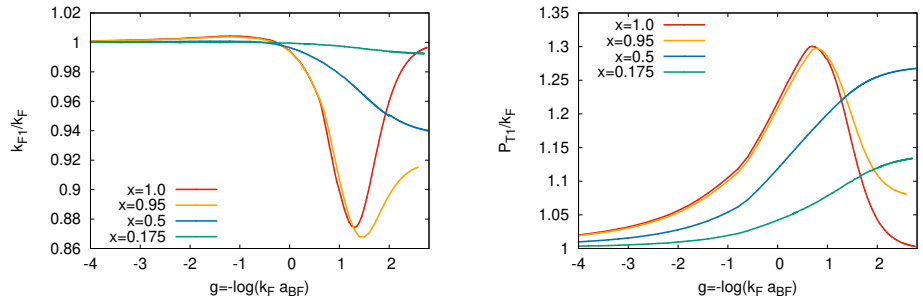

(a) (b)

Figure 5.6: *Momenta k_{F_1} (a) and P_{T_1} (b) vs. the BF coupling parameter $g = -\log(k_F a_{BF})$ for different bosonic concentrations x.*

In Sections 3.2 and 3.4 we introduced the momenta k_{F_1} and P_{T_1} at which $\int G_F(k,\omega)e^{i\omega 0^+}d\omega$ and $\int T(P,\Omega)e^{i\Omega 0^+}d\Omega$ present a Fermi step. Figure 5.7 presents the numerical results for k_{F_1} and P_{T_1} as functions of the dimensionless coupling $g = -\log(k_F a_{BF})$ and for four different concentrations $x = n_B/n_F = 0.175, 0.5, 0.95$ and 1.0.

Let us first consider the results for the momenta k_{F_1}, reported in panel (a) of Figure 5.7. From weak coupling to a value around $g \approx 0$, k_{F_1} remains about equal to k_F (with some small deviations for the two cases $x = 0.175$ and $x = 0.5$). In this regime of values of g, where BF correlations are not too strong, the jump of $n_F(k)$ is pinned at k_F, according to the Luttinger theorem. As a consequence, fermions behave as a Fermi liquid.

For positive values of $g = -\log(k_F a_{BF})$, k_{F_1} deviates significantly from k_F, signalling that BF correlations are now strong enough to create molecules and consequently produce some breakdown of Fermi liquid properties. Quite naturally, the deviations of k_{F_1} from the Fermi liquid value k_F are smaller at the lowest boson concentrations, since these deviations are produced by interaction with bosons.

At the highest concentrations $x = 0.95$ and $x = 1.0$, k_{F_1} displays a non-

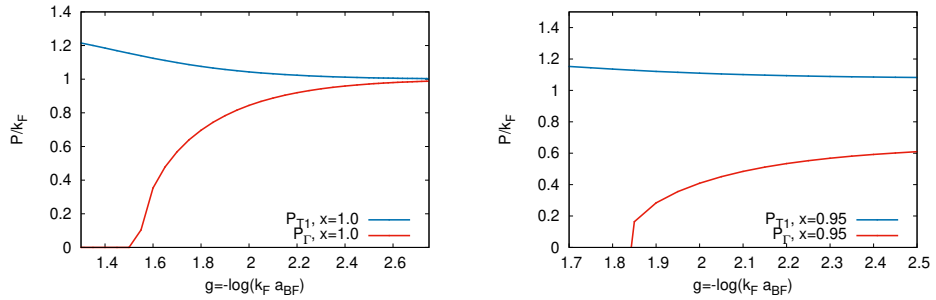

(a) (b)

Figure 5.7: *Momenta P_{T_1} and P_Γ vs. the BF coupling parameter $g = -\log(k_F a_{BF})$ for the bosonic concentrations $x = 1.0$ (a) and $x = 0.95$ (b)*

monotonic behavior, with a minimum for g slightly above one. We still do not have an explanation for this overall behavior of k_{F1}. We can just notice that the presence of such a minimum in the curve of k_{F1} seems somehow correlated with the presence of a maximum in the curve for the momentum P_{T1} (see Figure 5.7 (b)), even though the position of the these two features do not exactly coincide.

Interestingly, for these two cases of higher concentrations and for strong coupling, a Fermi step appears also in the function $\int \Gamma(P,\Omega)e^{i\Omega 0^+}d\Omega$. The corresponding momentum P_Γ is reported in panels (c) and (d) of Fig. 5.7, together with the momentum P_{T1}, for comparison. We see that for these two concentrations P_Γ appears above a critical coupling ($g \approx 1.55$, for $x = 1$, and $g \approx 1.80$, for $x = 0.95$), and progressively increases with the coupling. For the perfectly balanced case $x = 1$, both P_Γ and P_{T_1} reach the asymptotic value $P_\Gamma = P_{T_1} = 1$, while for $x = 0.95$, P_Γ and P_{T1} reach different asymptotic limits.

5.4 Results for the chemical potentials and Δ^2_∞

We pass now to discuss the results for the chemical potentials μ_B and μ_F. We focus first on the weak-coupling regime, where the bosonic and fermionic chemical potentials are expected to recover the perturbative results [13],

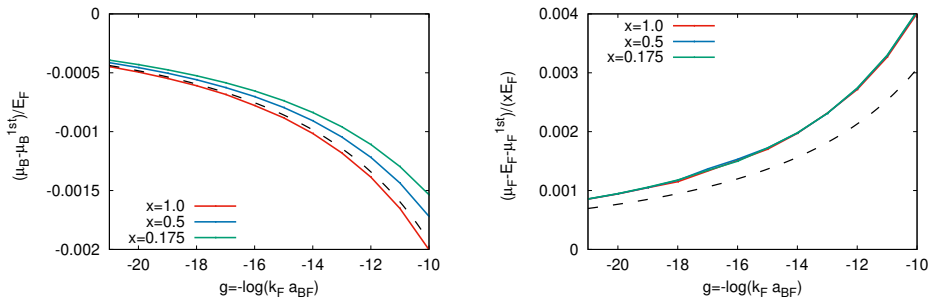

(a) (b)

Figure 5.8: *Bosonic and fermionic chemical potentials minus the leading terms* ($\propto g^0$ *and* $\propto g^{-1}$) *as function of the BF coupling* g. *In the case of fermions we also divide by the concentration* x. *Dash curve: second order correction* ($\propto g^{-2}$) *in Equations* (5.3) *and* (5.4).

.

referred to 2D BF mixtures in the mass-balanced case ($m = m_F = m_B$):

$$\mu_B = \frac{2\pi n_F}{mg}\left\{1 + \frac{1}{2g}\left[1 - \log 4\right]\right\} \tag{5.3}$$

$$\mu_F = E_F + \frac{2\pi n_B}{mg}\left\{1 + \frac{1}{2g}\left[2 - \log 4\right]\right\}. \tag{5.4}$$

The comparisons between the numerical results for μ_B and μ_F and equations (5.3) and (5.4) (for zero BB repulsion) are shown in Figure 5.8. In order to make such a comparison more stringent, we subtract the leading contributions: $\frac{\pi n_F}{m_r g}$ and $E_F + \frac{\pi n_B}{m_r g}$, for μ_B and μ_F, respectively. In the fermionic case we further divide the results by the concentration $x = n_B/n_F$. We see that both the bosonic and the fermionic chemical potentials approach the second order perturbative result, even though quite slowly. Interestingly, when divided by the boson concentration the curves for the fermionic chemical potentials collapse on top of each other even before reaching the perturbative expression (where this property holds, due to the analytic form of Eq. (5.4)).

The behaviour of the two chemical potentials away from the weak cou-

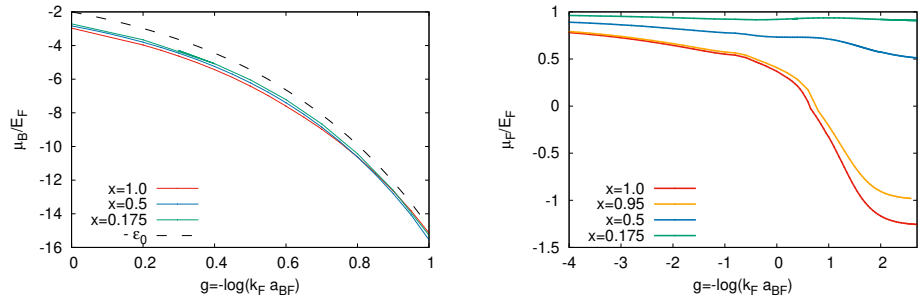

(a) (b)

Figure 5.9: *Panel (a): Bosonic chemical potential as a function of g for different concentrations. All curves approach minus the binding energy* $-\epsilon_0$ *(dashed lines). Panel (b): Fermionic chemical potential as a function of g for different concentrations.*

pling limit is reported in Figure 5.9. Specifically, panel (a) reports the bosonic chemical potential μ_B for intermediate couplings ($0 < g < 1$), in order to show how μ_B progressively approaches the expected asymptotic value $-\epsilon_0$, where $\epsilon_0 = 1/(2m_r a_{BF}^2)$ is the binding energy of the two-body bound state in vacuum. This is because, for strong coupling, if an extra boson is added to the mixture, it will immediately bound to a fermion (as long as $n_B \leq n_F$).

Figure 5.9b reports the fermionic chemical potential for different bosonic concentrations. The behaviour of μ_F differs substantially from what is found in the 3D case. As we have already discussed in Section 2.2, in 3D, μ_F does not show a monotonic behaviour: it first decreases because of the increasing attraction with bosons, it reaches a minimum, and then increases due to the Pauli repulsion between BF molecules. In 2D, we find that the fermionic chemical potential decreases monotonically. In particular for higher concentrations (so, for mixtures with comparable fermion and boson densities), μ_F can reach even negative values when the BF attraction is sufficiently strong. For all concentrations, μ_F seems to flatten to an asymptotic value when $g \gg 1$.

We expect such asymptotic value of μ_F to be determined by a balance

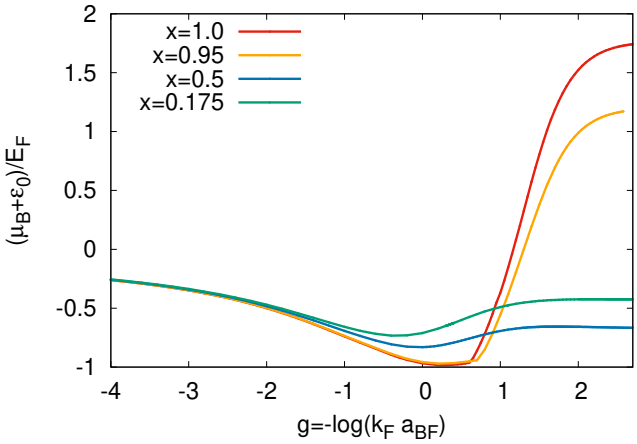

Figure 5.10: *Bosonic chemical potential plus the binding energy for concentrations* $x = 0.175, 0.5, 0.95, 1.0$ *as a function of the BF coupling* $g = -\log(k_F a_{BF})$.

between the Pauli repulsion among the unpaired fermions and the fermions bounded in the BF molecules, and the attraction with the bosons bounded in the molecules. In future work, it would be interesting to perform an expansion in the strong-coupling limit to obtain analytic expressions for this (and other) asymptotic values.

Figure 5.10 shows the function $\mu_B + \epsilon_0$ as a function of g for different boson concentrations. We have seen indeed that when g is large μ_B approaches $-\epsilon_0$. In terms of the dimensionless coupling g, one has $\epsilon_0/E_F = 2e^{2g}$, so that this scale becomes rapidly quite large. By plotting $\mu_B + \epsilon_0$, we are thus able to emphasize the sub-leading correction to the leading behavior in the strong-coupling limit. Similarly to the case of the fermionic chemical potential, also the function $\mu_B + \epsilon_0$ shows a saturation value for sufficient strong values of the BF coupling $g = -\log(k_F a_{BF})$. Like for the chemical potential μ_F, it would be interesting to derive analytic expressions also for $\mu_B + \epsilon_0$ in the molecular limit.

We conclude this Section by presenting our numerical results for the quantity Δ^2_∞. We recall that this quantity, apart from trivial constants, coincides with the so-called Tan's constant C, which rules the large mo-

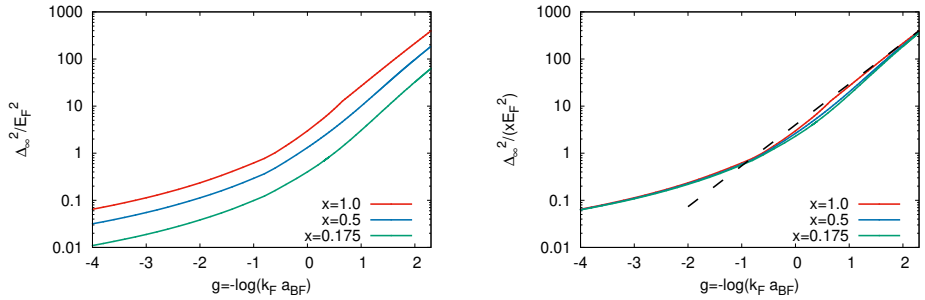

(a) (b)

Figure 5.11: Δ_∞^2 *as function of* $g = -\log(k_F a_{BF})$ *for different concentrations. In panel (b) we divide also for the concentration* $x = n_B/n_F$. *Dashed line: strong coupling limit given by* (5.5).

mentum behavior of the bosonic and fermionic momentum distributions. Specifically, for mixtures without BB repulsion one has at large momenta $n_B(k) = n_F(k) = C/k^4$, with $C = 4m_r^2\Delta_\infty^2$.

One can see in Figure 5.11 that Δ_∞^2 increases monotonically with the dimensionless BF coupling g. This is expected: we recall, indeed, that in the strong-coupling limit Δ_∞^2 is proportional to the density of composite fermions n_{CF}

$$\Delta_\infty^2 = \frac{\pi}{m_r^2 a_{BF}^2} n_{CF} = \frac{2\pi\epsilon_0}{m_r} n_{CF} \quad (g \to \infty) \tag{5.5}$$

where, for BF mixtures with majority of fermions, $n_{CF} = n_B$. Figure 5.11 (a) suggests that the curves of Δ_∞^2 vs coupling for different concentrations may differ by just an overall scale factor. By dividing Δ_∞^2 by the concentration x, we see indeed in panel(b) of Figure (5.11) that the curves corresponding to different concentrations overlap each other in almost the entire BF coupling range, indicating a universal behavior with respect to the concentration also for Δ_∞^2, besides the universal behavior of condensate fraction discussed above.

The dashed line in Figure 5.11b corresponds to the strong-coupling limit $\frac{2\pi\epsilon_0}{m_r}$ (which is obtained from (5.5) divided by n_B). A further check of the asymptotic limit of Δ_∞^2 is shown in Figure 5.12, for concentrations $x =$

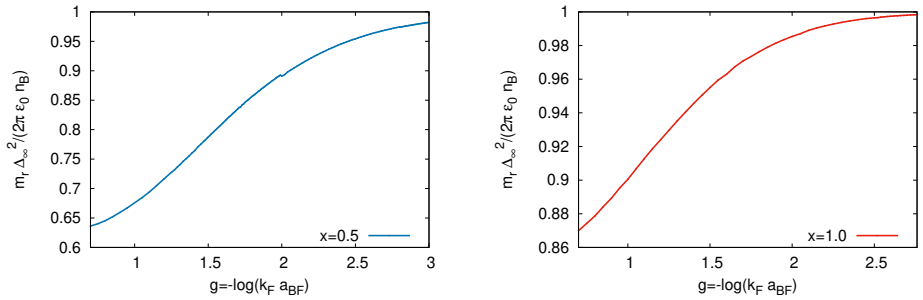

(a) (b)

Figure 5.12: Δ_∞^2 *divided by the convergence value given by equation* (5.5) *for positive values of BF coupling* g*. Figures are referred to concentration* $x = 0.5$ *(a) and* $x = 1.0$ *(b).*

$0.5, 1.0$, where the numerical results for Δ_∞^2 are divided by the asymptotic limit. For both concentrations, this ratio approaches one for strong BF coupling, as expected.

5.5 Estimation of the p-wave superfluid gap in the presence of a boson condensate

In Section 2.4, we described a proposal for creating a p_x+ip_y superfluid with 2D Bose-Fermi mixtures (with equal masses and densities). By combining BCS mean field for a p-wave superfluid, with few-body calculations, the p-wave superfluid gap Δ_{gap} should be given by [10]

$$\Delta_{gap} \approx \frac{k_F^m}{\xi(m_F+m_B)} \exp(2/k_F^{m2} S) \tag{5.6}$$

where k_F^m is the Fermi momentum associated to the BF molecules, ξ represents the effective range of the induced p-wave attraction and S is the p-wave scattering surface. By evaluating the energy spectrum of the FFBB system, Bazak and Petrov found the values $a_{FB}/2 < \xi < a_{FB}$ and $S \approx -3a_{FB}^2$.

However, the treatment of Ref. [10], ignored completely the presence of boson condensation. With our numerical simulations, we are able to take the boson condensation into due account. The presence of a condensate fraction will in fact compete with the formation of the molecules, thus reducing their number, and consequently the molecule Fermi momentum k_F^m.

In order to estimate k_F^m, we assume that all bosons with momentum $\mathbf{k} \neq 0$ are bounded in BF molecules. As a consequence, $(k_F^m)^2 \approx 4\pi(n_B - n_0)$. In this way, by using our numerical results for the condensate fraction (for $n_F = n_B$, $m_B = m_F$, in the absence of boson repulsion), we can calculate the p-wave superfluid gap Δ_{gap} as a function of the boson-fermion coupling g, by taking into account also the BEC. The resulting behaviour of the gap is shown in Figure 5.13 (a).

From this figure we see that the p-wave superfluid gap reaches a maximum value of $\Delta_{gap} \approx 0.27\ E_F$ at the value $g \approx -0.2$. This large value of the p-wave gap is quite promising for the experimental observability of the p-wave superfluid. We notice however that at this value of g the condensate fraction is still quite high (with a value of about 0.44, see also panel (b)). The presence of such large condensate fraction could in principle affect also the value of the induced p-wave interaction between the molecules.

In this respect, it could thus be more convenient to work at stronger

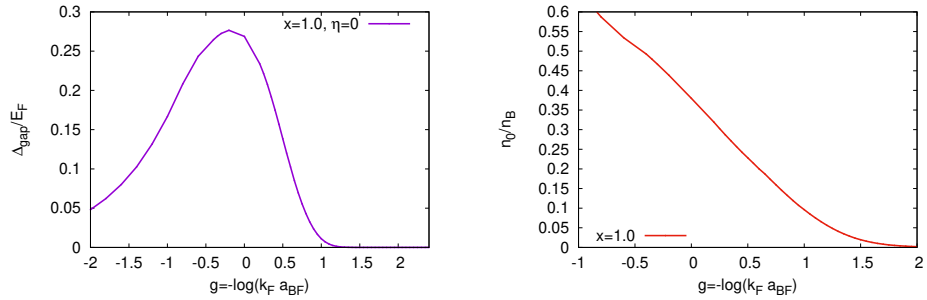

(a) (b)

Figure 5.13: *Panel (a): Width of the p-wave superfluid gap as function of the BF coupling g, for concentration $x = 1$ and with zero BB repulsion. Panel (b): Condensate fraction as function of $g = -\log(k_F a_{BF})$ for for concentration $x = 1$ and with zero BB repulsion (the range of g is fixed to choose the optimal value of interaction to measure the p-wave superfluid gap Δ_{gap}).*

coupling values, in order to deal with a smaller condensate fraction. A reasonable compromise between a not too small p-wave superfluid gap and a not too large condensate fraction is reached when $0.5 < g < 0.7$: in this regime the p-wave superfluid gap varies between $\Delta_{gap} \approx 0.14\ E_F$ (at $g = 0.5$) and $\Delta_{gap} \approx 0.07\ E_F$ (at $g = 0.7$), with a condensate fraction that varies from about 23 % to about 17%. We thus propose this range of BF couplings as the optimal one for the experimental observation of a p-wave superfluid of BF molecules in 2D.

Conclusions and future perspectives

In this master degree thesis we have studied a two-dimensional Bose-Fermi mixture, with a BF-attraction, using a T-matrix approach. Most of our simulations were performed for BF mixtures with equal masses for different boson concentrations $x = n_B/n_F$ (with $x \leq 1$) and exploring different regimes of the BF attraction.

By implementing the formalism defined in Chapters 3 and 4 in a numerical code written in Fortran 90, we have been able to study the behaviour of several thermodynamic quantities, such as the momenta distribution functions $n_F(k)$ and $n_B(k)$, the chemical potentials, the condensate fraction, and the Tan's constant.

The main results of the present work can be summarized as follows.
(i) We have found a universal behavior for both the condensate fraction and the Tan's constant with respect to the boson concentration. Specifically, we have found that the condensate fraction depends only on the boson-fermion interaction and is nearly independent from the boson concentration. A similar universality is found for the Tan's constant when divided by the concentration x. The universality of the condensate fraction is in line with what previously found in 3D [5] and recently experimentally confirmed in [6]. Here, we have confirmed such (a priori unexpected) behavior in two dimension, and extended it to the Tan's constant. This universality is exciting, because it allows one to connect the above universal quantities for a Bose-Fermi mixture to related quantities (namely, the quasi-particle residue

and the dimensionless Tan's constant) for the highly studied polaronic limit ($x \to 0$) of a single impurity in a Fermi gas.
(*ii*) We have discovered a peculiar behavior of the bosonic momentum distribution, with a cusp feature which is present in an extended range of couplings and concentrations. We have attributed such a feature to the so-called indirect Pauli exclusion effect, an interesting effect previously found in 3D in the molecular limit of Bose-Fermi mixtures. It is particularly interesting that in 2D this effect occurs well before the molecular limit, and coexists with the presence of a significant boson condensate.
(*iii*) While the main behavior of the boson and fermion chemical potentials vs. the BF coupling is similar to what found in 3D, we have found some significant qualitative differences for certain features. The origin of these differences between the 3D and 2D cases deserves further investigation. In particular, an analytic study of the molecular limit of 2D Bose-Fermi mixtures could shed some light in this respect.
(*iv*) We have found that in 2D, contrary to the 3D case, the condensate fraction never vanishes completely. We have argued that this is probably due to a shortcoming of the T-matrix approximation in 2D. This does not represent a too severe problem, to the extent that the condensate fraction becomes in any case exponentially small, and thus indistinguishable from zero for all practical purposes, above a certain BF coupling strength.
(*v*) Finally, we have estimated the size of the gap for the p-wave superfluid of BF molecules that should form in a Bose-Fermi mixture according to a recent theoretical proposal [10]. With our numerical simulations, we were able to take into account the condensate fraction, which is in competition with the formation of molecules. In this way, we have identified the optimal coupling range for the experimental realization of this new example of a p-wave superfluid.

Several future extensions of the present work are foreseen. First of all, BF mixtures with a majority of bosons should be explored, by studying the momenta distribution functions, condensate fraction and chemical potentials in an analogue way to what we have done in the present work.

Moreover, one should also consider the case of different boson and fermion

masses, to obtain more stringent comparisons in the weak coupling regime, and to explore if the universality and other effects that we have found for isotopic mixtures will persist also for mixtures of different atomic species.

The problem of the mechanical stability of 2D Bose-Fermi mixtures should also be thoroughly analyzed. Within the present formalism, this would entail calculating the compressibility matrix, and determining the minimum value of the boson-boson repulsion required to guarantee the positivity of the compressibility matrix. This kind of analysis would be of particular relevance for future experiments with 2D Bose-Fermi mixtures, for which, as mentioned above, the scattering lengths a_{BF} and a_{BB} can be tuned almost independently by using a Feshbach resonance to control one scattering length, and a confinement-induced resonance to control the other length.

Finally, dynamical quantities such as the spectral weight functions $A(\mathbf{k}, \omega)$ for the two species should be calculated. On the one hand, this would allow one to better interpret the above peculiar behavior of the bosonic momentum distributions (possibly, by evidencing different quasi-particle intensities which contribute simultaneously to construct $n_B(\mathbf{k})$ from the corresponding $A(\mathbf{k}, \omega)$). On the other hand, this would also allow one to derive quantities, like the radio-frequency spectroscopy intensity, of direct access with experiments with ultracold gases.

The work done in this master degree thesis thus represents a first step in the theoretical analysis of 2D Bose-Fermi mixtures with a strong Bose-Fermi pairing attraction, which we hope will motivate several further theoretical and experimental works in the near future.

Bibliography

[1] I. Bloch, J. Dalibard, S. Nascimbène, *Quantum simulations with ultracold quantum gases*, Nat. Phys. **8**, 267 (2012).

[2] F. Schäfer, T. Fukuhara , S. Sugawa, Y. Takasu, Y. Takahashi, *Tools for quantum simulation with ultracold atoms in optical lattices*, Nat. Rev. Phys. **2**, 411 (2020).

[3] E. Fratini, P.Pieri, *Pairing and condensation in a resonant Bose-Fermi mixture*, Phys. Rev. A **81**, 051605 (2010).

[4] E. Fratini, P.Pieri, *Mass imbalance effect in resonant Bose-Fermi mixtures*, Phys. Rev. A **85**, 063618 (2012).

[5] A. Guidini, G. Bertaina, D. E. Galli, P. Pieri, *Condensed phase of Bose-Fermi mixtures with a pairing interaction*, Phys Rev A **91**, 023603 (2015).

[6] M. Duda, Xing-Yan Chen, A. Schindewolf, R. Bause, J. von Milczewski, I. Bloch, Xin-Yu Luo, *Transition from a polaronic condensate to a degenerate Fermi gas of heteronuclear molecules*, arXiv:2111.04301 (2021).

[7] M. G. Ries, A. N. Wenz, G. Zurn, L. Bayha, I. Boettcher, D. Kedar, P. A. Murthy, M. Neidig, T. Lompe, S. Jochim *Observation of Pair Condensation in the Quasi-2D BEC-BCS Crossover*, Phys. Rev. Lett. **114**, 230401 (2015).

[8] P. A. Murthy, I. Boettcher, L. Bayha, M. Holzmann, D. Kedar, M. Neidig, M. G. Ries, A. N. Wenz, G. Zurn, S. Jochim, *Observation of the Berezinskii-Kosterlitz-Thouless Phase Transition in an Ultracold Fermi Gas*, Phys. Rev. Lett. **115**, 010401 (2015).

[9] L. Sobirey, N. Luick, M. Bohlen, H. Biss, H. Moritz, T. Lompe *Observation of superfluidity in a strongly correlated two-dimensional Fermi gas*, Science **372**, 844 (2021).

[10] B.Bazak, D.S. Petrov, *Stable p-Wave Resonant Two-dimensional Fermi-Bose Dimers*, Phys. Rev. Lett. **121**, 263001 (2018).

[11] A. Guidini, *Superconductivity and Superfluidity in Multicomponent Systems*, Ph. D. thesis, Università di Camerino (2016).

[12] M. Schick, *Two-Dimensional System of Hard-Core Bosons*, Phys. Rev. A **3**, 1067 (1971).

[13] L. Caldarelli, *Ground-state properties of dilute Bose-Fermi mixtures in two and three dimensions*, tesi di laurea magistrale, Univerisità di Camerino (2014).

[14] H. T. C. Stoof, K. B. Gubbels, D. B.M. Dickerscheid, *Ultracold Quantum Fields*, Springer (2009).

[15] C. Chin, R. Grimm, P. Julienne, E. Tiesinga, *Feshbach Resonances in Ultracold Gases*, Rev. Mod. Phys. **82**, 1225 (2010).

[16] R. Carlone, M. Correggi, D. Finco, A. Teta, *A quantum model of Feshbach Resonances*, Ann. Henri Poincaré **20**, 2899 (2019).

[17] P. G. Averbuch, *Zero energy divergence of scattering cross sections in two dimensions*, J. Phys. A **19**, 2325 (1986).

[18] S. K. Adhikari, *Quantum scattering in two dimensions*, Am. J. Phys. **54**, 362 (1986).

[19] K. Chadan, N. N. Khuri, A. Martin, T. T. Wu, *Universality of low-energy scattering in (2+1) dimensions*, Phys. Rev. D **58**, 025014 (1998).

[20] D.S. Petrov, G. V. Shlyapnikov, *Interatomic collisions in a tightly confined Bose gas*, Phys. Rev. A **64**, 012706 (2001).

[21] Z. Hadzibabic, J. Dalibard, *Two-dimensional Bose fluids: An atomic physics perspective*, La Rivista del Nuovo Cimento **34**, 389 (2011).

[22] I. Bloch, J. Dalibard, W. Zwerger, *Many-Body Physics with Ultracold Gases*, Rev. Mod. Phys. **80**, 885 (2008).

[23] A. V. Turlapov, M. Yu Kagan, *Fermi-to-Bose crossover in a trapped quasi-2D gas of fermionic atoms*, J. Phys.: Condens. Matter **29**, 383004 (2017).

[24] P.Pieri, G. C. Strinati, *Strong-coupling limit in the evolution from BCS superconductivity to Bose-Einstein condensation*, Phys. Rev. B **61**, 15370 (2000).

[25] A. Guidini, G. Bertaina, E. Fratini, P. Pieri *Bose-Fermi mixtures in the molecular limit*, Phys. Rev. A **89**, 023634 (2014).

[26] G. Bertaina, A. Guidini, P. Pieri *Quantum Monte Carlo study of the indirect Pauli exclusion effect in Bose-Fermi mixtures*, Eur. Phys. J. Spec. Top. **224**, 497 (2015).

[27] H. Shi, A. Griffin, *Finite-temperature excitations in a dilute Bose-gas*, Phys. Rep. **304**, 1 (1998).

[28] G. Bertaina, E. Fratini, S. Giorgini, P. Pieri *Quantum Monte Carlo Study of a Resonant Bose-Fermi Mixture*, Phys. Rev. Lett. **110** , 115303 (2013).

[29] N. Read, D. Green *Paired states of fermions in two dimensions with breaking of parity and time-reversal symmetries and the fractional quantum Hall effect*, Phys. Rev. B **61**, 10267 (2000).

[30] K. Helfrich, H.W. Hammer, D. S. Petrov, *Three-body problem in heteronuclear mixtures with resonant interspecies interaction*, Phys. Rev. A **81**, 042715 (2010).

[31] A. Fetter, J. D. Walecka *Quantum Theory of Many-Particle Systems*, Dover Publications, (2003).

[32] S. Tan, *Large momentum part of a strongly correlated Fermi gas*, Ann. Phys. **323**, 2971 (2008).

[33] V. N. Popov, *Functional Integrals and Collective Excitations*, Cambridge University Press (1988).

[34] N.M. Hugenholtz, D. Pines *Ground-State Energy and Excitation Spectrum of a System of Interacting Bosons*, Phys. Rev. **116**, 489 (1959).

[35] W.H. Press, S. A. Teukolski, W. T. Vetterling, B. P. Flannery, *Numerical recipes in Fortran 90: The art of Scientific Computing*, Cambridge University Press, Cambridge, (1996).

[36] W.H. Press, S. A. Teukolski, W. T. Vetterling, B. P. Flannery, *Numerical recipes in Fortran 77: The art of Scientific Computing* Cambridge University Press, Cambridge, (1986).

[37] H. F. Khalfan, R. H. Byrd, R. B. Schnabel, *A Theoretical and Experimental Study of the Symmetric Rank-One Update*, SIAM J. Optim., **3**, 1-24 (1993).

[38] S. Zöllner, G. M. Bruun, C. J. Pethick, *Polarons and molecules in a two-dimensional Fermi gas*, Phys. Rev. A **83**, 021603 (2011).

[39] M. M. Parish, *Polaron-molecule transitions in a two-dimensional Fermi gas*, Phys. Rev. A **83**, 051603 (2011).

[40] Jonas von Milczewski, F. Rose, R. Schmidt, *Functional renormalization group approach to strongly-coupled Bose-Fermi mixtures in two dimensions*, arXiv:2104.14017v2 (2022).